NTNU
Det skapende universitet

Elektrisk resistivitet i industrielle SiC-lag

Magnus Austheim Krokstad

Materialteknologi
Innlevert: juli 2014
Hovedveileder: Merete Tangstad, IMTE

Norges teknisk-naturvitenskapelige universitet
Institutt for materialteknologi

I hereby declare that this work has been carried out independently and in compliance with the examination regulations of the Norwegian University of Science and Technology, NTNU.

_____

Magnus A. Krokstad

Trondheim, July 2014

PREFACE

This master thesis has been written as a part of the evaluation in the course TMT 4905.It is the culmination of five fantastic years at NTNU with a slight detour down under for a year.

First, I would like to thank my supervisor Merete Tangstad for her guidance and help through the last year. I really appreciate you taking time off in your vacation to help me finalise the thesis.

Second a huge thank you to all the technical staff that has helped me with my experimental work and planning. Especially Delphine Leroy, Bendik Sægrov, Morten Peder Raanes, and Ove Darell.

To everyone else who should be thanked, you know who you are!

ABSTRACT

It is thought that only 1% of the current through a silicon alloy furnace goes between the electrodes through the charge, and that the rest of the current strikes an arc between the electrode and the metal pool. An unknown current could go through the SiC-crust formed as the cavity-walls around the electrode. This could either be from arcs striking it or electrode-to-electrode currents previously thought to go through the silicon in the charge.

This work has investigated the electrical properties of SiC-crust samples from both an MG-Si producing furnace (Elkem) and a FeSi-producing furnace (Finnfjord) with the four point method at temperatures up to 1600°C. Atomic number contrast images of all samples were also obtained to investigate the composition of the industrial SiC-crust.

A resistivity in the range 0.1 – 1-0 Ω cm was obtained around 1600°C and the resistivity in an industrial furnace is thought to be even lower as the temperatures are higher in the furnace. Metal content (FeSi + Si) was found to affect the high-temperature resistivity with a decreased resistivity following the increase of metal. Increased porosity affected the low-temperature resistivity by increasing the resistivity, an effect that seems to drop off and disappear with increased temperature.

The composition of the samples varied widely, showing an inhomogeneity both between the samples and within the samples. Both the Elkem- and Finnfjord-samples were within each other's standard deviation when it comes to composition and the main difference between samples from the same furnace seemed to be the structure. While some samples had a very continuous SiC with little evidence of grains, other had a very clear grain-structure. While the position of the Finnfjord-samples is known, the Elkem samples comes from unknown positions in the crust and an informed discussion on structure relative to position is impossible. The structure does however seem to signify that the SiC does not come from reacted C-particles.

SiC is a very good conductor at high temperature, and it is likely that both a lot of the arcs strike against the crust and that a significant electrode-to-electrode current could go through the column on SiC found in the centre of the furnaces.

No final conclusion could be made regarding the formation-mechanism of SiC form this work, but several possibilities are described.

SAMMENDRAG

Det antas at 1% av strømmen som går gjennom en ovn som produserer silisiumslegeringer vil gå gjennom chargen mellom elektrodene, resten vil gå gjennom lysbuen som går fra elektroden til metallbadet. Det er ukjent hvor mye strøm som kan gå gjennom SiC-laget som dannes som kratervegg, enten som følge av at lysbuen treffer veggen eller at strøm går fra elektrode til elektrode gjennom den istede for chargen.

Dette arbeidet har undersøkt de elektriske egenskapene til prøver fra SiC-laget fra to ovner, en som produserer MG-Si (Elkem) og en som produserer FeSi (Finnfjord). Prøvene er undersøkt med firepunkts-metoden opp til 1600°C. Atomnummerkontrast-bilder ble også tatt av alle prøvene for å undersøke sammensetningen på SiC-laget.

Resistiviteten til prøvene ble funnet i området 0.1 – 1.0 Ωcm ved omtrent 1600°C, og vil sannsynlig vis være enda lavere ved temperaturene som finnes inni ovnen. Metallinnholdet (FeSi + Si) påvirker høytemperatur-resistiviteten, der en lavere resistivity ble funnet i prøvene med mer (FeSi + Si). Høyere porøsiteten økte lavtemperatur-resistivteten, men denne effekten ser ut til å forsvinne ved høyere temperatur.

Sammensetningen i prøvene varierte veldig, noe som er tegn på høy inhomogenitet selv innad i prøvene. Både Elkem- og Finnfjord-prøvene var innenfor hverandres standardavvik. Sammensetning, og hovedforskjellen på prøvene fra hver sin ovn viste seg å være strukturen. Noen prøver hadde veldig kontunierlig SiC med kun få spor av korn, andre hadde en tydelig kornstruktur. Selv om posisjonen til Finnfjord-prøvene er kjent er Elkem-prøvenes posisjon ukjent, dette gjør det vanskelig å diskutere strukturen i forhold til posisjon i ovnen. Det ser likevel ut til at SiC-laget ikke kommer fra karbonpartikler reagert med SiO (g).

SiC viser seg å være en svært god leder ved høy temperatur. Det er sannsynlig at flere av lysbuene vil gå fra elektrode til SiC-laget og at en merkbar strøm mellom elektrodene vil kunne gå gjennom SiC-søylen som er funnet i midten av ovnen.

Det kan ikke trekkes noen endelig konklusjon på hvilken formasjonsmekanisme som danner SiC, men flere mulige mekanismer blir diskutert.

LIST OF ABBREVATIONS

MG-Si	Metallurgical Grade Silicon, up to 98% Si
FeSi	An alloy of iron and silicon, not stoichiometric
EPMA	Electron Probe Micro Analyser
SEM	Scanning Electrode Microscope
XRD	X-ray diffraction
Z-contrast	Atomic number contrast
AC/DC	Alternating Current/Direct Current

CONTENTS

CHAPTER 1. INTRODUCTION

While the high silicon alloys are produced in an electric arc furnace as many other metal alloys, it differs with the existence of a gas cavity around the electrode tip. This cavity is formed from the furnace charge reacting to form gaseous SiO, which condenses and creates a supportive layer which has to be manually broken down by stoking (Schei et al., 1998, pp. 50-51).

On the inside of the glassy condensate layer a crust porous SiC is found, and while the current theory is that the SiC is formed from SiO (g) reacting with carbon particles from the charge this theory seem to be getting less support and other possible formation-mechanisms are discussed in this work. In samples from two recent excavations of a FeSi-producing (Tranell et al., 2010) and a MG-Si-producing (Tangstad et al., 2014) furnace differences in the carbide-crust is found both in composition and structure.

The metal-producing reaction SiO (g) + SiC = 2 Si (l) + CO (g) requires temperatures above 1811°C to run favourably to the right (Schei et al., 1998, pp. 29), and the heat in the furnace is supplied by an electric arc striking from the electrode to the metal bath or crust. While the current theory states that most of the arcs strike the metal, quite a lot of the arcs have to strike the SiC-crust as well. This comes from the findings that the current equipment cannot sustain arcs longer than 10 cm (Saevarsdottir et al., 2001). As the electrode is moving much larger distances in short amount of time, a fair amount of the arcs have to strike against the crust.

One of the major factors determining the quality of the operation is the electrical current paths, and hence the energy distribution in the furnace. It is found that if only one arc exists in the cavity at any given time, 2/3 of the transformer current will go between electrodes through the charge (Saevarsdottir and Bakken, 2010). As this electrode-to-electrode current is thought to be around 1% (Valderhaug, 1992) when going through silicon in the charge, the electrical properties of SiC is of major interest as current could be flowing between electrodes though the centre-column consisting mainly of SiC. The resistivity of the furnace materials will determine the electrical current paths. With the exception of the arc, the electrical resistivity of the materials in a furnace producing silicon alloys has not been previously investigated.

The resistivity of the SiC-material from both the Finnfjord- and the Elkem-excavation is examined in this work, along with their composition, with techniques developed in an earlier work (Krokstad, 2013). The aim of this work is hence to investigate the SiC-crust from excavation samples, and obtain data on the electrical properties of it along with compositional data. This will aid in the further modelling of furnaces as to improve the furnace operation and could also give a lead into the formation mechanism of the SiC-crust. -

CHAPTER 2. THEORY

This chapter will go through the theoretical background needed to discuss the results achieved in this work. First it will explain electrical conductivity, focusing on semiconductors, before it goes through the process of making MG-Si and FeSi, discussing the raw materials, furnace operation and the excavation of two furnaces producing MG-Si and FeSi respectively. After this, the electrical properties of materials and electrical pathways in the furnace are discussed.

2.1. Electrical Properties

2.1.1. Crystal Bonds and Band Gaps

In a single atom, electrons can only occupy specific energies with two electrons allowed in each energy level. This rapidly changes as atoms go together to form lattices, which creates overlap in the electron orbitals. This overlap leads to a bond formation, giving all electrons a range of energies to choose from as shown in Figure 2.1.

Also seen in Figure 2.1 is the band structure of a metal, where some energy bands overlap. In a semiconductor, the teal band is filled while the pink band is empty, but in the metal the overlap causes electrons to have both bands available. Only electrons of high enough energy can flow through a material and conduct electricity, this minimum energy is defined as the Fermi Energy, E_F. In semiconductors, this energy is located in between two gaps while in metals it is located inside a band. This means that little to no added energy is required for electrons to achieve energy high enough for conduction. This is shown with an imagined example in Figure 2.2

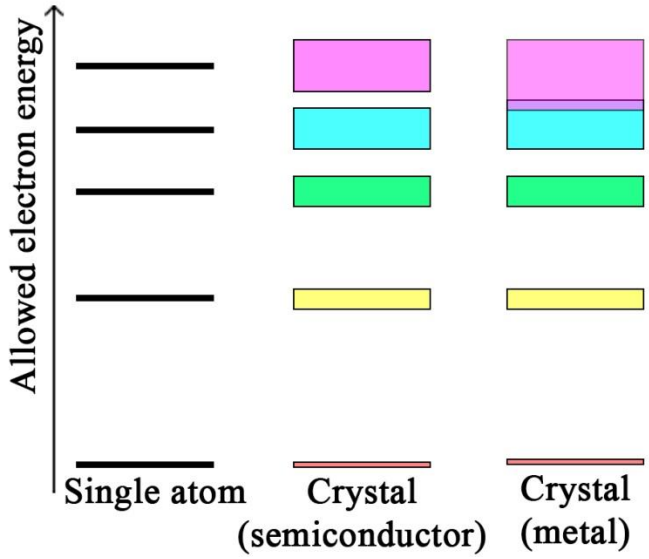

Figure 2.1: Allowed energies in a single atom compared to a crystal (simplified after Askeland and Phulé (2003))

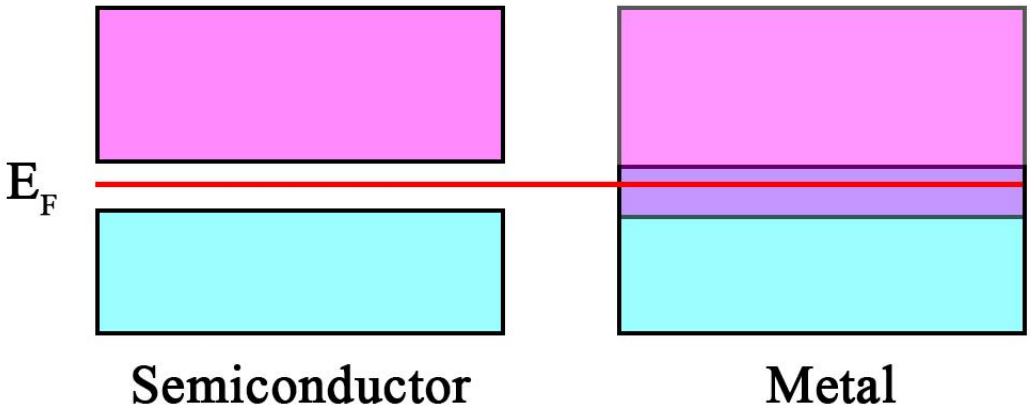

Figure 2.2: Simplified sketch of Fermi Energy compared in a semiconductor and a metal

In the semiconductor, the teal band is filled while the pink is empty. This gives rise to a high difference in energy between the ground state of the electron and the conducting state which must be added before conduction can occur. This difference in energy is known as the band

gap, E_g, of the material. In metals, this energy addition is insignificant as many electrons already have energies very close to E_F.

2.1.2. Semiconductor Properties

Doping

With the exception of liquid silicon, all materials treated in this thesis are semiconductors. But the theory described above is only valid for pure semiconducting materials. Impurities, called dopants when added by purpose, in the crystal lattice of a different group in the periodic table will have more or fewer electrons compared to the original material.

If the dopant has fewer electrons than the original material, ie. Al in a Si lattice, it will introduce an acceptor energy level, E_a. If Si is doped with P instead, the extra electron will require much less energy to jump unto the conduction band from the donor level E_d. This is shown in Figure 2.3.

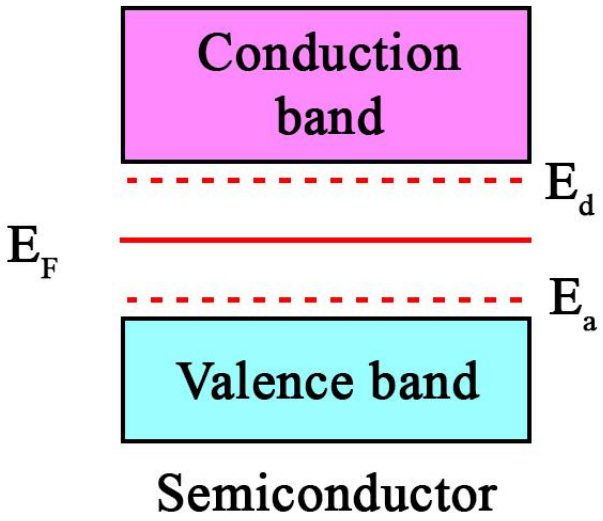

Figure 2.3: Doping in a semiconductor

The acceptor energy, E_a, allows for an electron to move out of the valence band and leave a positive hole behind to conduct electricity. The electrons with the donor energies, E_d, easily obtain enough energy to be in the conduction band and will be conducting electricity. This

effect is known as the extrinsic effect, and doped semiconductors are also known as extrinsic semiconductors.

Effect of temperature

As temperature is increased, more electrons obtain the energy required to stay in the conduction band, and thus a decrease in resistivity, ρ, is seen with temperature. This is called the intrinsic effect and the resistivity is defined as the Arrhenius equation found in Equation 2-1. k and c are material constants, E_g is band gap and T is the temperature.

Equation 2-1

$$\rho = k \cdot e^{\frac{E_g}{c \cdot T}}$$

However, if a semiconductor is doped the effects from dopants will be much greater than the intrinsic effect up to a certain temperature. This is the extrinsic effect and can be seen as the first range in Figure 2.4. Once the dopant atoms have been exhausted, only a small decrease in resistivity with temperature is seen. Finally, once the temperature is high enough, intrinsic effect take over and the resistivity decreases significantly again.

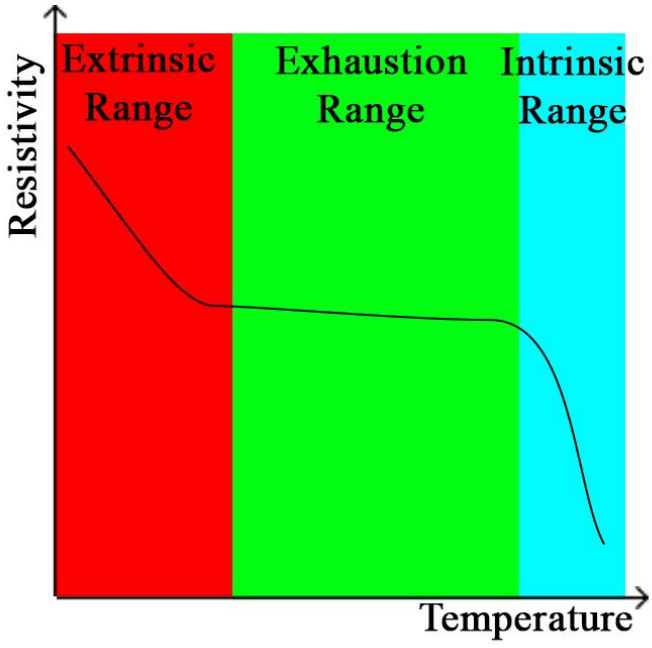

Figure 2.4: Resistivity of a doped semiconductor (simplified after Askeland and Phulé (2003))

For a doped, also called extrinsic, semiconductor, no overall formula can be used as each range show very different behaviour. It is however possible to apply Equation 2-1 for the high-temperature, intrinsic range.

2.2. High Silicon Alloy Production

The process of producing high silicon alloys such as MG-Si or FeSi of different qualities requires only a few different raw materials. The two main components are quartz (SiO_2) and carbon in the form of coal, charcoal or coke. To produce FeSi, an iron source is also needed. Woodchips are added to increase the permeability of the charge.

2.2.1. Quartz

Quartz is the second most abundant mineral in the earth's crust, ensuring it is readily available for use. However, as buyers requires purer products with more specific composition, producers of high silicon alloys have to use as pure SiO_2 as economically feasible.

The most important mechanical property of the quartz is the thermal strength. As the lumpy form is used to promote gas flow, any decrepitation could lead to fine particles blocking the free-flowing gas. This would lead to large gas channels forming, giving a low silicon yield which will be discussed further later. Pure SiO_2 melts at 1700°C (Eisenhüttenleute, 1995), but differs from other common oxides such as FeO and Al_2O_3 with the much higher viscosity in molten state as seen in Figure 2.5.

2.2.2. Carbon Materials

The advanced reaction pattern in a high silicon alloy producing furnace will be discussed later, but the overall reaction can be assumed to be reaction 2-1.

$$SiO_2 + 2C = Si + 2CO \qquad 2\text{-}1$$

Carbon is therefore essential to the production of silicon, and depending on the required purity; coke, coal or charcoal can be used alone or mixed together. Woodchips are also often added, but mainly as to increase the permeability of the charge (Gasik, 2013) and not as a source of carbon.

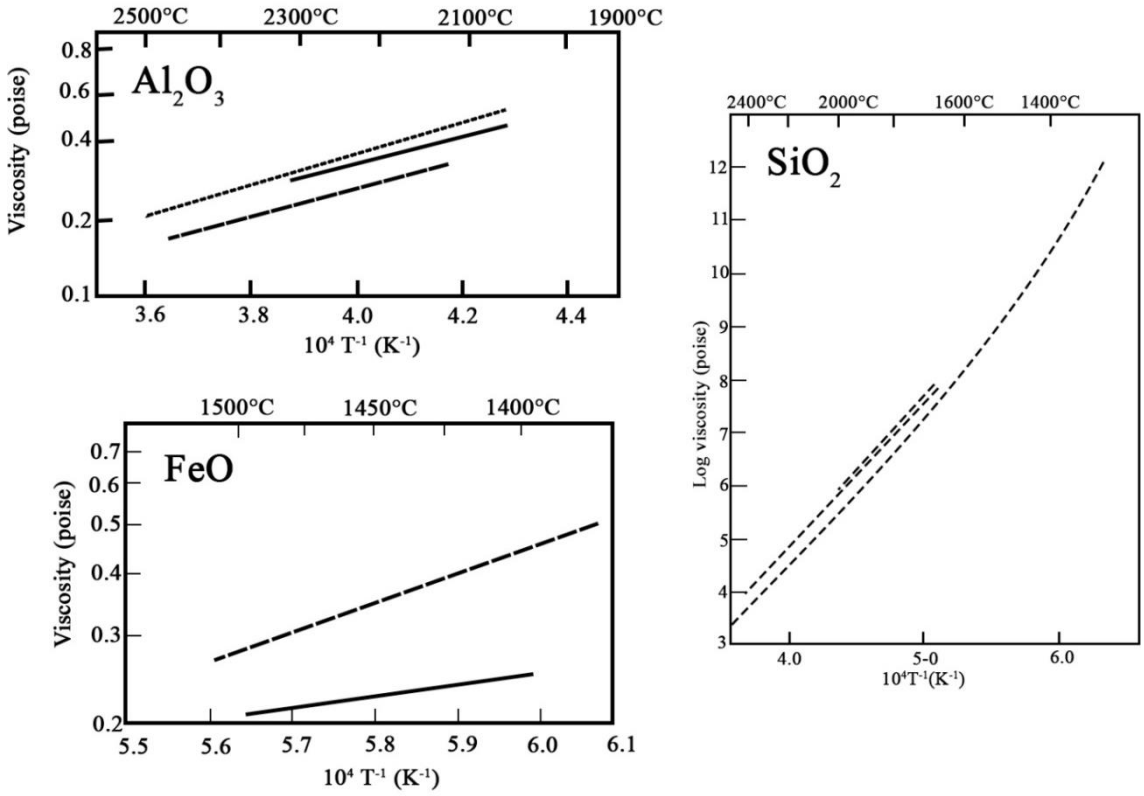

Figure 2.5: Viscosity of common oxide-species in metal production, adapted from (Eisenhüttenleute, 1995)

The amount of carbon available for reduction within the material is defined as the fixed carbon, and typical numbers can be found in Table 2.1 along with the amount of volatiles that burns off at relatively low temperatures high up in the furnace.

Even though it has a higher amount of fixed carbon, coke is seldom used to produce silicon alloys. This is due to the low reactivity between coke and SiO (g), which is important for good furnace operations (Schei et al., 1998, pp. 102). The reaction pattern will be discussed later, but a high reactivity with SiO leads to a smaller loss of Si from the furnace through the gas-phase and thus a higher yield.

Figure 2.6 shows the SiO-reactivity according to the SINTEF-test, where SiO (g) flows through a standard amount of graded carbon sample. After condensation of the remaining gas, it is measured how much SiO has passed through the carbon. A small amount of ml SiO coming through means a high reactivity. The SINTEF test was last reviewed by Lindstad et al. (2007).

Table 2.1: The fixed carbon and amount of volatiles in different carbon sources
1: (Eidem, 2008) 2: (Koukouzas et al., 2007) 3: (Ryu et al., 2006) 4: (Olanders and Steenari, 1995)

Material	Fixed Carbon (%)	Volatiles (%)
Coke[1]	85-90	1-1.5
Coal[1,2]	60-93	2-30
Charcoal[1]	77-81	18-21
Woodchips[2,3,4]	11-18	67-82

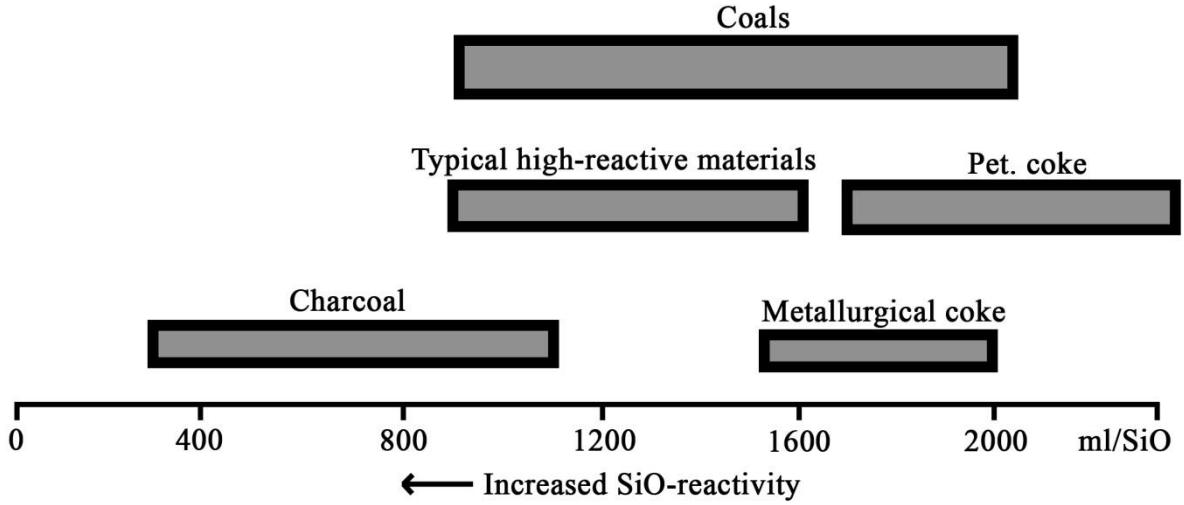

Figure 2.6: SiO-reactivity of different carbon-material. After (Schei et al., 1998).

2.2.3. Iron Source

To produce FeSi of any quality, iron is required along with the silicon oxide. This can come in the form of both iron scraps and iron ore, with the former requiring less additional carbon added to the process. The possibility for chemical control may be the deciding factor of which source is used at a plant.

2.2.4. Furnace Operation

Electrical energy

High temperatures are required for reduction of SiO_2, and the thermal energy in industrial furnaces is supplied by three electrodes striking plasma arcs inside the furnace. These arc have been studied and modelled by Valderhaug in his PhD thesis (Valderhaug, 1992), where he writes that the arcs forming in silicon alloy producing furnaces are high-pressure, high-power, free burning arcs. The temperature of these arcs is in the range of 20-30000K, and they are the main source of heat in the furnace.

Modelling of the electrical systems and the arc in furnaces have found that the current commercial electrical system is not able to sustain arcs longer than 5-10 cm (Saevarsdottir et al., 2001). This is interesting as the electrode holders, which indicate the electrode position for operators, vary much more than this length over short periods of time and will be discussed further later on.

Furnace reactions

As iron is known to reduce easily with CO, all iron found in the furnace at temperatures in the predominance diagram is assumed to be carbon-saturated, liquid Fe.

With the predominance diagram of the Si-C-O-system found in Figure 2.7 it is possible to discern the main reactions in a metallurgical Si-furnace. The following reactions are of utmost importance:

$$2\ SiO_2\ (s,l) + SiC\ (s) = 3\ SiO\ (g) + CO\ (g) \qquad 2\text{-}2$$

(Denoted [2.4] in Figure 2.7)

$$SiO_2\ (s,l) + Si\ (l) = 2\ SiO\ (g) \qquad 2\text{-}3$$

(Denoted [2.5] in Figure 2.7)

$$SiC\ (s) + SiO\ (g) = 2\ Si\ (l) + CO\ (g) \qquad 2\text{-}4$$

(Denoted [2.7] in Figure 2.7)

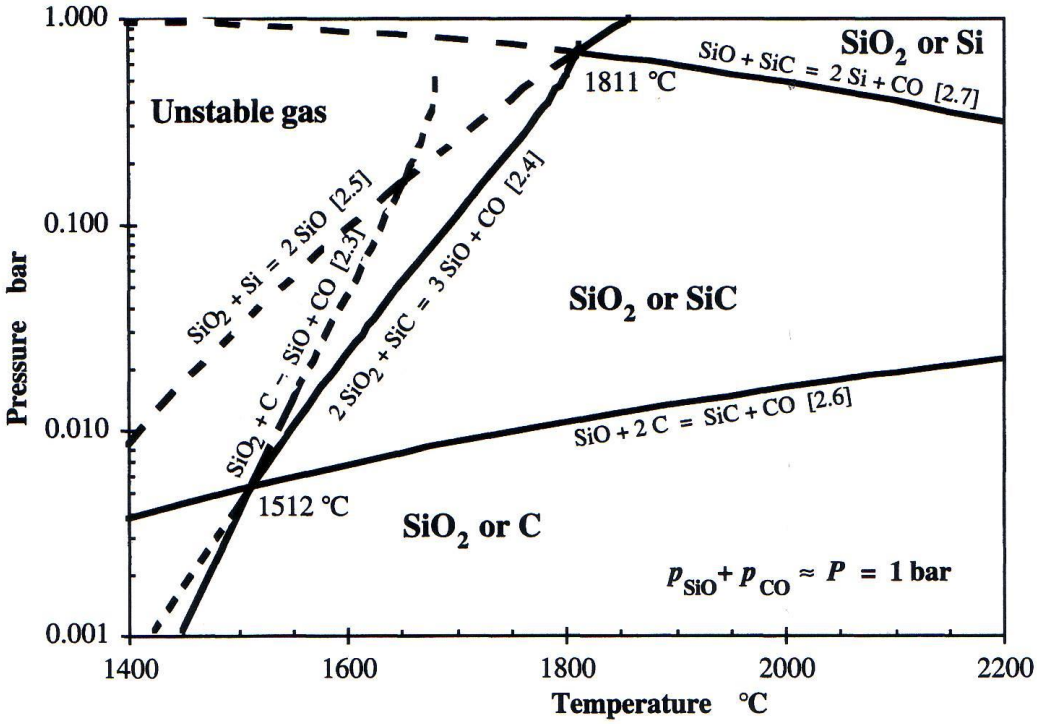

Figure 2.7: The predominance diagram of the Si-C-O-system (Schei et al., 1998, pp. 29)

All three reactions mentioned above require high temperature, above 1800°C, and will only happen in the inner parts of the furnace. In Figure 2.8 the inner parts can be seen as the metal bath (2-4 and 2-3) and along the cavity walls (2-2). For reactions 2-2 and 2-3 to occur, slag or quartz needs to enter the metal pool. One way this could happen is through the process of stoking the furnace, where the cavity crust supposedly collapses and could bring oxides along. Another way for oxides to enter the metal pool is along the electrodes, as the crust does not completely enclose them.

Both the excavations performed by Tangstad et al. (2014) and Tranell et al. (2010) found slag or raw materials (SiO_2) in samples from the metal pool, proving that it is possible for reaction 2-3 to happen. Figure 2.8 shows a sketch of a furnace producing high silicon alloys based on the findings of both Tangstad et al. (2014) and Tranell et al. (2010). Both excavations will be discussed later in this chapter.

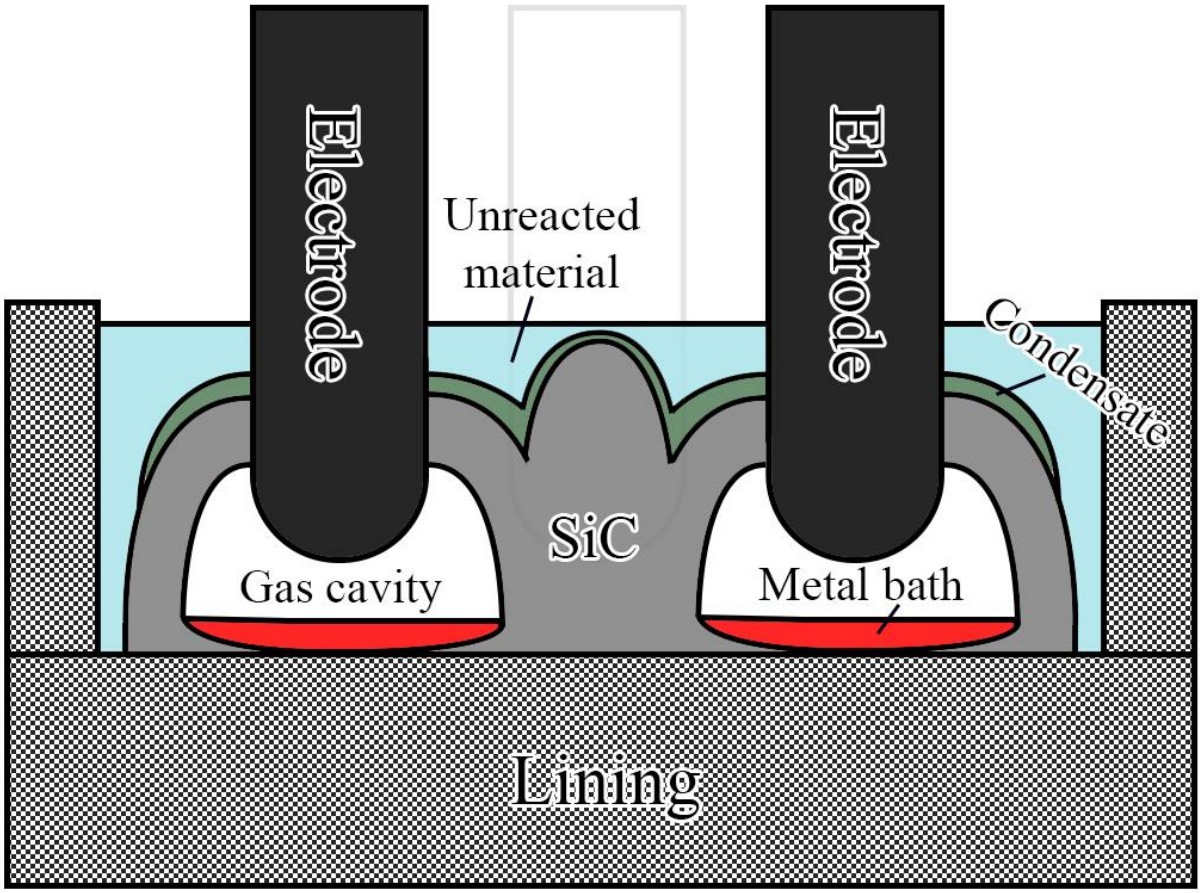

Figure 2.8: Not-to-scale sketch of a Si-furnace based on Figure 2.9 and Figure 2.10

Other reactions which could occur are the reduction of SiO_2 with solid carbon or SiC:

$$SiO_2\,(l) + 3C\,(s) = SiC\,(s) + 2\,CO\,(g) \qquad 2\text{-}5$$

$$SiO_2\,(l) + C\,(s) = SiO\,(g) + CO\,(g) \qquad 2\text{-}6$$

$$SiO_2\,(l) + 2\,SiC\,(s) = 3\,Si\,(l) + 2\,CO\,(g) \qquad 2\text{-}7$$

The first two reactions are however unlikely, as they require temperatures above the stability point of C which can be found only as SiC above 1512°C. This can be seen from Figure 2.7. Reaction 2-7 could run at the expense of reaction 2-2, but a calculation of ΔG in HSC Chemistry 7 by Outotec shows that reaction 2-2 is more favourable above 1800°C. Gas-condensed-reactions are also kinetically more favourable than solid-liquid-reactions.

As the SiO (g) and CO (g) formed in the inner parts of the furnace rises through the SiC-crust, temperature drops. Below 1811° SiO (g) is no longer stable and several reactions may occur:

$$2\ SiO\ (g)\ =\ SiO_2\ (s,l) + Si\ (l) \qquad 2\text{-}8$$

(Reverse [2.5] in Figure 2.7)

$$SiO\ (g) + 2\ C\ (s) =\ SiC\ (s) + CO\ (g) \qquad 2\text{-}9$$

(Denoted [2.6] in Figure 2.7)

$$3\ SiO\ (g) + CO\ (g)\ = 2\ SiO_2\ (s,l) + SiC\ (s) \qquad 2\text{-}10$$

(Reverse [2.3] in Figure 2.7)

Reaction 2-8 is the reverse of reaction 2-3 and forms liquid silicon if temperatures are above 1414°C. It is also strongly exothermic and will heat and partially melt the SiO_2. This glues the materials together forming a layer known as condensate. Stoking will break the layer, as it is brittle.

To achieve a high yield of silicon, the SiO-gas must be converted back to solid material before it leaves the furnace top where it will form amorphous silica. Reactions 2-8 through 2-10 will assure that, under perfect conditions, the partial pressure of SiO (g) out of the furnace is below 0.1% of the gas. As few metallurgical processes are run under equilibrium conditions the reactivity of SiO (g) with the different carbon sources and the size of the quartz particles are very important.

Both the SiO (g) and CO (g) leaving the furnace top will react with oxygen in the air inside the ventilation system through reactions 2-11 and 2-12. The solid is amorphous and is commonly filtered out and bagged for sale to the concrete industry.

$$2SiO\ (g) + O_2\ (g)\ = SiO_2\ (s) \qquad 2\text{-}11$$

$$2CO\ (g) + O_2\ (g) = CO_2\ (g) \qquad 2\text{-}12$$

Furnace layers based on excavations

The latest excavation was performed by Tangstad et al. (2014) on one of the MG-Si furnaces of Elkem Thamshavn, where samples were collected during the plant's excavation of the furnace. This led to a lower, but still sufficient, accuracy of where in the furnace the samples came from. Tranell et al. (2010) excavated a FeSi75-producing furnace at Finnfjord, where the more exact position of the samples was noted. Samples from both excavations are used in the experimental work of this thesis.

At the top of the furnace a layer of unreacted material which also extends towards the bottom of the furnace along the lining can be found. In the Finnfjord furnace the top charge layer was thicker, but less was found along the lining compared to the Elkem furnace.

Below the unreacted charge, the previously mentioned condensate is found. Condensate is divided into different types based on their colour, which it derives from the distribution of the constituent elements SiC, Si, Al and the respective oxides.

Tranell et al. found white and brown condensates in the FeSi-furnace while Tangstad et al. found brown and green condensates in the MG-Si-furnace. In experiments described by Schei et al. (Schei et al., 1998, Chapter 3.2.2.3) brown and green condensate was found in both FeSi and MG-Si production

Schei et al. and Tangstad et al. agree on both the brown condensate and the green condensate, identifying the brown as SiO_2 + Si and the green as SiO_2 and SiC. Brown condensate is most likely formed in reaction 2-8 while green condensate from reaction 2-10. Tranell et al. (2010) does not describe the white condensate in detail, but mention it glues together partially unreacted material and is most likely formed through reaction 2-8 as well.

The next layer in the furnace, and the focus of this thesis, is the SiC-crust. This crust was found to be much thicker in the Elkem furnace than in the Finnfjord furnace, but whether this is from the different products or the furnace operation is unknown. Gas channels were found in this layer by both Tranell et al. and Tangstad et al., proving a strong gas flow up from the cavity. Results from both excavations show that samples are quite porous on a macroscopic scale, but rather dense on microscopic scale.

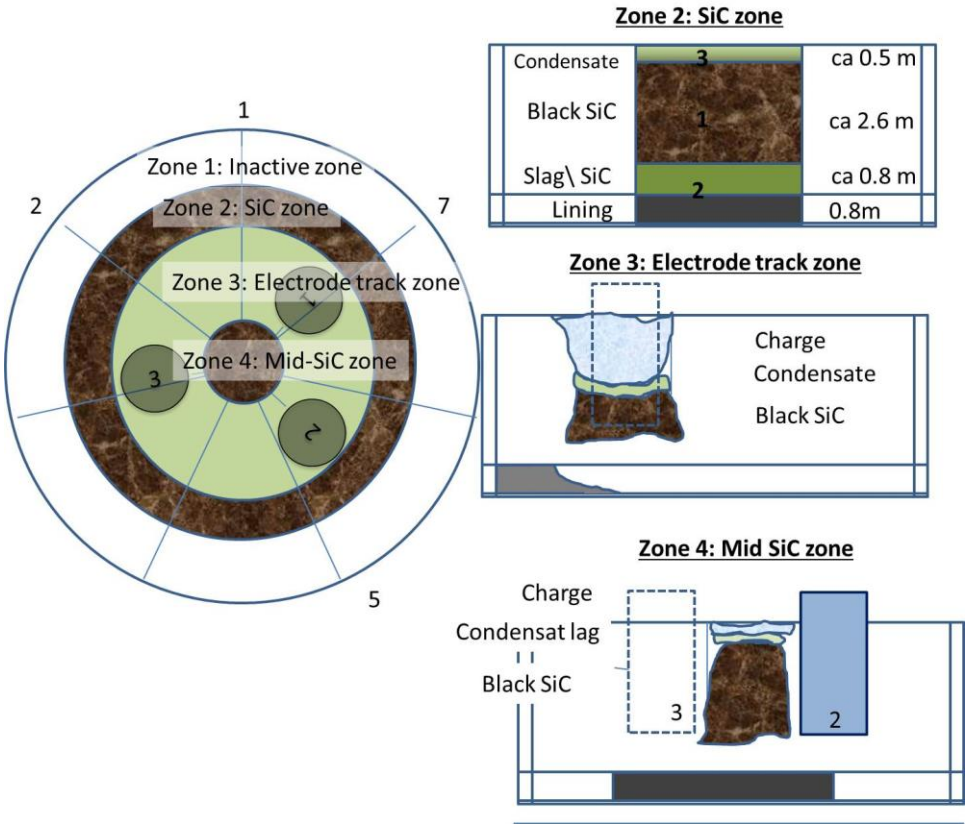

Figure 2.9: Furnace zones as described by Tangstad et al. (2014)

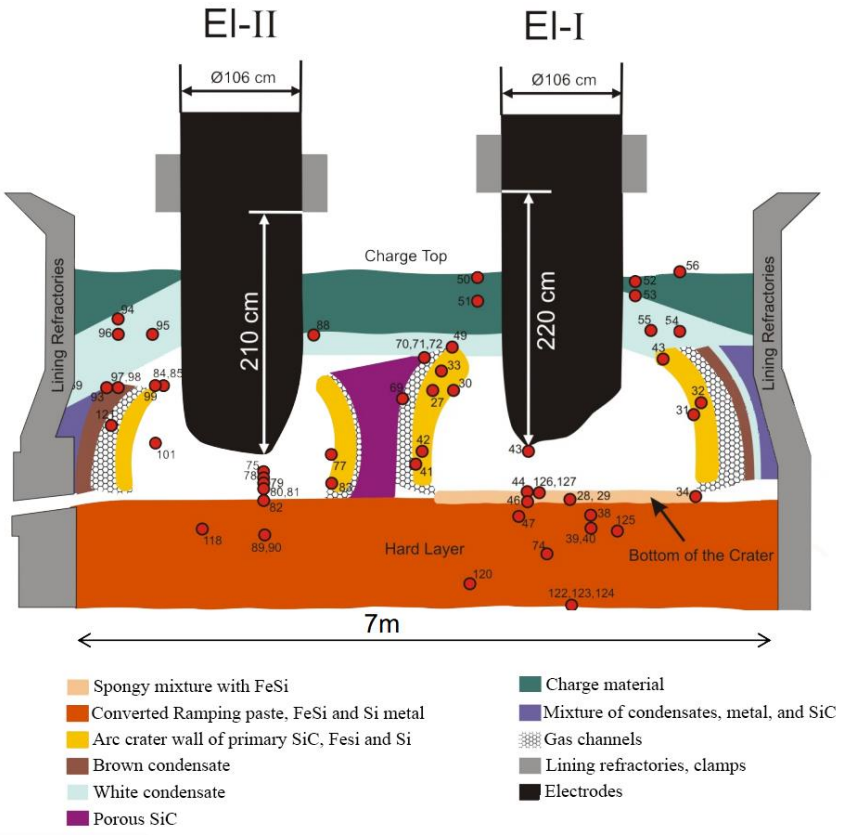

Figure 2.10: Furnace zones as described by Tranell et al. (2010). Figure found in Tangstad et al. (2014).

The SiC crusts may come from transformed C particles. However, with a dendritic surface structure found by Tangstad et al. (2014) it is also speculated that it could be formed from a gas phase. As the arc has temperatures up towards 30 000K, a number of gas species may be found. Tranell et al. shows EPMA-images of the crust, where areas of SiC seem to resemble the size of original carbon-particles indicating reaction 2-9 is the main reaction for SiC-formation.

Below the crust, a cavity is found around the electrode. The gases of this cavity are mainly SiO (g) and CO (g), but due to the high temperatures of the electric arcs several other minor species such as C, Al, Ca, Fe and their respective oxides and carbides can be found as well.

At the bottom of the cavity, a pool of molten metal along with SiC and some SiO_2 is found. This is where the main metal-producing reaction, reaction 2-4, is thought to happen. Below this a spongy SiC is found sitting on top of the refractory.

2.3. Electrical Properties of Furnace Materials

2.3.1. Silicon

Silicon is a well-known semiconductor material used frequently in solar cells and electronics. It is defined as a half-metal in the periodic table due to the metallic nature of its molten form which leads to a drop in resistivity once the melting point is reached.

There are no other surprising trends in the resistivity of pure silicon as found in Figure 2.11, the resistivity decreases with temperature although not as straight as theory dictates. This could be due to the small amount of dopant required to make an impact. The high resistivites at low temperatures is from the relatively high band gap of silicon which has been found as 1.12eV at room temperature (Bludau et al., 1974).

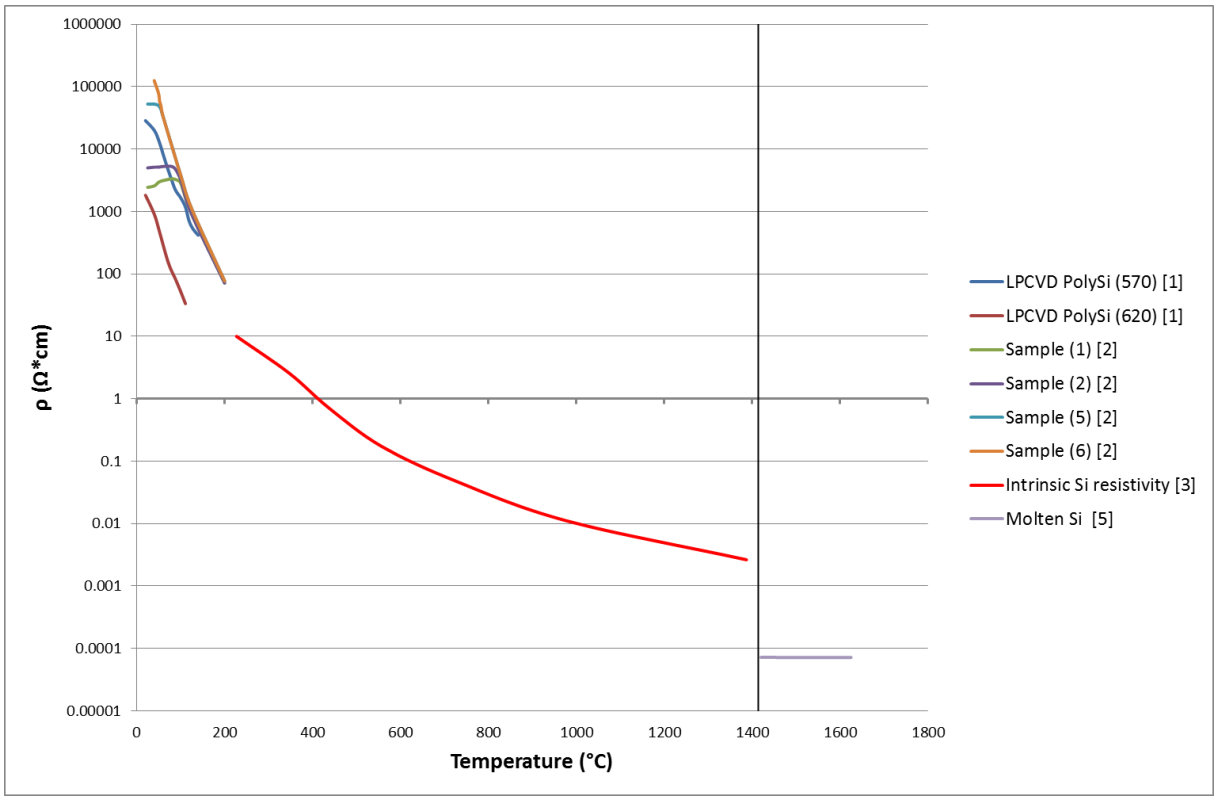

Figure 2.11: Resistivity as a function of temperature for undoped Si, the vertical line is the melting temperature of pure silicon
[1]: (Tomozeiu et al., 2000), [2]: (Hoffmann et al., 1959), [3]: (Law and Francois, 1956), [5]: (Sasaki et al., 1995)

2.3.2. Carbon materials

The carbon found in a silicon alloy furnace will have originated from coke, coal or woodchips. Other sources such as petroleum coke has also been tried to reduce the cost. Carbon will, however, mainly exist as SiC or CO-gas in the parts of the furnace which are of interest for this thesis and other C-species will not be discussed extensively. It should also be noted that coke is not much used in the production of high silicon alloys, but as Eidem (2008) preformed extensive research on coke it will be used as a basis for this discussion due to the lack of literature on the electrical properties of coal and other sources of carbon. Metallurgical coke is used widely in process producing other metals such as Mn and Cr with similar furnaces and will be used as a reference.

A few interesting fact should, however, be discussed. First is the band gap of diamond, which is 6.0eV (West, 1988) and much higher than silicon. This means that carbon in a diamond

structure will be an excellent insulator and have a very high resistivity. The different structures of carbon in graphite and coke do however have a much lower resistivity than silicon and act more like a metal in electrical terms.

Another interesting property of coke and graphite can be seen in Figure 2.12 where only an insignificant change in resistivity is observed with increased temperature. The negligible decrease is a huge contrast to silicon, and also defies the literature which states that SiC should be a better conductor than the carbon materials (Schei et al., 1998, pp. 142). This can be seen in Figure 2.15 and Figure 2.16, and the resistivity of SiC will be discussed in the next section. An explanation for the statement from Schei et al. can be found in the structural properties of the materials. While SiC is found in a continuous crust with little microporosity, carbon materials are fed into the furnace in bulk and the contact resistance between particles play an important role. The bulk-resistivity of coke can be found in Figure 2.13 which shows higher resistivity than SiC.

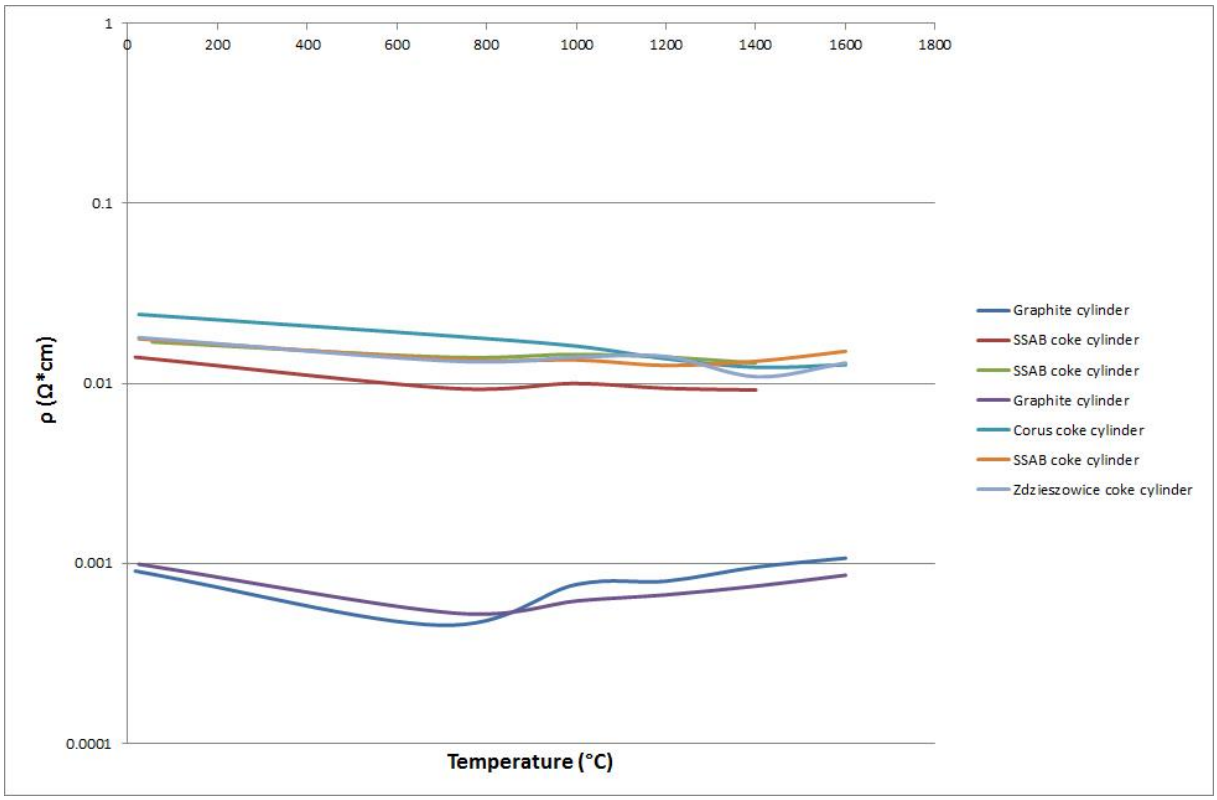

Figure 2.12: Material resistivity as a function of temperature for cokes.

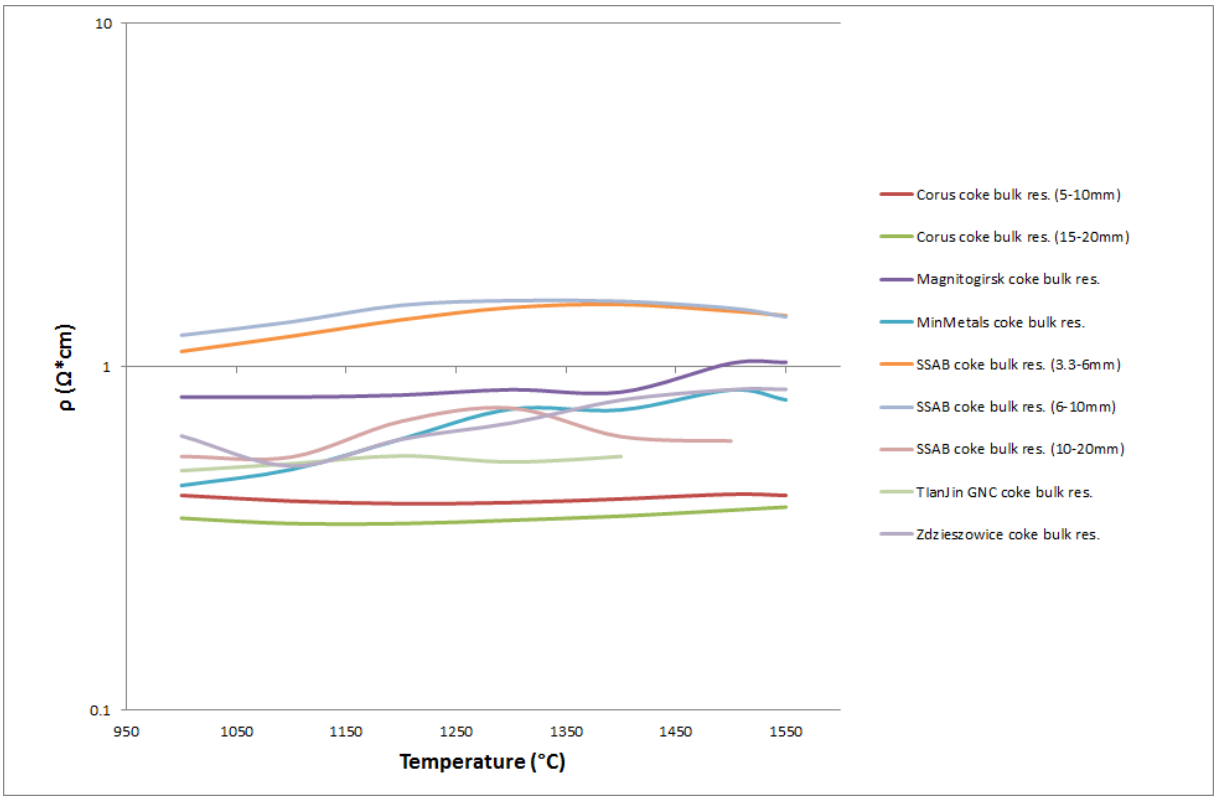

Figure 2.13: Resistivity of coke in bulk as a function of temperature. (Eidem, 2008)

2.3.3. Silicon carbide

The combination of two elements of group 14 in the periodic table, such as silicon and carbon, will still be an undoped semiconductor. The structure, however, is closer to that of silicon and diamond than coke, coal and graphite.

The band gap of SiC is found in the range 2.42eV – 3.33eV for the different polytypes (Shur et al., 2007), which is higher than silicon at 1.12ev. While the intrinsic resistivity of SiC, Figure 2.14, seems to be higher than for silicon at elevated temperatures, most of the literature reports of values much smaller resistivities at the whole temperature range as seen in Figure 2.15 and Figure 2.16.

The wide range of resistivities could be explained by the many different polytypes of SiC. One way to separate the main crystal structures is through the α- and β-notation where the former is hexagonal and the latter is cubic. But while there is only one way to structure SiC in a cubic lattice, several ways of packing the hexagonal structure is found (Kosolapova, 1968, pp. 193). Fetterley (1957) found that the literature at the time of his work indicated β as a better conductor than α. This is also supported by the findings of Pelissier et al. (1998). They found lower resistivities in β than in a β+α mixture, and the highest resistivity in α-SiC.

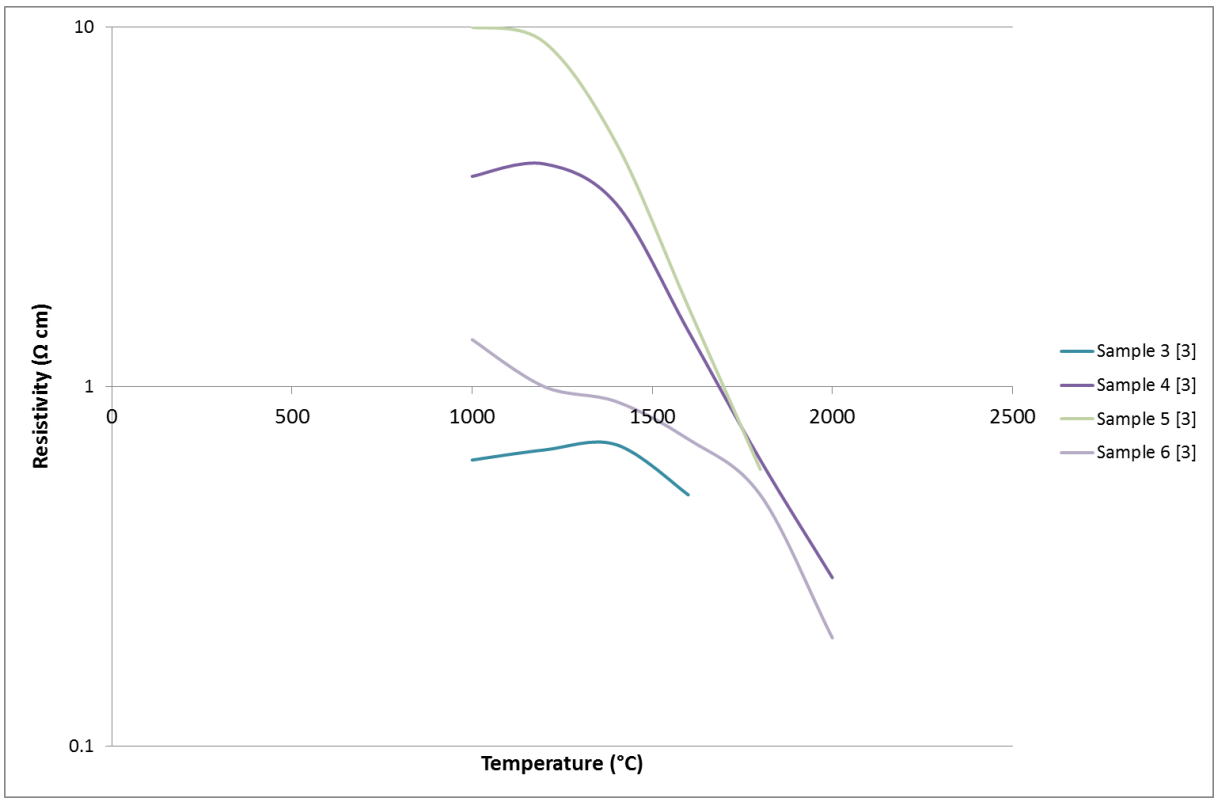

Figure 2.14: Intrinsic resistivity of SiC

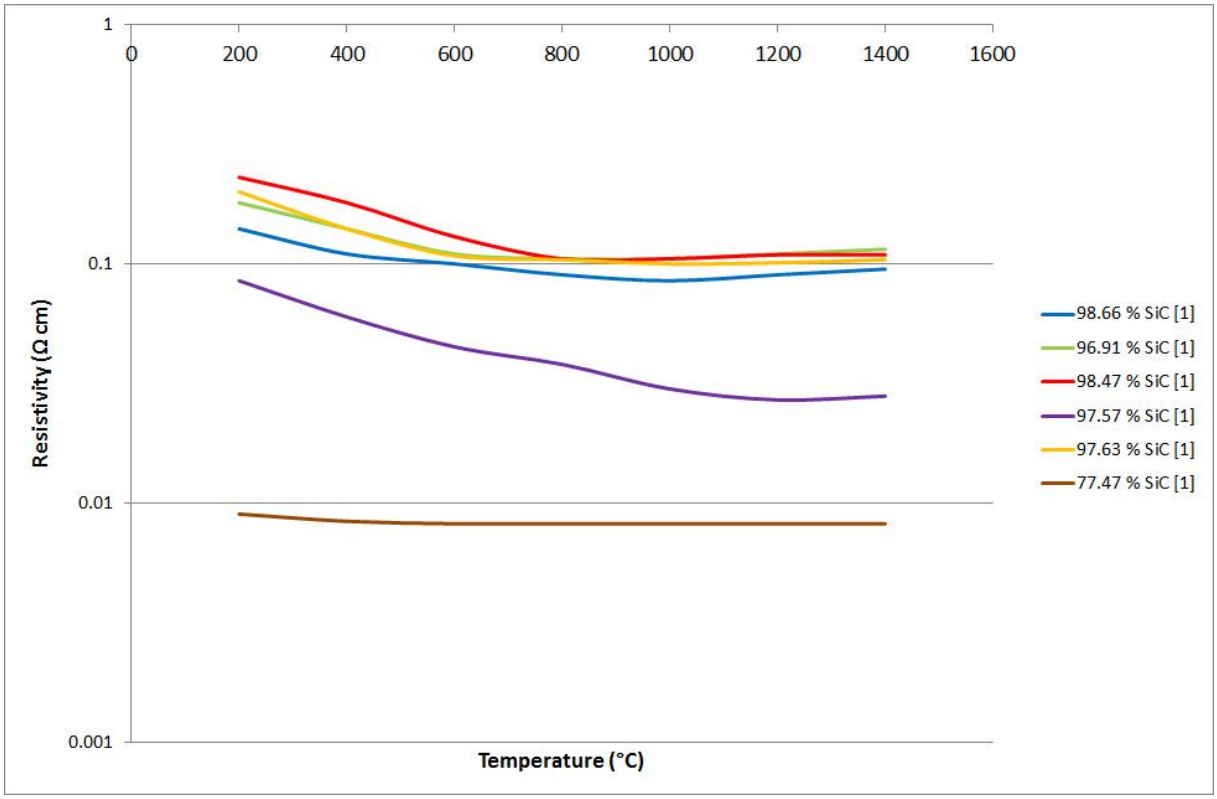

Figure 2.15: Resistivity as a function of temperature of impure SiC [1]: (Gnesin et al., 1978)

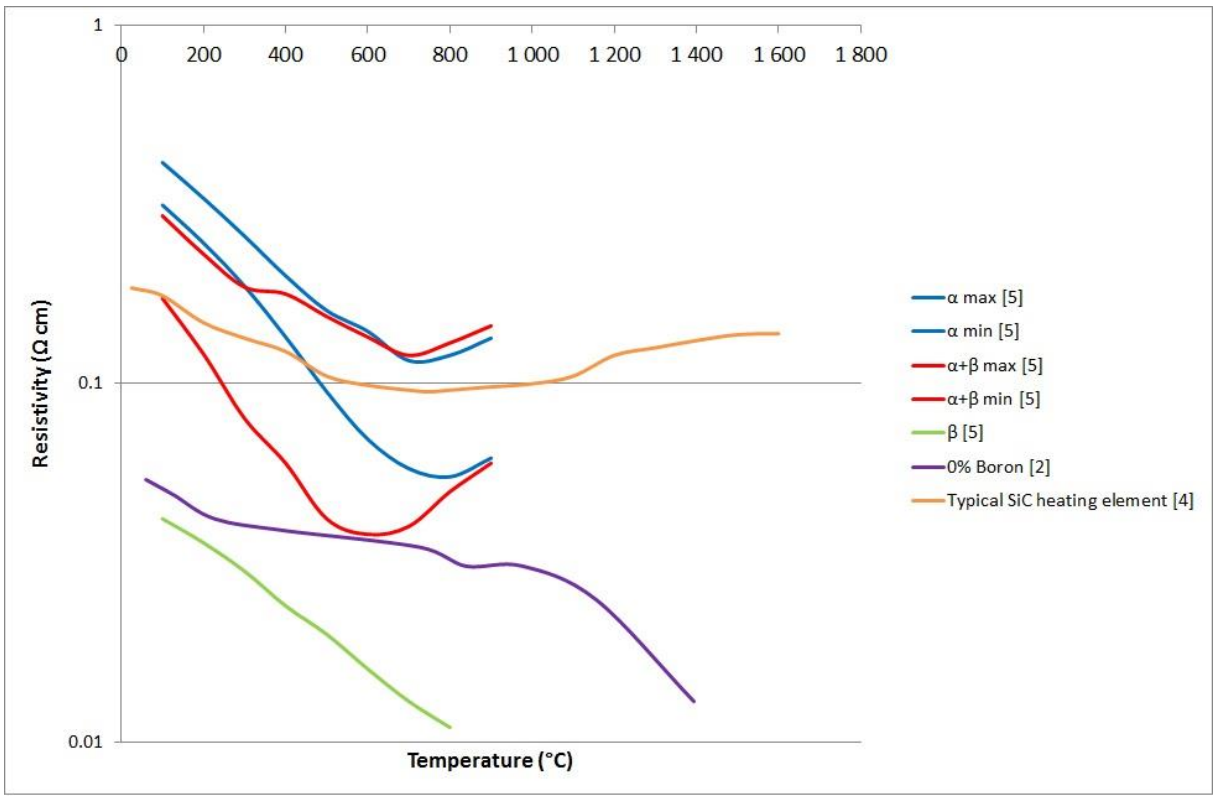

Figure 2.16: Resistivity as a function of temperature of impure SiC [2]: (Gnesin et al., 1983), [4]: (Fetterley, 1957), [5]:(Pelissier et al., 1998)

The initial decrease in resistivity during heating is reasonable with the extrinsic charge carriers being released as expected, the peculiar effect occurs in the “mid-temperature-range” where resistivity begins to increase with temperature as a metal. Several theories are found in the literature on this effect. Fetterley (1957) argues that the effect is the same as seen in metals, where the increased lattice vibration causes an increase in resistivity due to lower mobility of electrons. Gnesin et al. (1983, 1987) suggests that acceptor impurities appear in the degenerated SiC and stabilise the resistivity, while Pelissier (1998) believes that oxidation of the material forming silica is the reason for the increase the resistivity.

For temperatures above this increase, Fetterley (1957) suggests the intrinsic release of electrons from SiC will be favourable and cause another decrease in resistivity. Gnesin et al. (1978) argues that the resistivity will remain constant even above the temperatures found in their experimental work up to 1300°C. Racette (1957) did research on the intrinsic properties of hexagonal (α) SiC, Figure 2.14, and discovered that the intrinsic electron release started accumulating at around 1400°C - 1550°C. This effect is not observed in Figure 2.15 where most of the literature measurements stop at 1400°C.

2.3.4. Silicon oxide

The band gap of the different structures of silica is found above 8eV (Li and Ching, 1985), and as most production of high alloy silicon is done with relatively pure materials this thesis will assume SiO_2 is a perfect insulator allowing no electrical conduction.

2.3.5. Comparison

Although the values for the different materials operate on vastly different scales, Figure 2.17 compares all. It can be easily seen that silicon is the best conductor in liquid state but vary greatly below the melting temperature while impure SiC seems to be fairly unaffected by temperature.

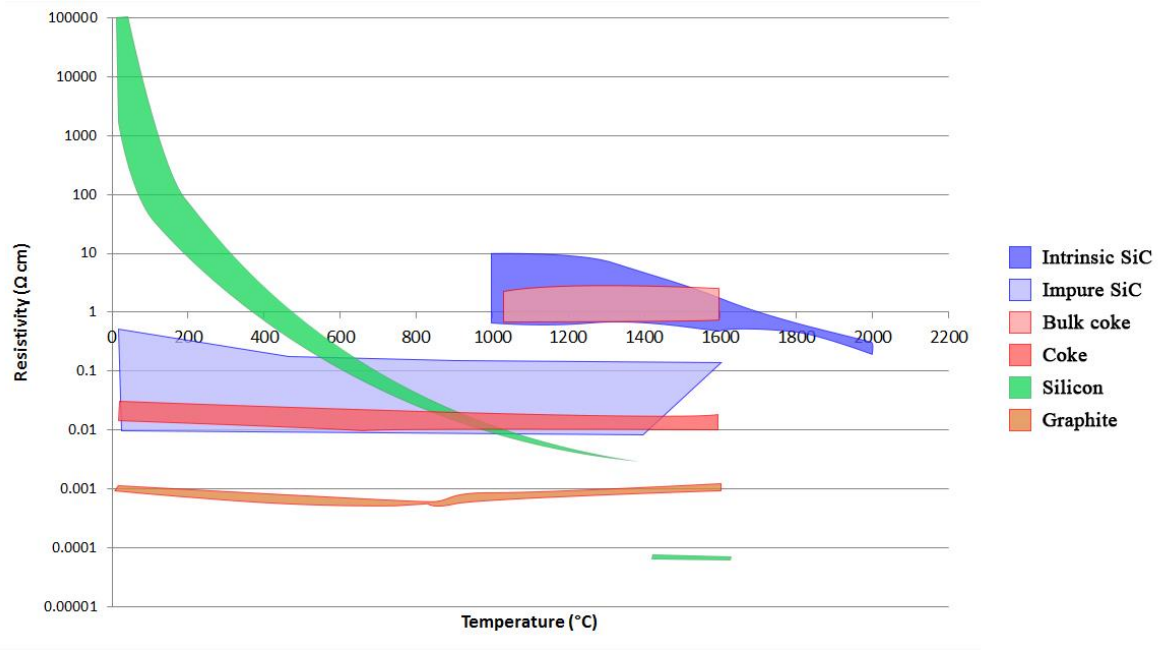

Figure 2.17: Resistivity of the different materials found in a high-silicon alloy furnace based on Figure 2.11 through Figure 2.16.

2.4. Electrical pathways in the furnace

It is widely accepted that most of the furnace current goes through the electric arc while only a small amount of current will flow through the different materials. Which materials this is, is still disputed. The most likely current paths, according to Schei et al. are found in Figure 2.18. This figure is updated to fit with the figure based on excavations discussed earlier in Figure 2.19.

The current paths in Figure 2.18 are as follows:

17.1 Arc from electrode tip to bottom layer silicon pool
17.2 Arc from electrode side to the upper parts of the conductive layer
17.3 Current from the electrode through the charge and into the bottom layer
17.4 Current from one electrode to another through the charge layer

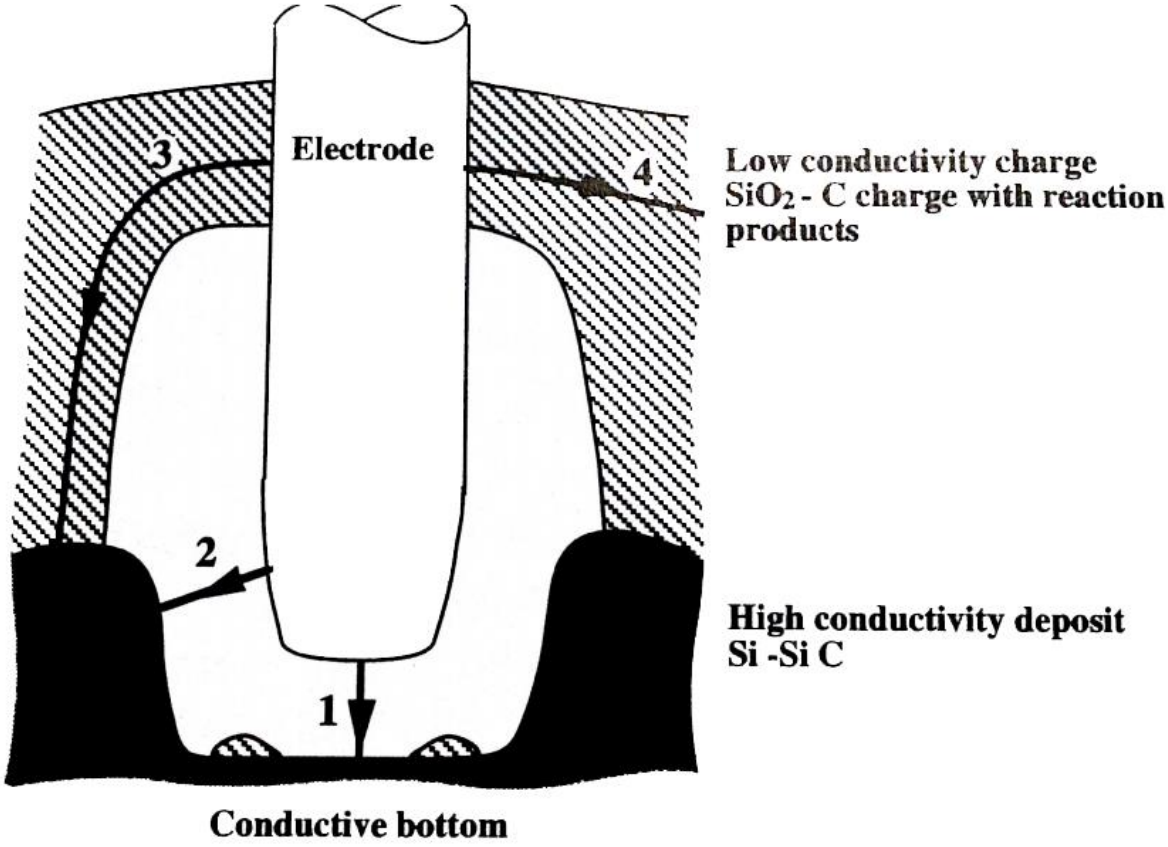

Figure 2.18: Possible current paths in the furnace as according to Schei et al. (Schei et al., 1998, pp. 156)

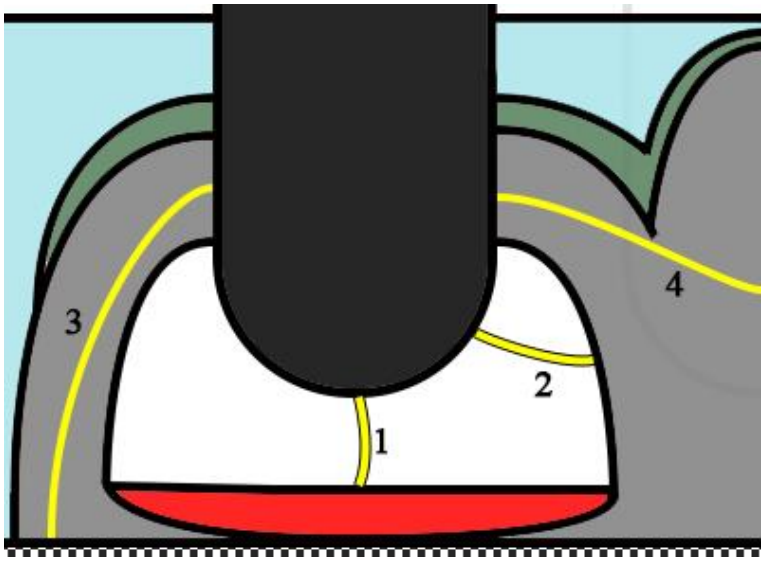

Figure 2.19: Current paths in a furnace, based on Schei et al. (1998).

For the updated figure, the more likely pathways seem to be:

18.1 Current from one electrode to another through the charge layer

18.2 Arc from electrode side to the upper parts of the SiC-crust

18.3 Current from the electrode through the SiC-crust and into the bottom layer

18.4 Current from one electrode to another through the SiC-crust

While the assumption that most of the current will go through the arc might be valid, the question whether it is between electrode and metal pool or SiC-crust is not answered. As mentioned in chapter 2.2.4, it is impossible to form arcs longer than 5-10cm with the commercially available transformers.

Data provided by Wacker Chemicals Norway, Figure 2.20, shows the relative position of the electrode throughout a normal 24hr period. This clearly shows that the electrode is moved more than 10cm up and down in short periods of time, indicating that if arcs are to be sustained at all times they have to strike against the SiC-crust. The data is based on the electrode holder and not the actual electrode tip, but it is unlikely that several cm of the electrode is removed over such short periods of time.

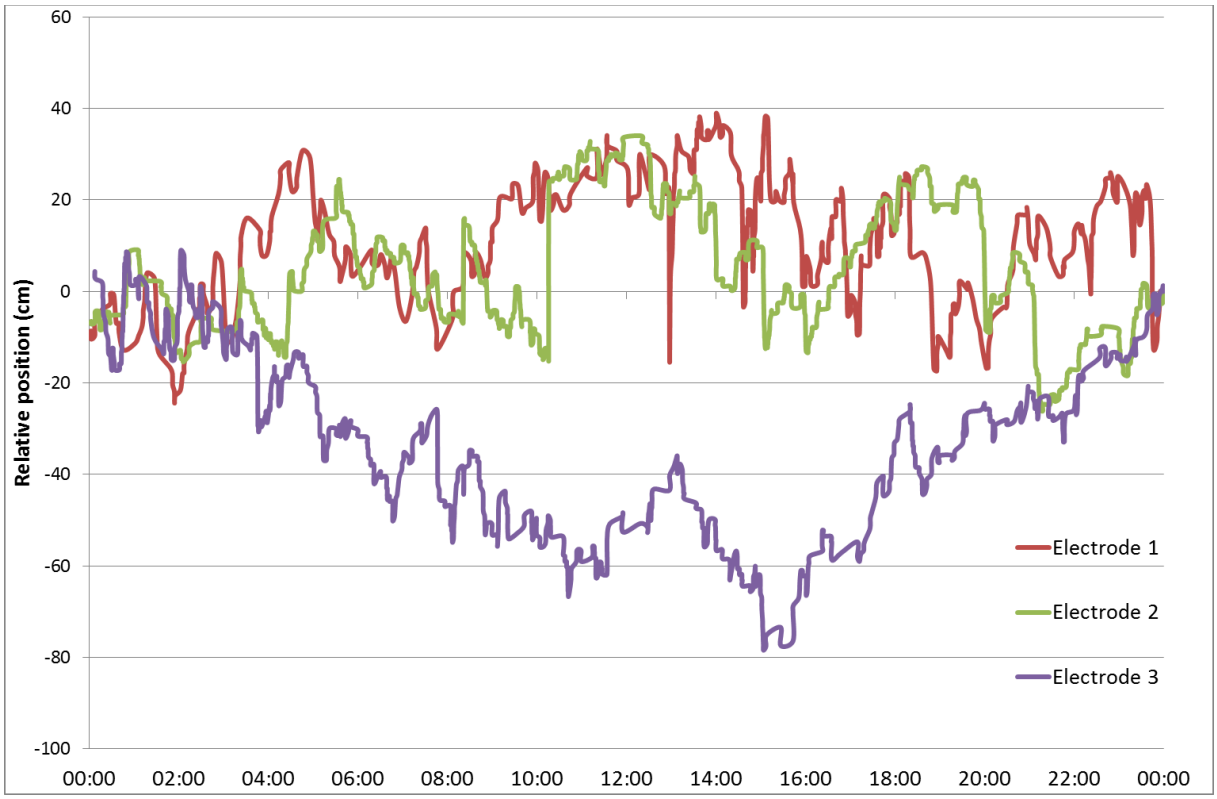

Figure 2.20: Relative electrode position (compared to 00:00) in a normal 24hr period

CHAPTER 3. EXPERIMENTAL WORK

3.1. Resistivity Measurements

3.1.1. Sample selection

SiC-crust samples originate from furnace excavations at Elkem Thamshavn by Tangstad et al. (2014) and Finnfjord by Tranell et al. (2010) . The position of the Finnfjord-samples can be seen in Figure 2.10. A summary of samples used in this work, and their origin is found in Table 3.1.

Table 3.1: Samples used for this work

Elkem excavation	Finnfjord excavation	Reference samples
E#1	F#33	Graphite rod
E#20	F#97	WM SiC
E#41		

In the earlier project work (Krokstad, 2013), two samples were prepared from sample 1 of the Elkem furnace excavation. One long and one short, but only the long sample is used in this work and will therefore be referred to as “Elkem sample #1”.

Samples of industrially produced SiC were supplied by Washington Mills at Orkanger, but were too brittle and fell apart during drilling.

3.1.2. Sample Preparation

Core samples were manufactured by two different diamond core drills. The first drill, used for the Elkem samples 1 and 41, had thin wall with a thickness of 0.1 mm with diamond sintered directly onto the wall and a diameter of 40 mm. The second drill was a more robust TWICS-drill, with a wall thickness of 1.5 mm and a separate crown with a thickness of 2.5 mm produced by Nortron Saint-Gobain. Outer diameter of the second drill was also 40 mm. To achieve a more reproducible sample preparation the ends of all samples were cut off with

Struers B0D25 Diamond Cut-Off saw using a Struers Discotom-5. Sample dimensions can be found in Table 3.2. All drilling was performed by Ove Darell at SINTEF.

Table 3.2: Sample dimensions

Sample	Diameter (cm)	Length (cm)
E#1	2.0	5.52
E#20	3.48	4.97
E#41	2.0	4.65
Graphite	2.55	6.48
F#97	3.41	1.842
F#33	3.542	3.08

While only two drills were used, the TWICS-drill was hard to mount perfectly vertical would be off axis causing the samples E#20, F#97 and F#33 to have somewhat different diameters.

On each end of the samples, molybdenum wires (1 mm diameter) were glued to the samples with Pelco® High Temperature Carbon Paste to act as electrodes. About one cm along the side of the sample, a groove was sawed into the sample to secure the position of the measurement-wires. The latter was glued in the grooves with the same carbon paste. The measurement wires were also Mo, but with a diameter of 0.127 mm. These were connected to wires of the same diameter as the electrode wires to reduce the risk of damage during heating.

Figure 3.1 shows the sample prepared for experiments, Figure 3.2 the full setup and Figure 3.3 the top of the lid. The top was the only visible part of the setup during experiments as seen in Figure 3.6.

Figure 3.1: Close-up of the sample before experiments

To further protect the wires from short circuiting and damage, alumina tubes were placed through the lid as seen in Figure 3.2. The outer wires were used as electrodes while the inner were used for measurements. A schematic of the setup inside the furnace is seen in Figure 3.5.

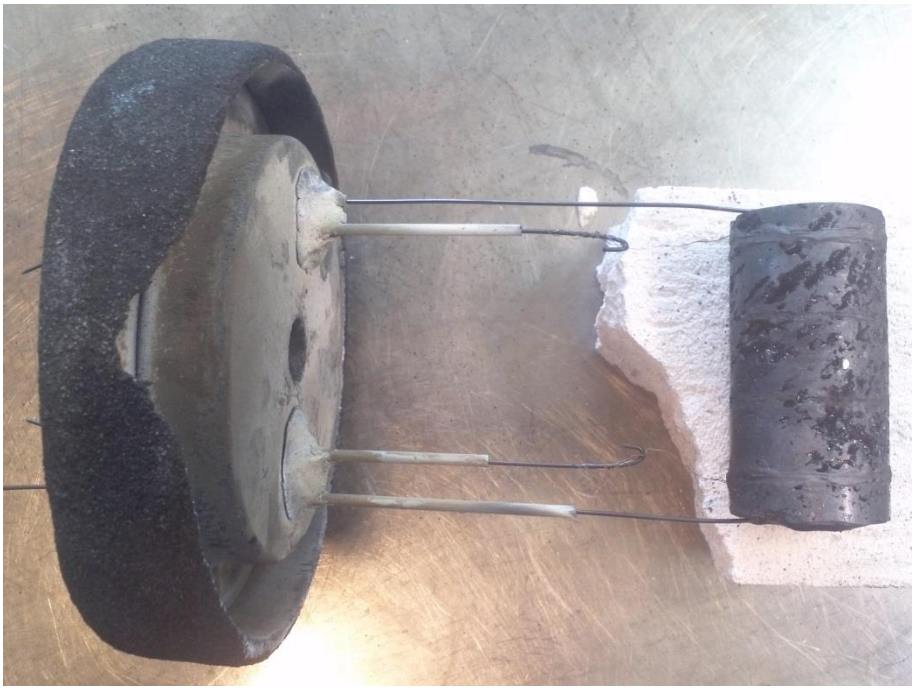

Figure 3.2: Full setup inside the crucible

3.1.3. The Four-Point Method

For measuring the resistivity, the four-point method was applied as seen in Figure 3.4. This method is simple and flexible, and was chosen over the simpler two-point method as it eliminates most of the contact resistance in the equipment and setup. It is also easier to control the distance between the measurement-points in this method, compared to the two-point method.

The four-point method utilises two wires connected around the sample, as seen in Figure 3.2, to measure the voltage drop over a known distance while also measuring the current of the outer circuit. The resistivity is then calculated via the resistance from the current and voltage drop with the known dimensions.

Figure 3.3: Top of the lid

Resistivity is found from resistance through Equation 3-1, where ρ is the resistivity, R the resistance, A the area and l the length between the two measurement points.

Equation 3-1

$$\rho = R * \frac{A}{l}$$

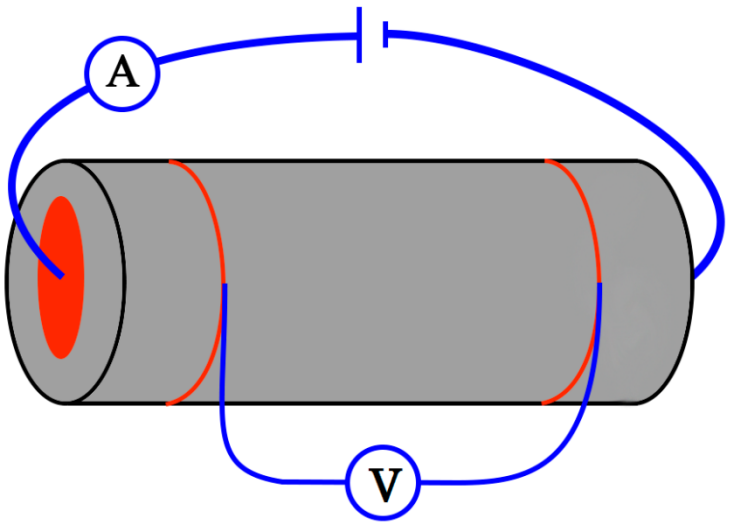

Figure 3.4: The four-point method as applied in this work

3.1.4. High Temperature Setup

This works utilises the same equipment and procedures as in the previous project work (Krokstad, 2013), with slight modifications. Instead of having relatively thin Mo-wires being connected to thicker wires, this work uses the thickest wires directly as electrodes. The same crucible is used, but a more stable alumina-brick was placed in the bottom to support the sample for the Elkem-samples. An alternative setup was used with the Finnfjord samples where the alumina-brick was replaced by metallurgical coke. The inside of the furnace is illustrated in Figure 3.5, while the top can be seen during the experiments in Figure 3.6.

Both voltage and current was measured using National Instruments NI9239 with software developed by Bendik Sægrov of SINTEF. The software also controlled the Kempower IPM15 welding transformer used for supplying the electrode current.

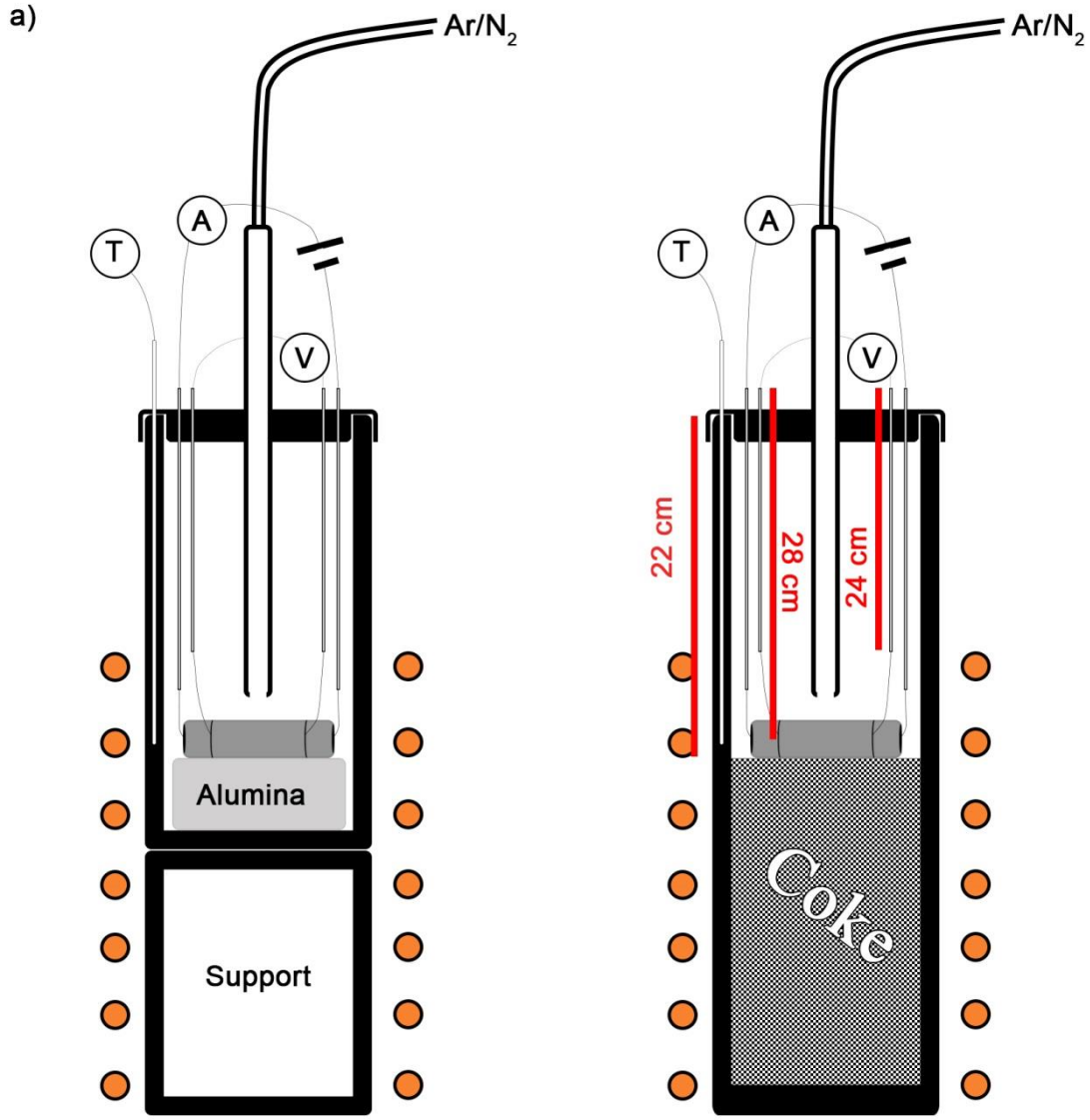

Figure 3.5: Sketch of the inside of the crucible during experiments. a) setup in the first seven experiments, b) setup in the following experiments. The scale is about the same for both.(A is current, V is voltage and T is temperature)

The furnace used was the Inductotherm 75kW furnace. The crucible was purged with excessive amounts of N_2 or Ar with a 4N purity to protect the molybdenum wires which are known to oxidise in air at temperatures above 600°C. The thicker wires were separated from each other and the lid by alumina tubes secured with alumina paste as to avoid short-circuiting the setup. This is shown in chapter 3.1.2. Standard copper-wires were used from the Mo-wires on top of the crucible to the measurement apparatus and the Kempower. These were protected by glass-fibre sleeves and pillows against the heat as can be seen in Figure 3.5. Even though the furnace was running while measurements were made, no significant change was observed and it was assumed the possible induced current in wires and sample was too small to be detected.

Figure 3.6: Top of furnace during experiments. To the far right is the thermocouple and in the centre a graphite lance is seen.

Due to nature of the setup it proved difficult to measure the exact temperature of the sample, but as SiC is generally known to be a good heat conductor and is used as heating elements it seems viable to expect it to have approximately the same temperature as the crucible. A type-

S thermocouple measured the temperature of the crucible, and the temperature was allowed to stabilise before resistivity-measurements was performed.

3.1.5. Test procedures

1. Preparing sample as seen in the previous chapter
2. Purge crucible with gas
3. Starting the furnace
4. Measure resistivity twice at every temperature, first at peak temperature and secondly 2-3 minutes later
5. Temperature-increments of 100°C per resistivity-measurement (exception after 1400°C), example of temperature-development seen in Figure 3.7

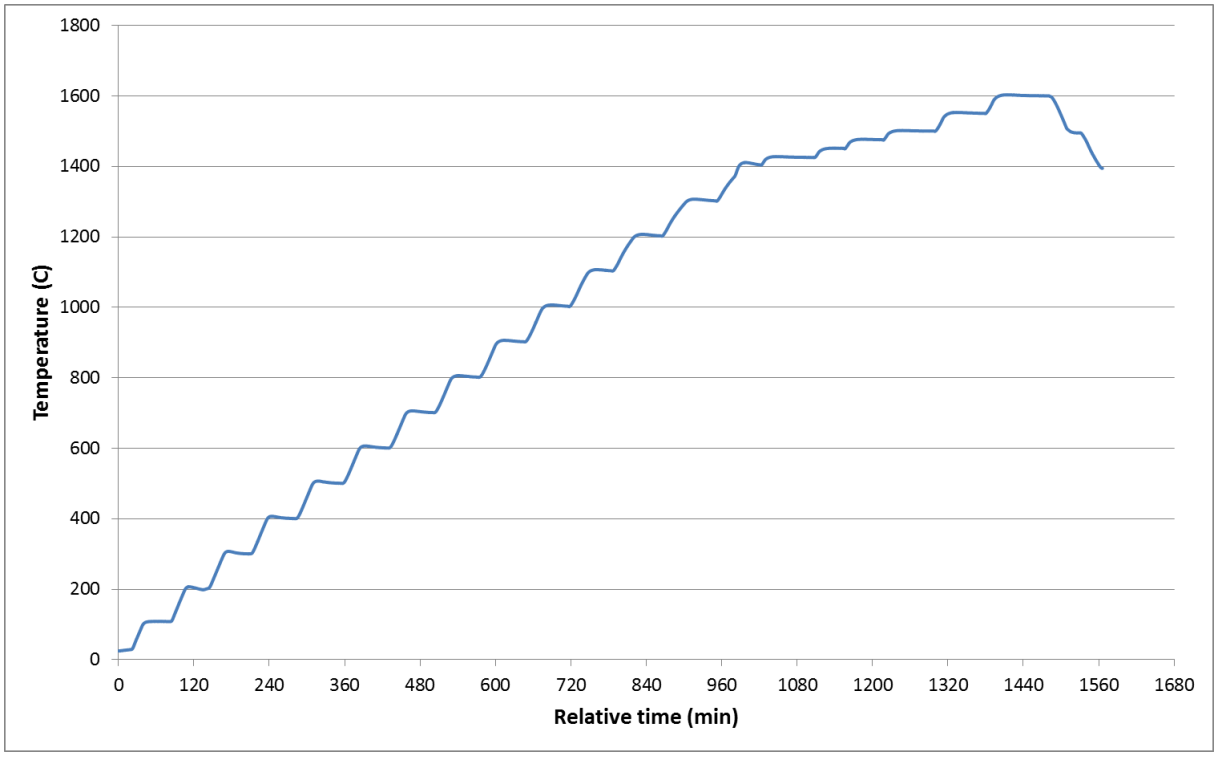

Figure 3.7: Temperature of the crucible in the experiment on sample F#97

As the dwelling time in the program was set to 10 minutes, the ramping was manually restarted once the second measurement was performed as to increase experiment efficiency. This leads to different dwell times at different temperatures.

All Elkem samples were tested at least once, while the Finnfjord-samples were tested only once. Some of samples where tested several times to test variation between experiments, and changes with heating cycles. Notation 1st, 2nd and 3rd signify which test the data is from. Samples were tested in the following order:

E#1 (1st through 3rd), E#41 (1st and 2nd), E#20 (1st and 2nd), F#97 (once) and F#33 (once).

Between each test, all wiring was redone while the crucible stayed the same.

3.1.6. Filtering of data

As the equipment measured both current and resistance continuously, a some noise was produced in the raw data as seen in Figure 3.8.

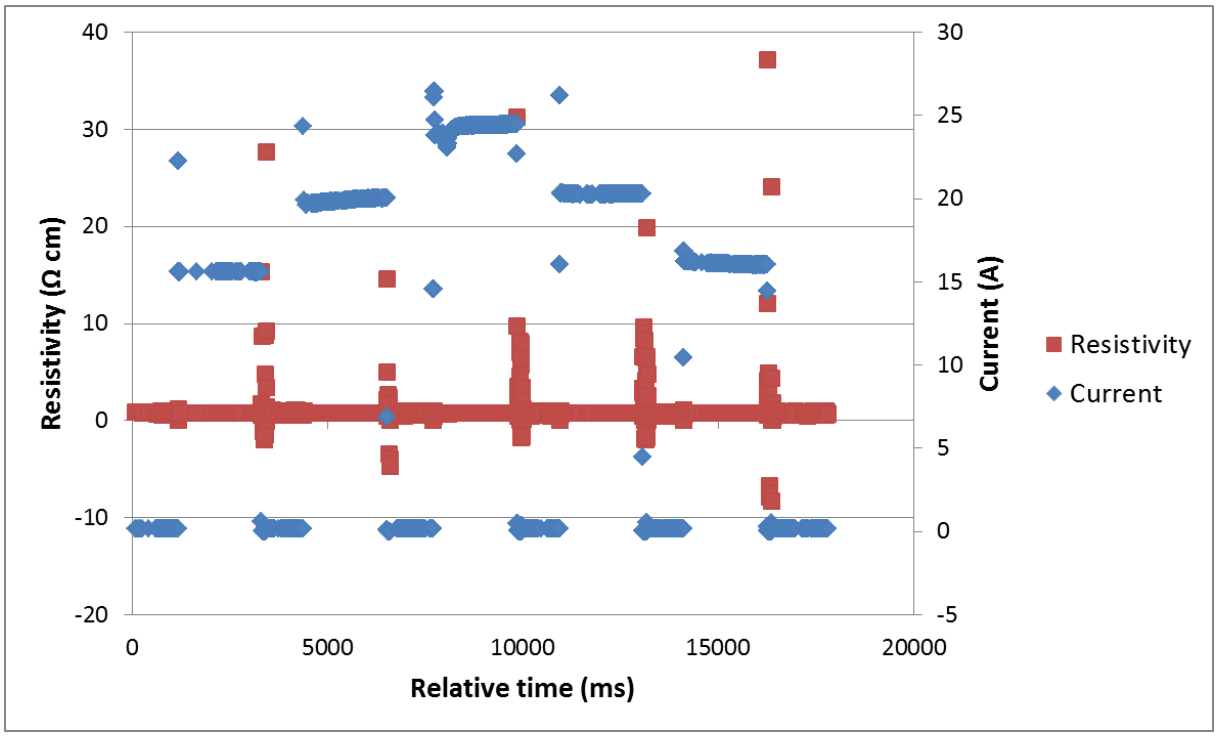

Figure 3.8: Measurements of Elkem-sample #20 at 1003°C, unfiltered

This data was then filtered using the measured current from the outer circuit to determine when actual data was collected. A macro was written which excluded data when the current was below a limit depending on the values from the experiment. After this process the data was again filtered to remove outliers defined as data outside the values of average ±3σ. The

result of the filtration is shown in Figure 3.9. This remaining data was then averaged and used as the resistivity of that temperature.

The remaining outliers, both in the form of either current or resistivity, were manually removed. The macro can be found in APPENDIX A.

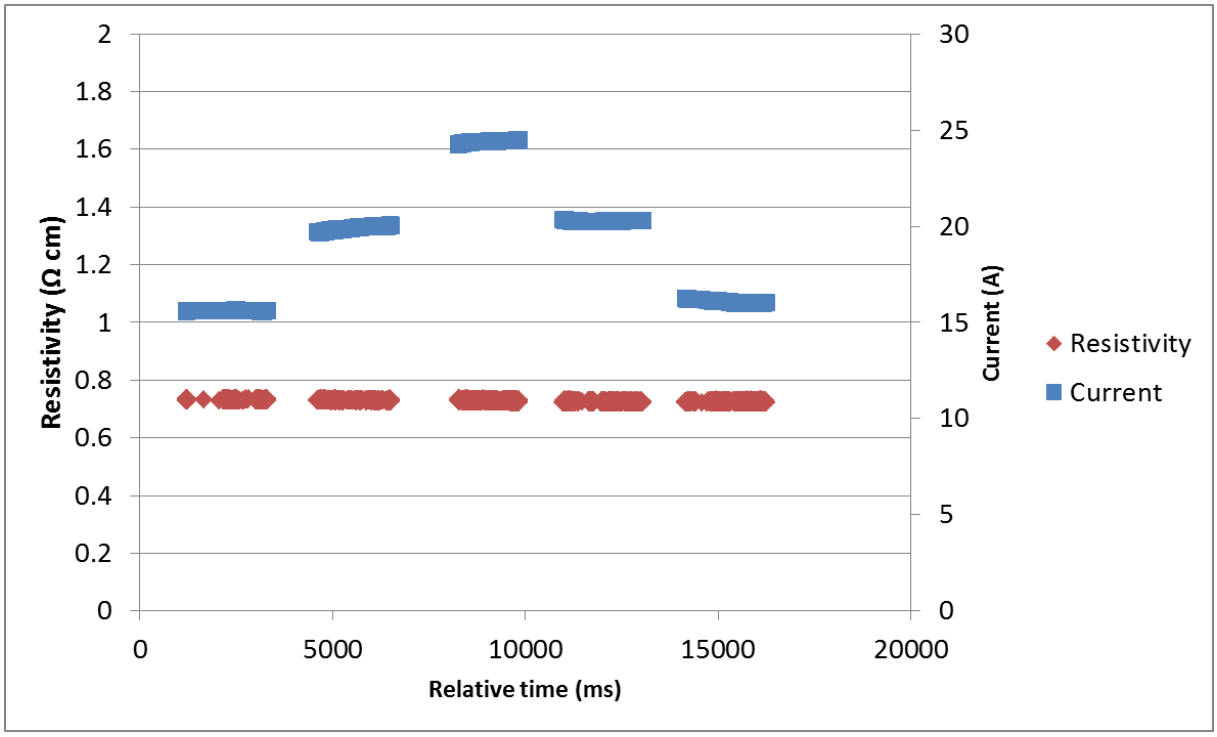

Figure 3.9: Measurements of Elkem-sample #20 at ~1003°C, filtered

3.1.7. Calibration

Calibration of the equipment was performed in the earlier work (Krokstad, 2013) at room temperature, which can be seen in Table 3.3, and in this work on a rod of graphite as a function of temperature. The latter had a specified longitudinal resistivity of $7 \cdot 10^{-4}$ Ω cm, and the results of the measurements can be found in Figure 3.10.

Table 3.3: Calibration data obtained from the graphite rod and the SiC heating element in previous work (Krokstad, 2013)

Sample	Measured values	Manufacturer specification
Graphite rod	7.68 +/- 0.14 µΩm	7 µΩm
SiC	1.98 +/- 0.04 Ω	1.9 Ω

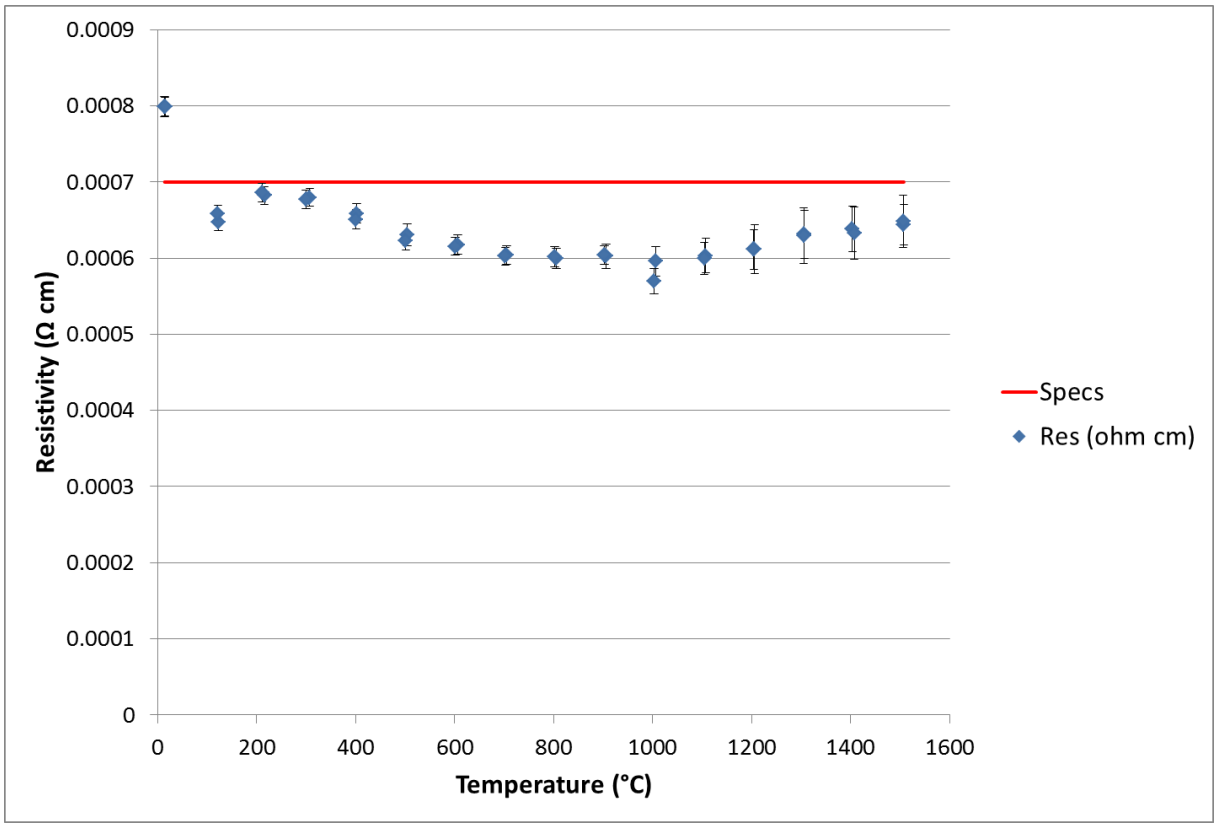

Figure 3.10: Resistivity of graphite as a function of temperature

The same data filtration found in chapter 3.1.6 was applied to the graphite rod. It is evident that the measured resistivity of the graphite rod is very close to the specified value, and shows a fairly constant value with temperature as expected from chapter 2.3.2.

3.2. Compositional analysis

3.2.1. Sample Preparation

Samples were cut into disks, all with approx. the same height as seen in Figure 3.11.

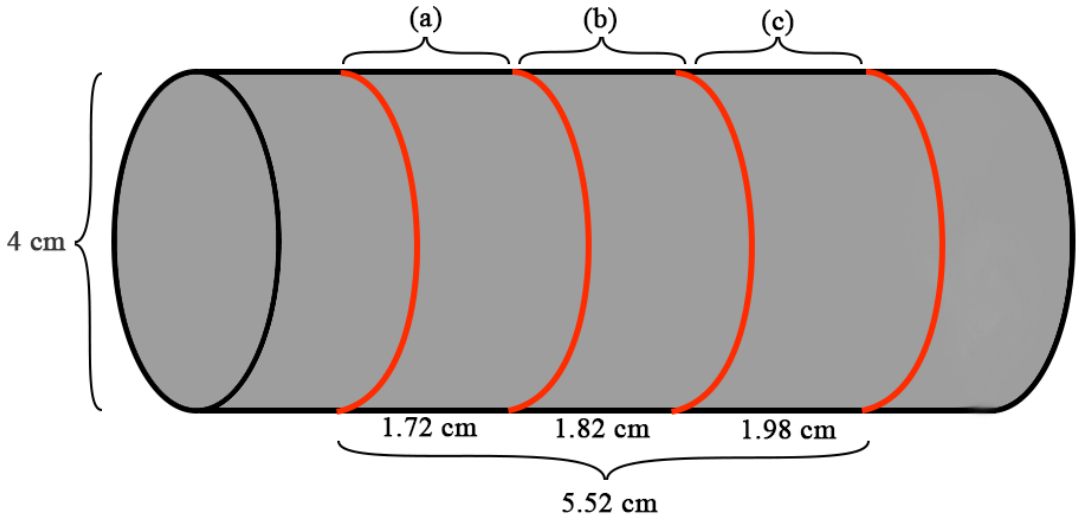

Figure 3.11: Cutting lines in Elkem sample #1

SEM or EPMA using Z-contrast proved to be the fastest and most reliable method of analysing the disk samples. To cover a representable amount of the sample every disk was cut in four parts, see Figure 3.12. The surfaces investigated are indicated as S_x, each representing the surface between the connecting parts.

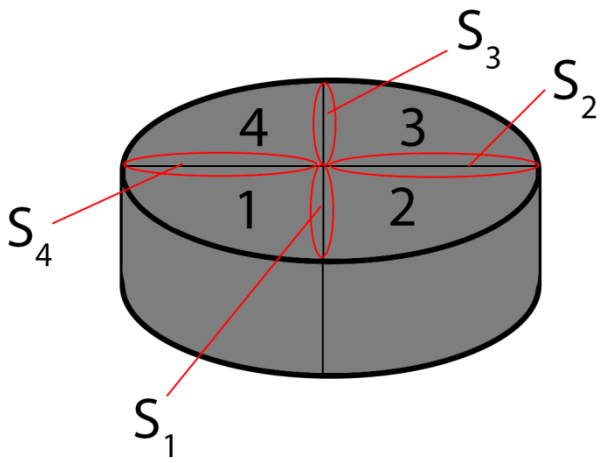

Figure 3.12: Cutting of samples for SEM

Each piece of the disks was mounted in EPOFIX™ and polished with the steps seen in Table 3.4.

Table 3.4: Grinding and polishing of samples for SEM/EPMA

Step nr.	Grinding/Polishing medium	Roughness
1	Diamonds sintered onto steel plate Piano	220
2	DiaPro Allegro	9 µm
3	DiaPro Dac	3 µm
4	DiaPro Nap	1 µm

Each sample proved different needs for polishing times to achieve required finish, and as such no standardised polishing-time was used.

3.2.2. SEM/EPMA

SEM (Zeiss Supra 55VP) and EPMA (JXA-8500F) both were used to take atomic number contrast images (Z-contrast). These images are obtained through the collection of backscattered electrons, being scattered by elastic collisions with the nuclei. Heavy elements scatter the electrons more efficiently, making them seem brighter than lighter elements. To obtain less charging, an effect that occurs with non-conductive materials, all samples examined in the EPMA and SEM (with the exception of E#1 and E#41) were coated with carbon.

The images obtained had five different shades of gray, representing a metallic (FeSi) phase, silicon, SiO_2, SiC and pores from white to black respectively. It was assumed that area-fraction of each phase is equal to the volumetric fraction and the former calculated using i-Solution DT.

i-Solution DT uses a manually set threshold of intensity from “0” (black) to “65536” (white), but most images needs a certain amount of filtering. Sample F#33 is shown as an example below.

The filter sharpens the edges and smoothen the contrast within the different phases making it easier to apply the threshold. This will, however, result in a loss of the smallest particles/pores. Each threshold is then given a colour, and after application an image seen below is obtained. Another side-effect of the filtering is the inevitable boundary-intensities. Between the bright and dark phases, an average intensity will appear which may correspond with another phase, causing the accuracy of these images to be within 1%.

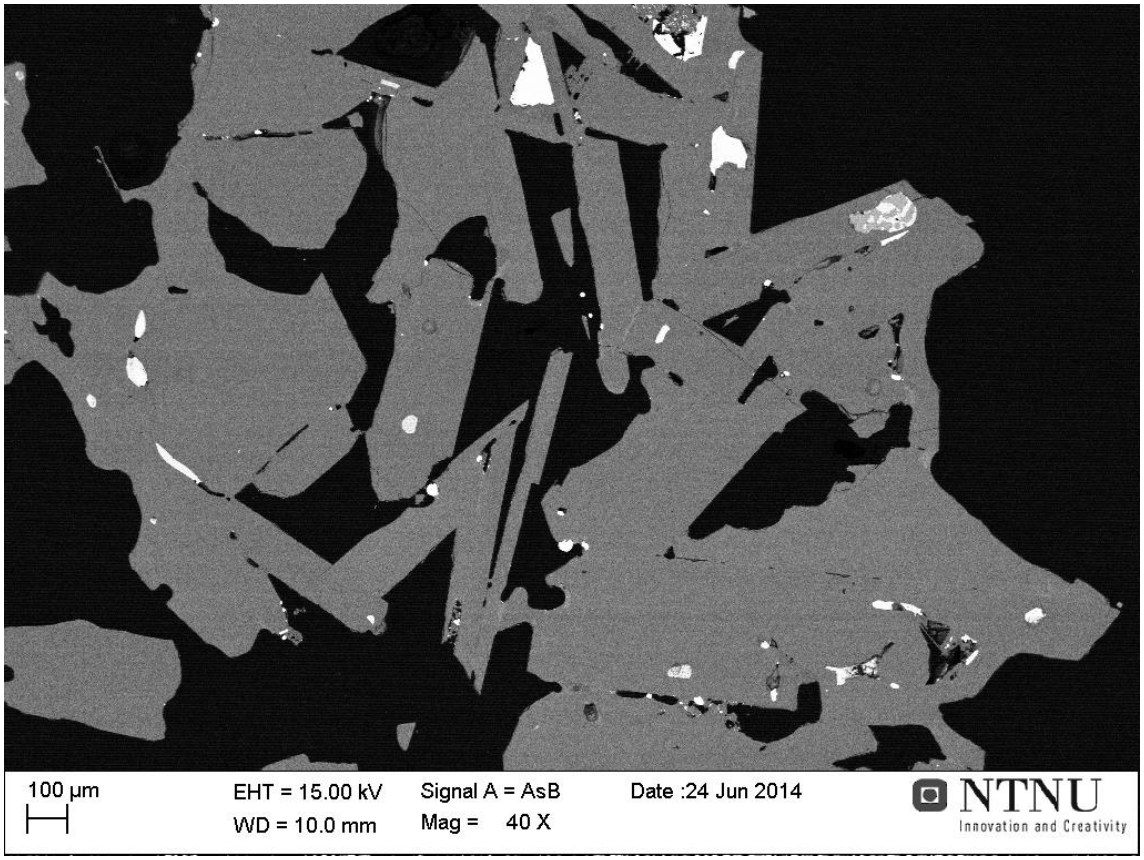

Figure 3.13: Image 2-10 from sample F#33, original image

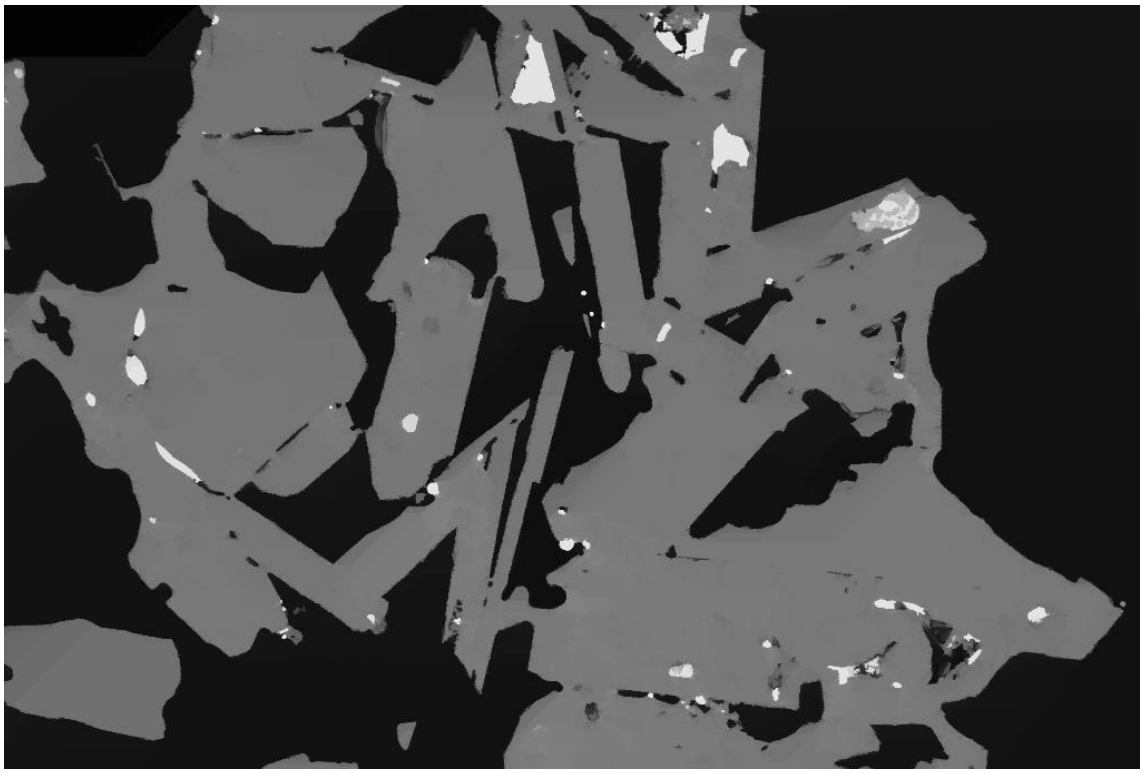

Figure 3.14: Image 2-10 from sample F#33, filtered

Figure 3.15: Image 2-10 from sample F#33 with thresholds applied

3.2.3. XRD

X-Ray Diffraction proved ideal for analysis of the metallic phase formed beneath the samples during experiments, but unsuitable for the bulk disk-samples. Pulverisation of the SiC was not attempted due to the hardness of the material. After complete pulverisation with mortar, the metal was dispersed on a single crystal sample holder with alcohol.

The equipment used was the A-unit, a Siemens D5005, at the powder diffraction lab at the institute of material science and technology. Measurements were done with the angle range of 5-80° over three hours.

Phases were identified with the Bruker EVA.DIFFRAC V3.2 software. The software used by the laboratory to analyse volume fraction of species from a XRD spectrum is Bruker's EVA.TOPA. TOPAS assumes the sample has a perfectly flat surface, and has no function to correct for porosity. For porous samples, the porosity interferes with the measurements and peaks will appear at incorrect angles. XRD was therefore concluded to be futile for the SiC-samples.

CHAPTER 4. RESULTS

4.1. Resistivity

The data obtained for the temperature-dependency in resistivity of SiC is found in Figure 4.1, a closer look at the high-temperature-data is seen in Figure 4.2.

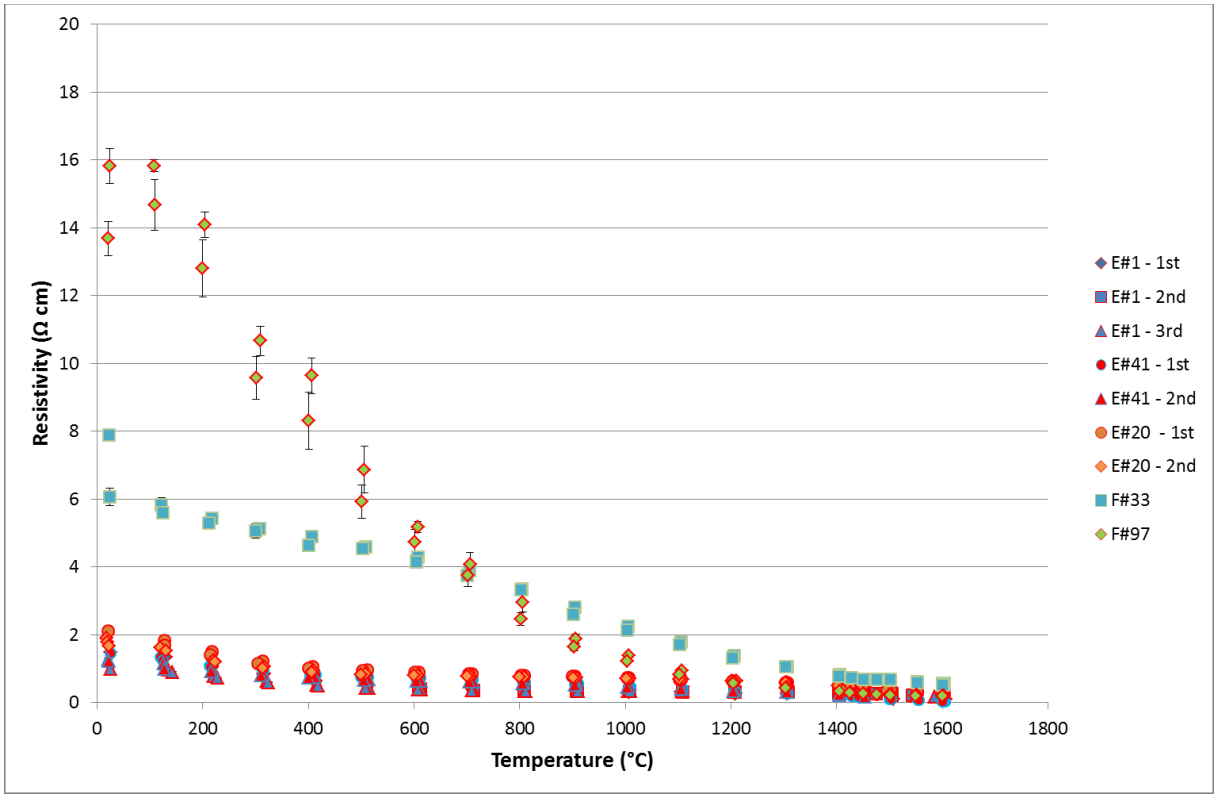

Figure 4.1: The resistivity of all industrial-SiC-samples as a function of temperature
E#1 – 1st is from the earlier works (Krokstad, 2013)

The resistivity of the SiC from the industrial crusts is clearly dependent on temperature, and while the values at high-temperature range seem to approach the same range, a large difference between samples is seen at low temperatures. As the Finnfjord-samples have a larger span of resistivites, Figure 4.3 gives the Elkem-samples alone to give a better picture of their dependence on temperature. Equipment error caused values below 600°C for E#1 2nd test to be wrong and they are omitted from all figures.

For the Elkem-samples a decrease in low-temperature resistivity is seen with each test, this meaning the resistivity decreased with subsequent heating of the sample for each experiment.

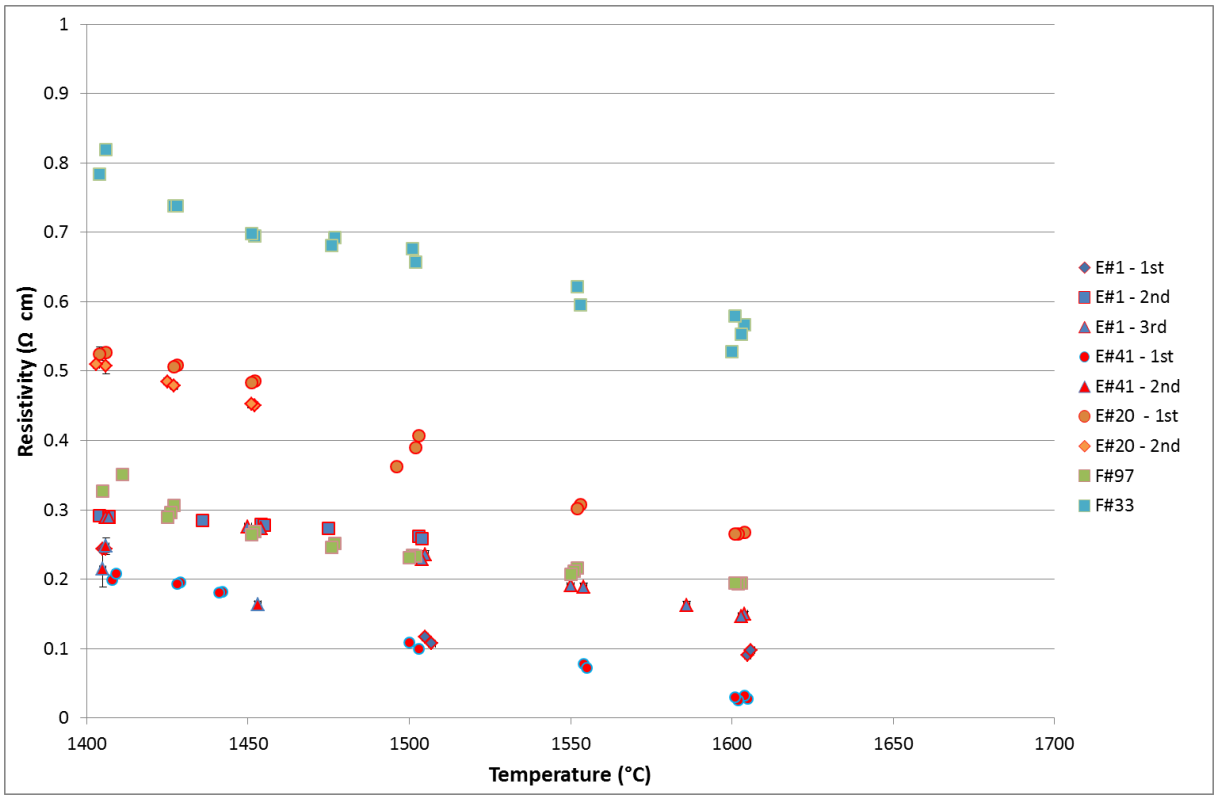

Figure 4.2: The resistivity of all industrial-SiC-samples as a function of temperature, high temperature range

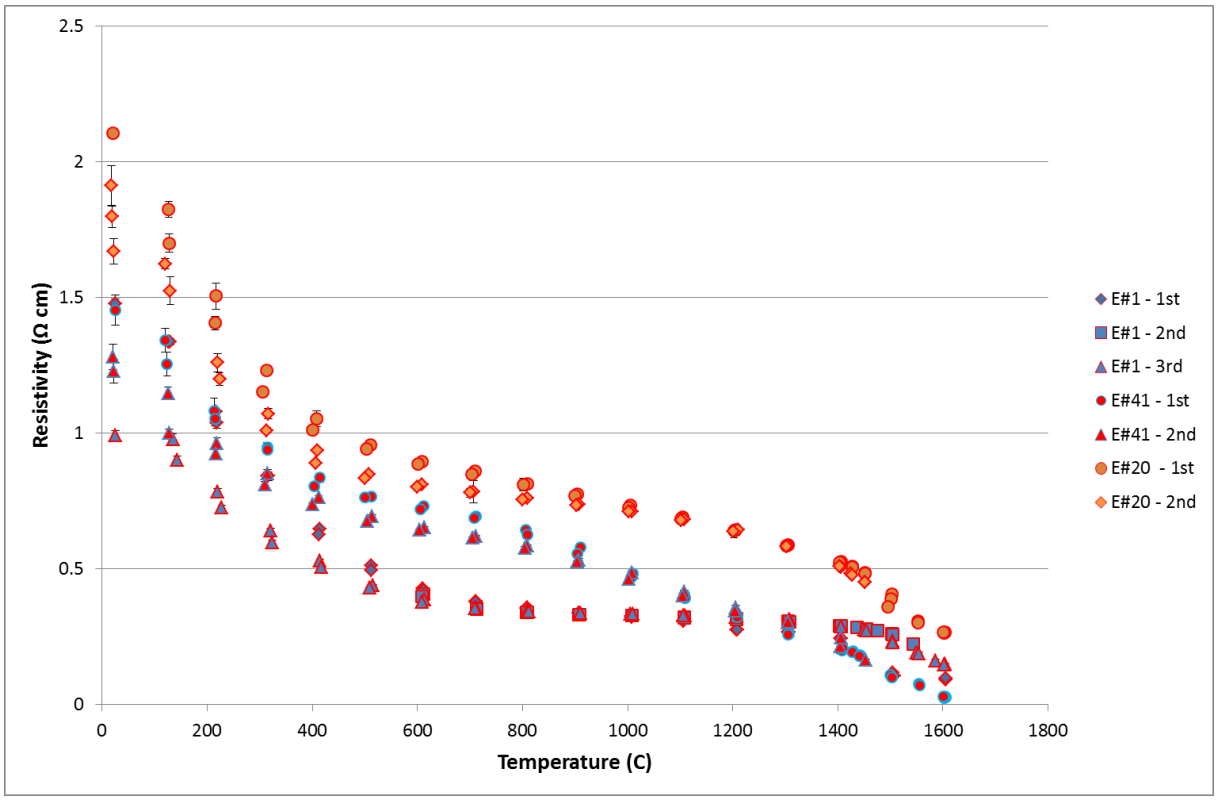

Figure 4.3: The resistivity of the Elkem industrial-SiC-samples as a function of temperature

4.2. Composition

4.2.1. SEM/EPMA Z-contrast

Final composition

The final, average composition of each sample disk, after all high-temperature experiments, can be found in Figure 4.4. As sample F#97 was so small only one disk was produced, each part of this disk is shown in the figure. The standard deviation used is the standard deviation of data from all images of the specific disk. Typically 80-90% of the sample disk was investigated. Figure 4.5 through Figure 4.9 shows representative Z-contrast images of the samples, more images can be found in APPENDIX B.

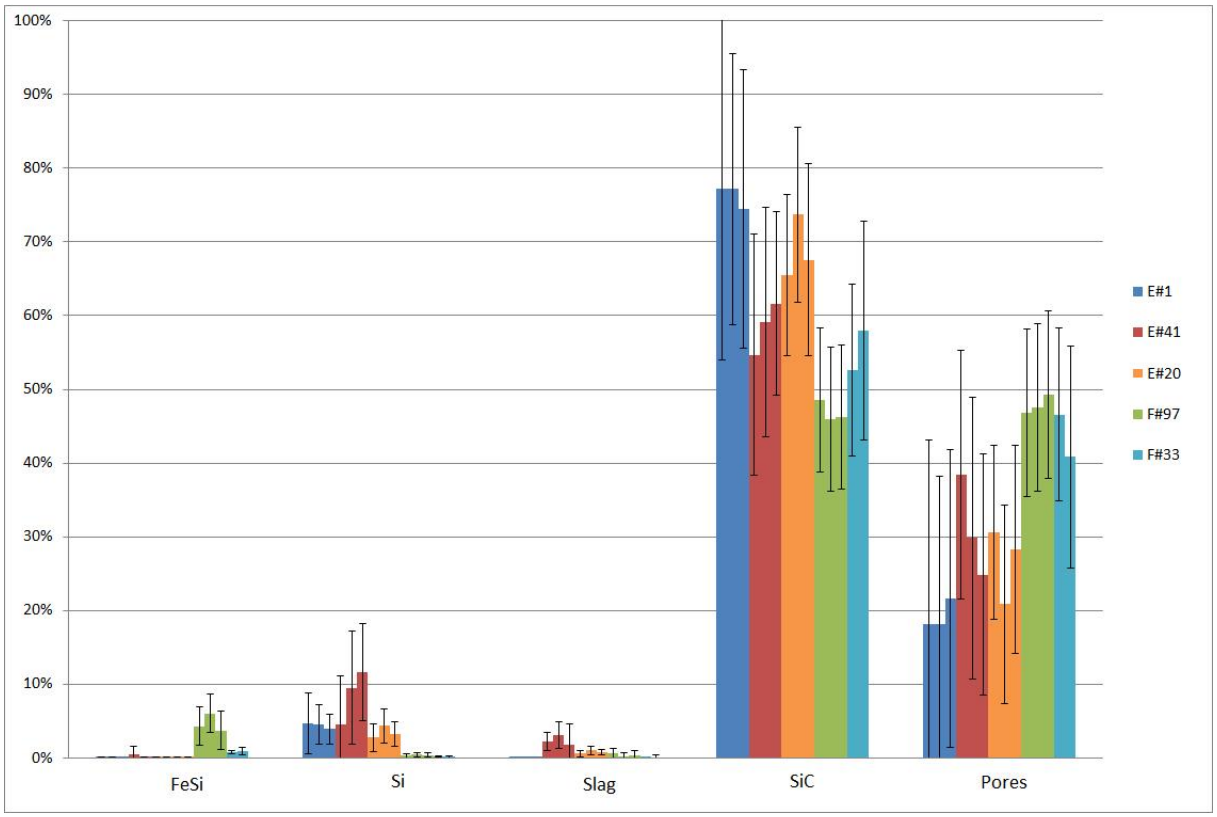

Figure 4.4: Composition of each SiC-sample by volume-percent

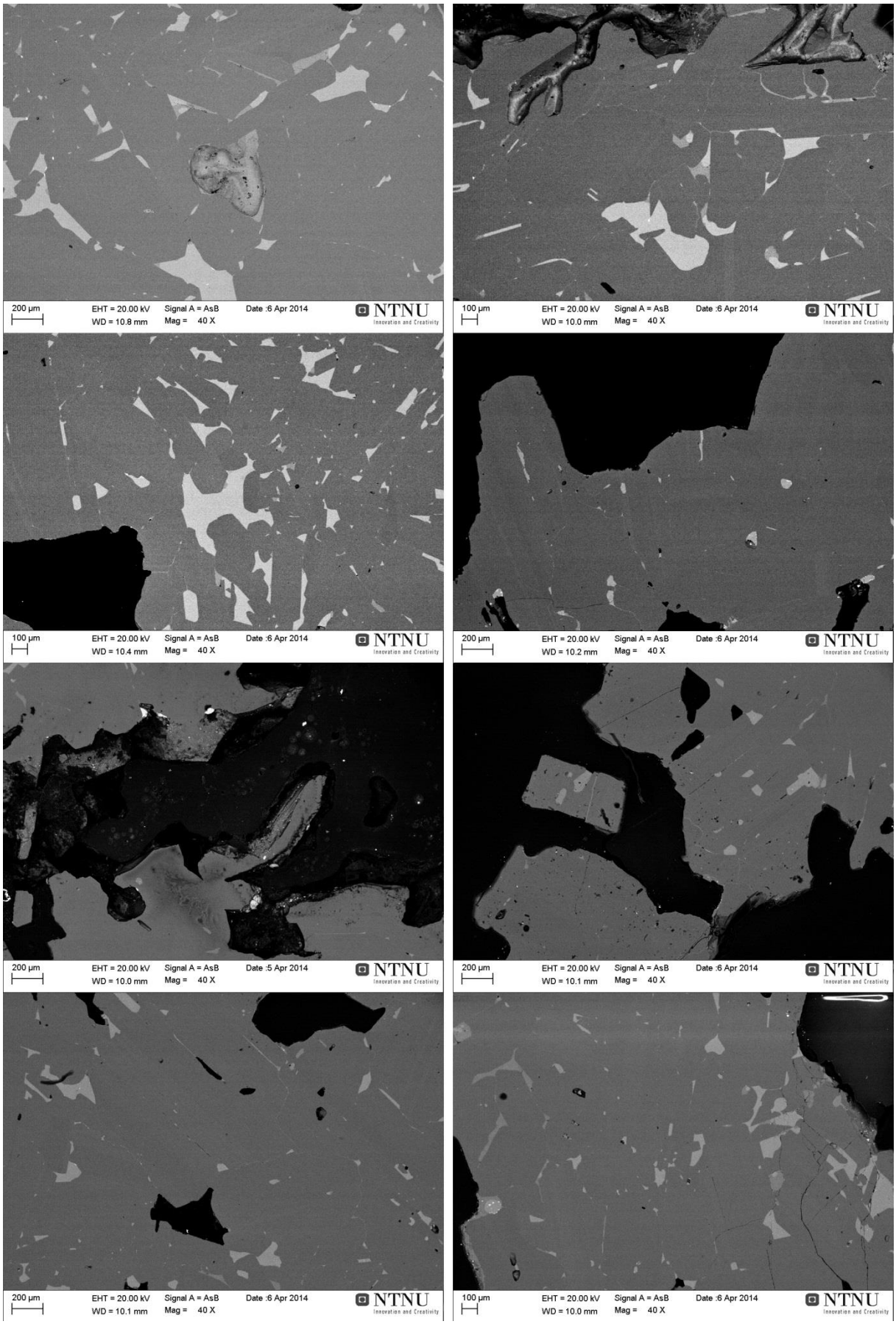

Figure 4.5: Representative images from sample E#1

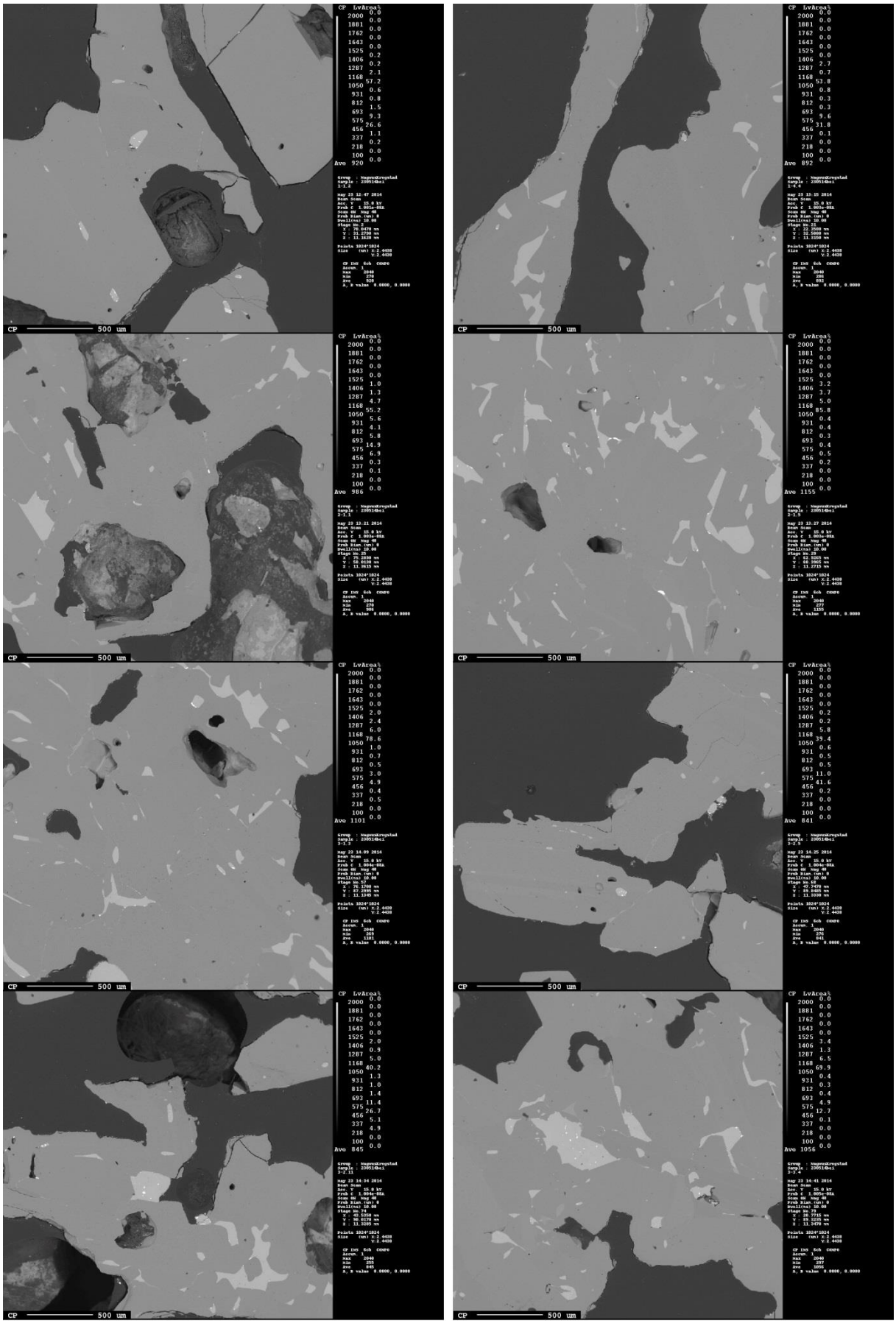

Figure 4.6: Representative images from sample E#20

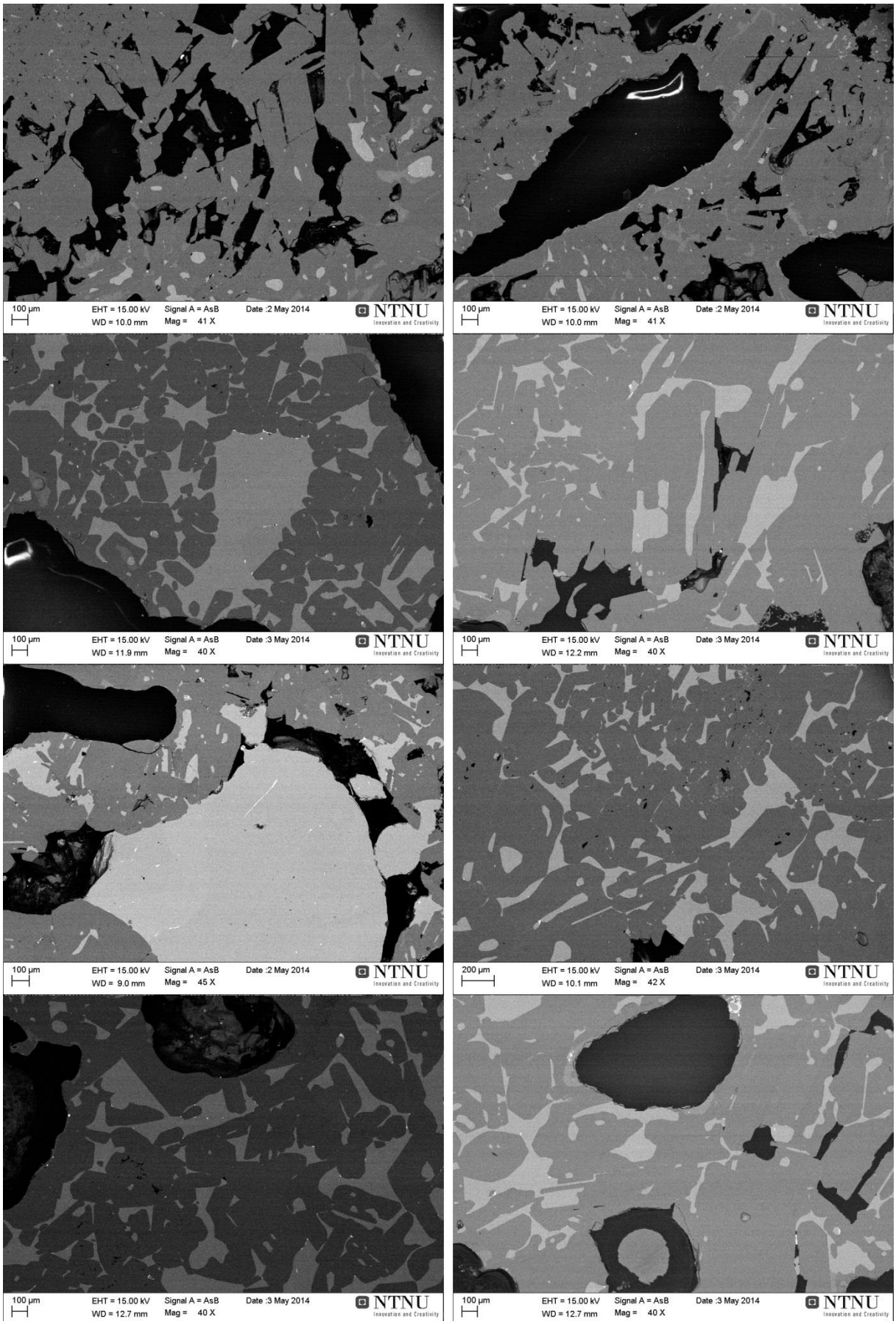

Figure 4.7: Representative images from sample E#41

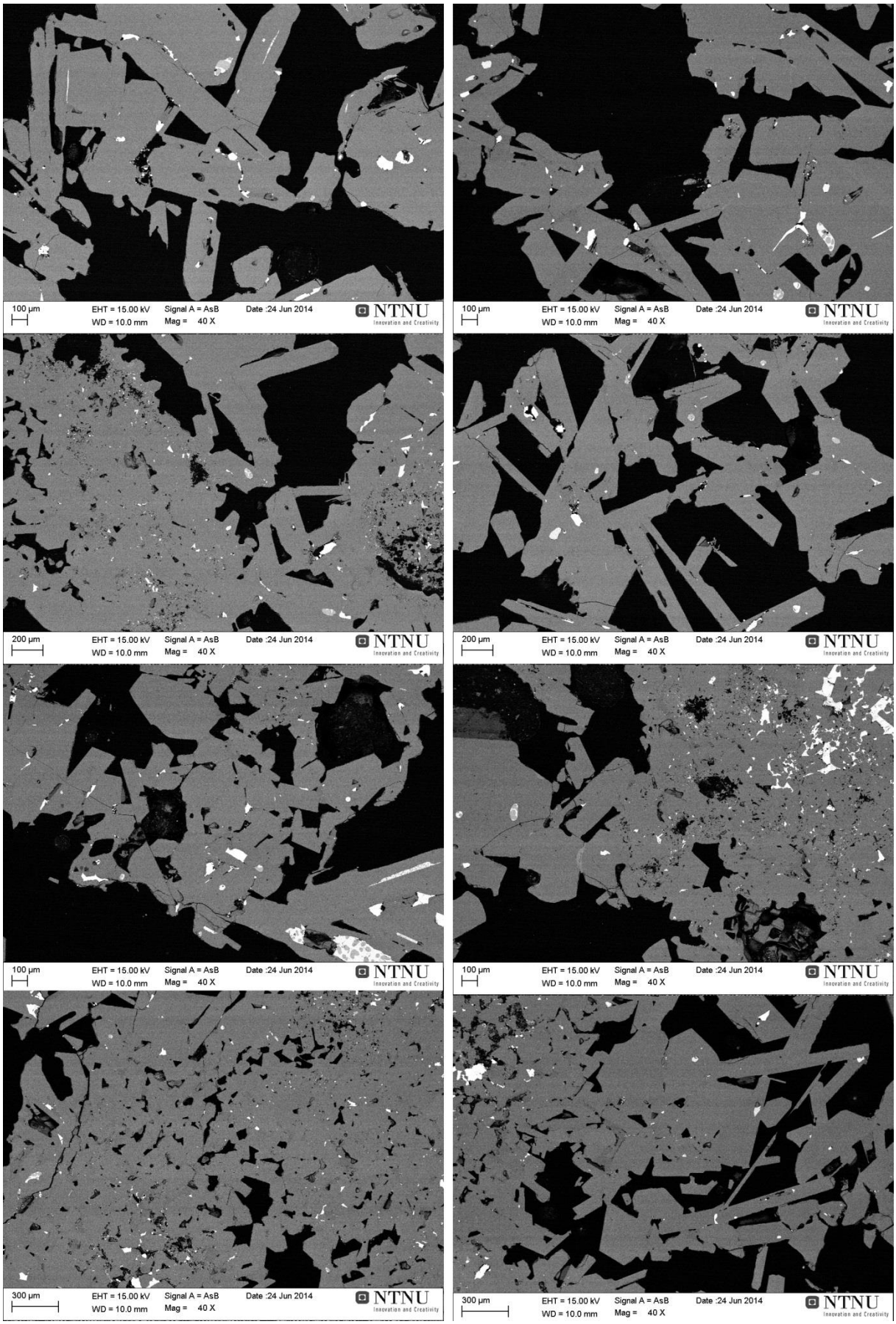

Figure 4.8: Representative images from sample F#33

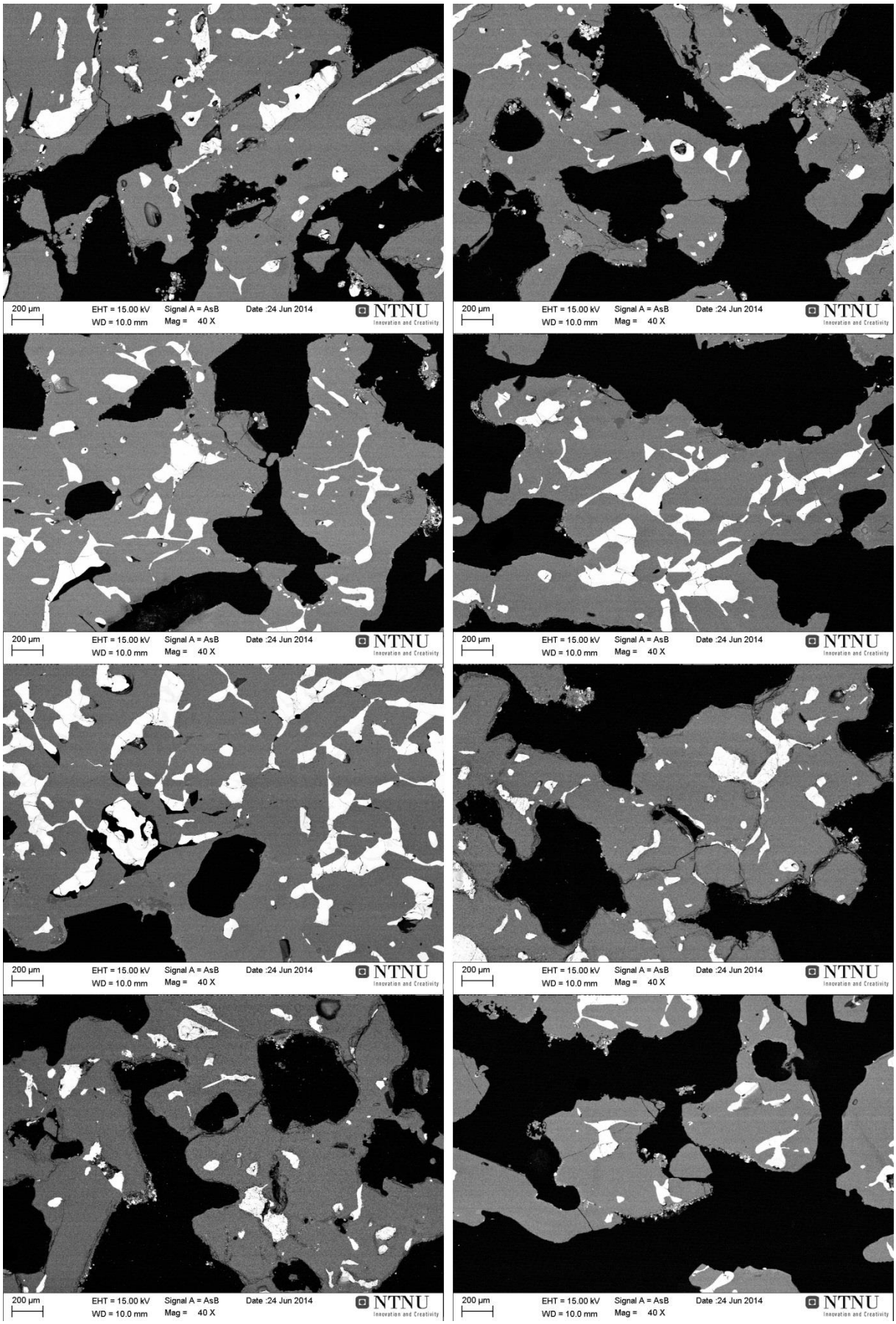

Figure 4.9: Representative images from sample F#97

Three important observations can be made from Figure 4.4. First is the uneven composition in between the disks of each sample and also within the disks as seen in the standard deviation. While the disks varied in-between each other, none of the values were outside the standard deviation of each disk in and of itself. The difference between the samples was also found to be within the standard deviation of each other with respect to SiC and pores, while the FeSi-, Si- and SiO_2-content varied outside. While this deviation could be seen on as a factor of uncertainty of the measurement, it is clear to see in Figure 4.5 through Figure 4.9 that the sample composition varied highly which would lead to a high standard deviation.

Second, the samples from the Finnfjord FeSi-furnace has much more FeSi than Si while the Elkem samples, coming from a MG-Si, furnace contains barely any FeSi but a significant amount of Si.

Third, by comparing the composition of the samples to the resistivity it can be observed that the amount of FeSi/Si, which will be liquid above 1414°C, corresponds with the resistivity at high temperature. More FeSi/Si leads to lower resistivity at high temperatures, with the exception of sample E#1 which has a lower resistivity than F#97. The total amount of FeSi + Si can be seen in Figure 4.10 along with the resistivity of the respective samples.

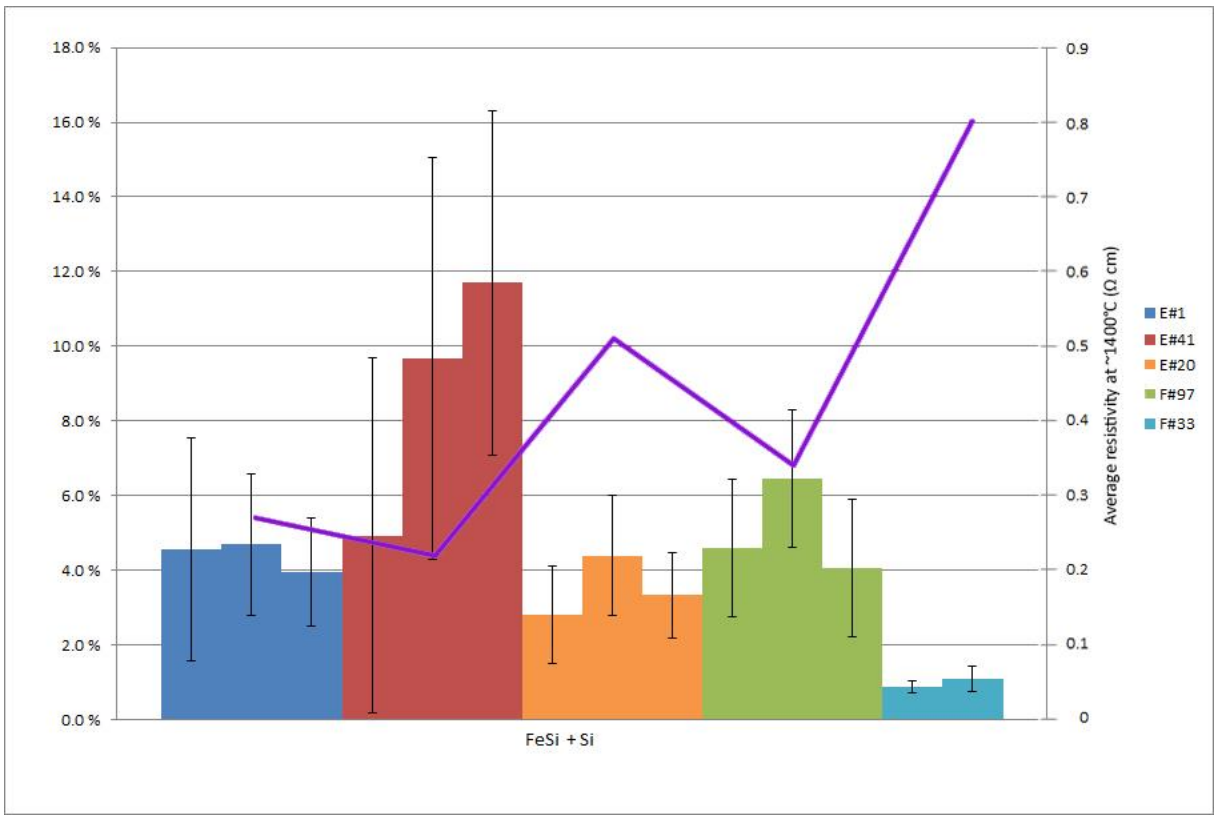

Figure 4.10: FeSi + Si content

Change in composition from heating in experiments

Even though the materials originate from a furnace and have been subject to temperatures higher than those reached in the experimental work of this thesis, samples were investigated before and after heating. As the resistivity-test samples could not be investigated on directly to give data before heating, new samples were taken around the hole left from the core sample and investigated as "before"-samples. Figure 4.12 through Figure 4.13 show the composition of the samples before and after heating from experiments. Sample E#1 was not included due to the loss of the material close to the drill site. The standard deviation used is the standard deviation of data from all images of the specific disk or sample.

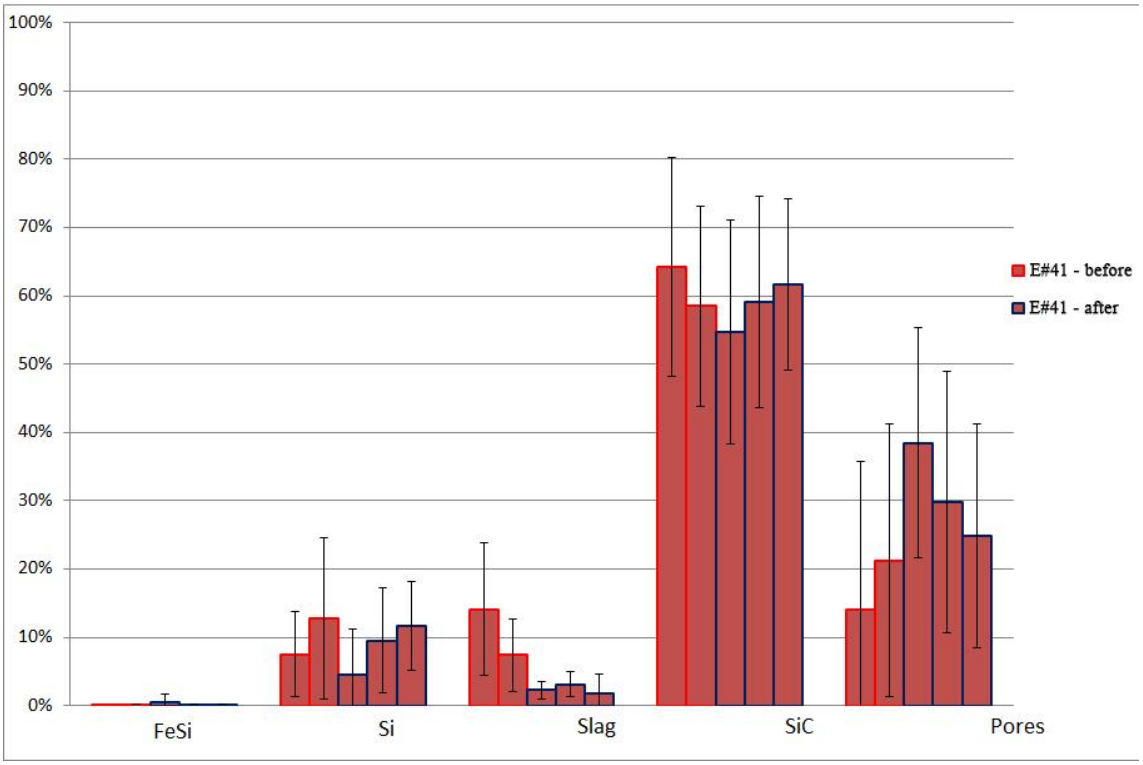

Figure 4.11: Composition of disks from sample E#41 before and after testing

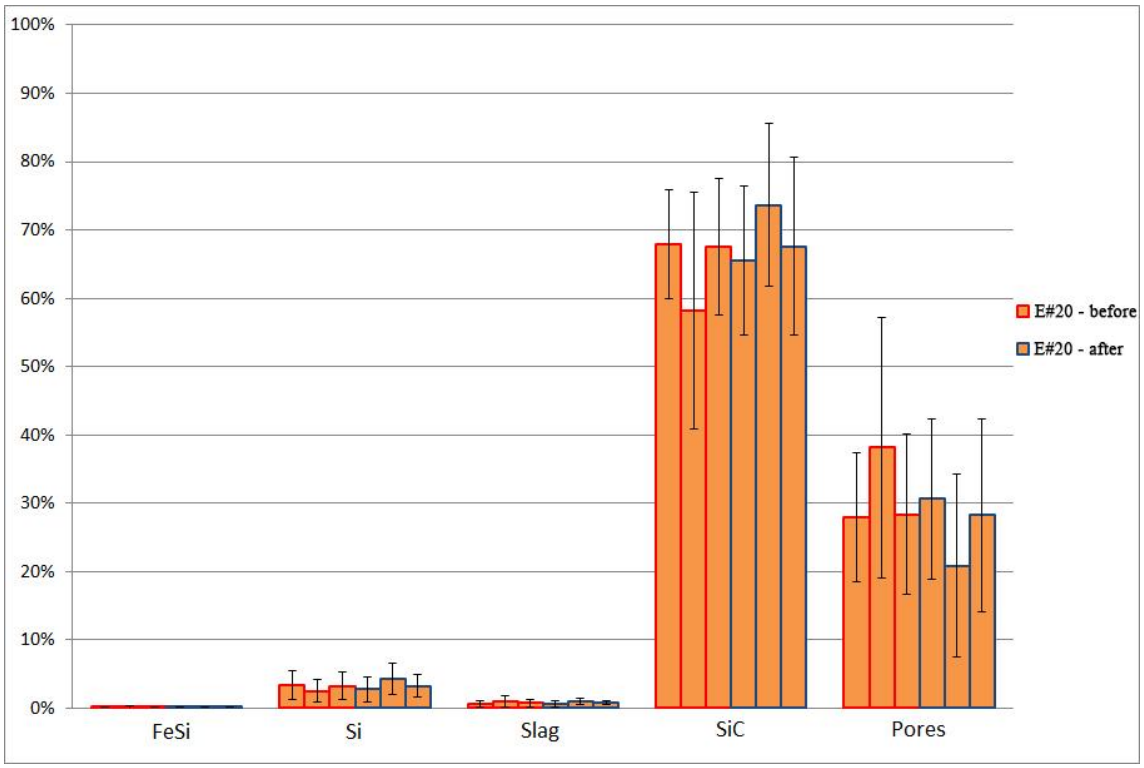

Figure 4.12: Composition of disks from sample E#20 before and after testing

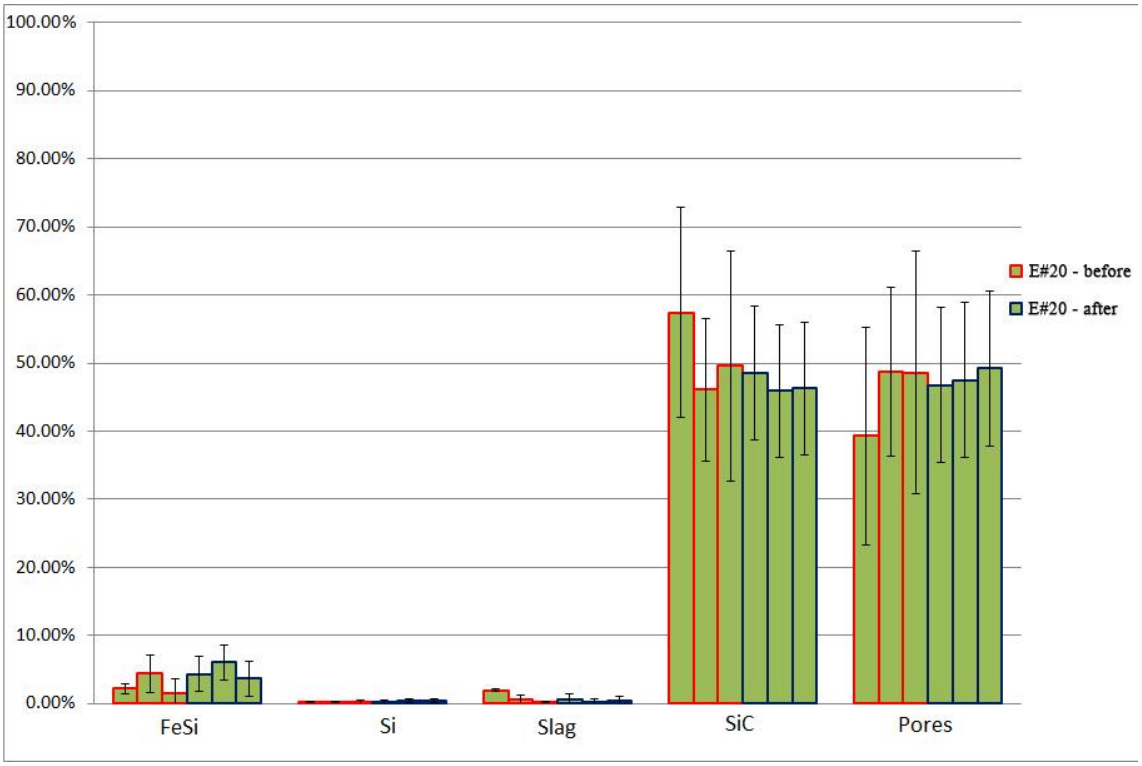

Figure 4.13: Composition of disks from sample F#97 before and after testing

All of the samples show some difference in the composition before and after, but samples are very inhomogeneous as seen by the standard deviation and no major change is observed that cannot be explained by this.

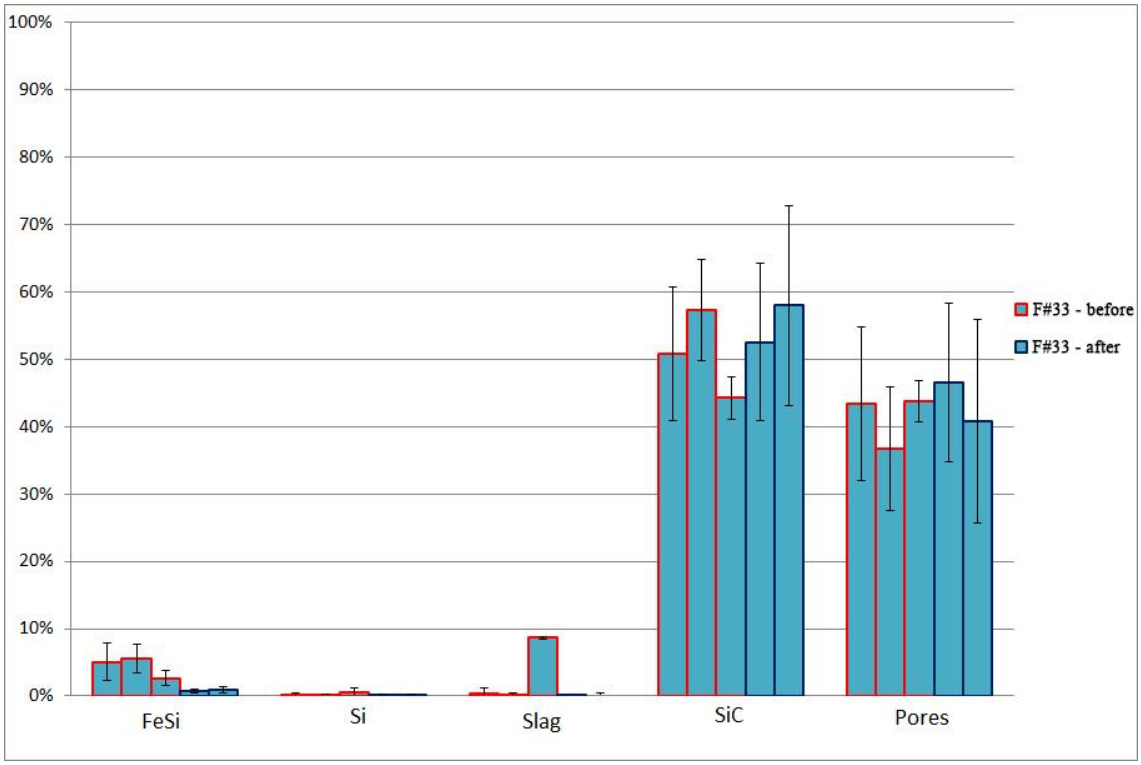

Figure 4.14: Composition of disks from sample F#33 before and after testing

4.2.2. EDS-analysis on each phase

In chapter 3.2.2 it is shown how the area fraction of each phase was found, and the assumption based on the knowledge of the phases and their average atomic number could be used to determine which phase is what. But in order to confirm this, EDS analysis was performed on several of the phases.

From sample E#20, the following image was taken. The red area is enlarged in Figure 4.16.

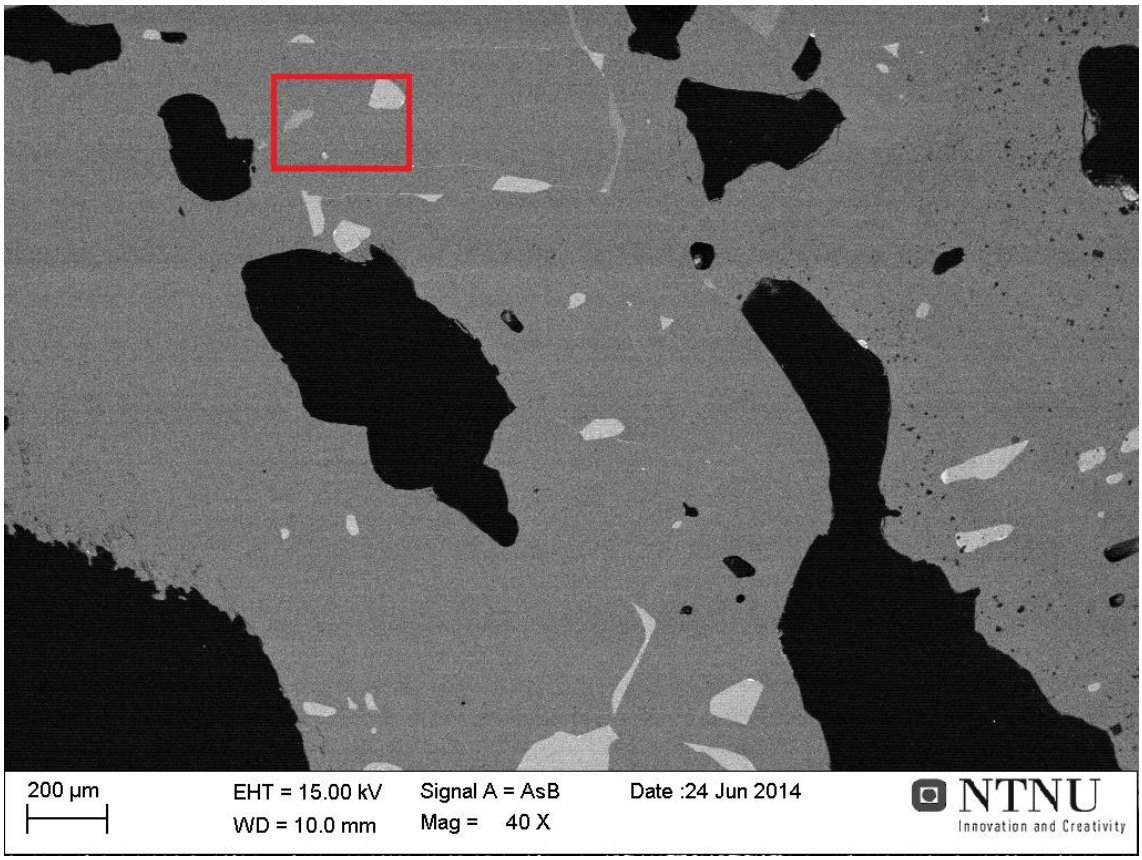

Figure 4.15: Z-contrast image of sample E#20

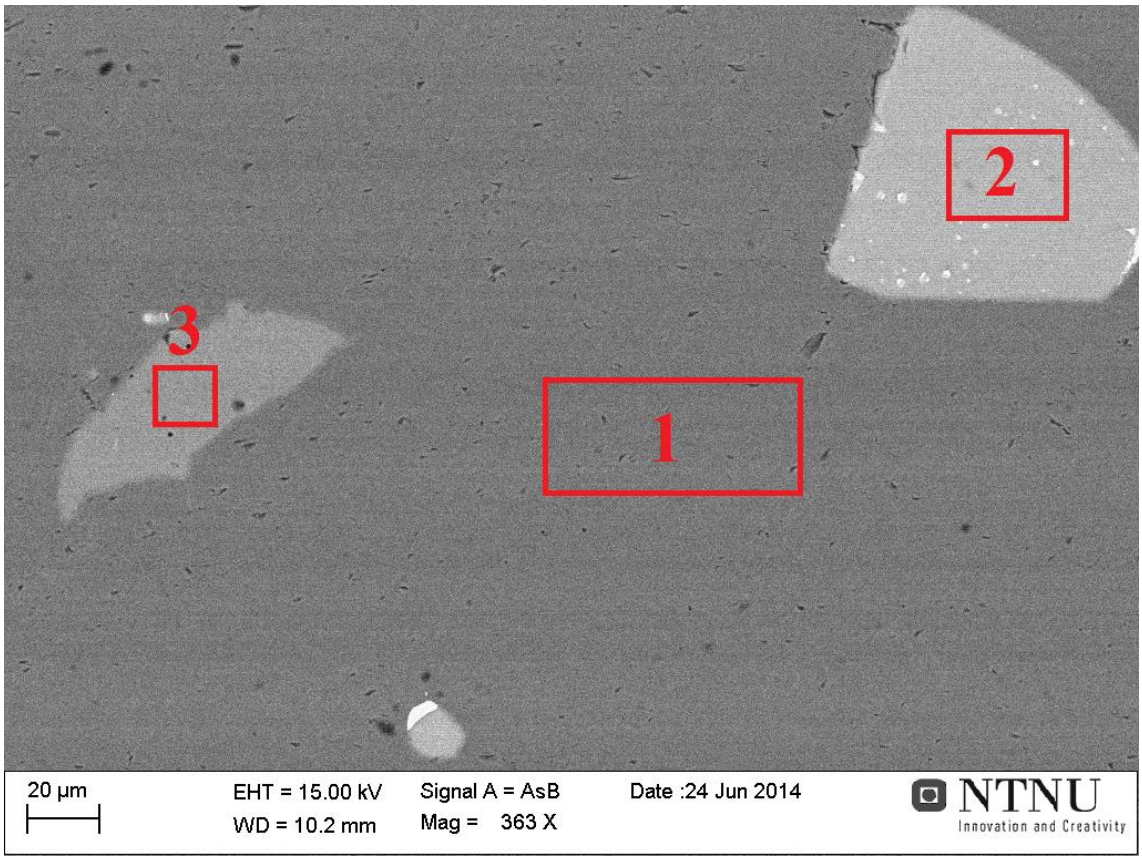

Figure 4.16: Red area of Figure 4.15

EDS analysis was performed on each of the three areas in Figure 4.16, giving the following spectra:

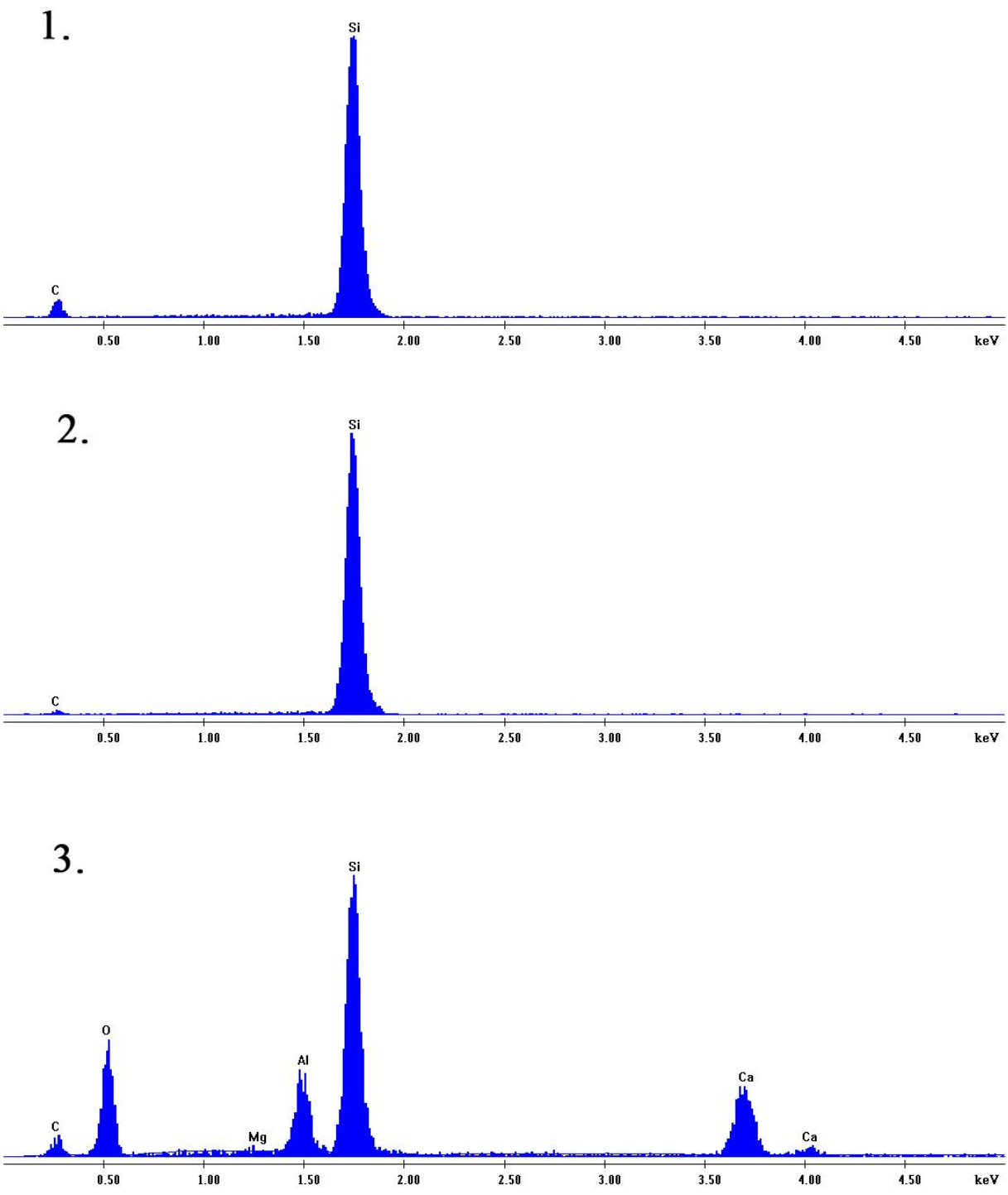

Figure 4.17: EDS spectra from the three areas in Figure 4.16.

As the samples were coated with carbon, a trace amount of carbon is seen in the otherwise pure silicon of area 2. Area 1 is SiC. Area 3 is slag consisting of Mg-, Al-, Si-oxides. The higher amount of C in the slag area compared to Si could be due to the emission depth of the electron beam including some SiC beneath the slag. No EDS was performed on the small bright white particles, as they were assumed to be any of the combinations of Fe_xSi_y as predicted by the Fe-Si-phase diagram (Figure 5.5).

Figure 4.18 shows sample E#41, where an eutectic structure of the slag can be seen. This structure was not investigated further.

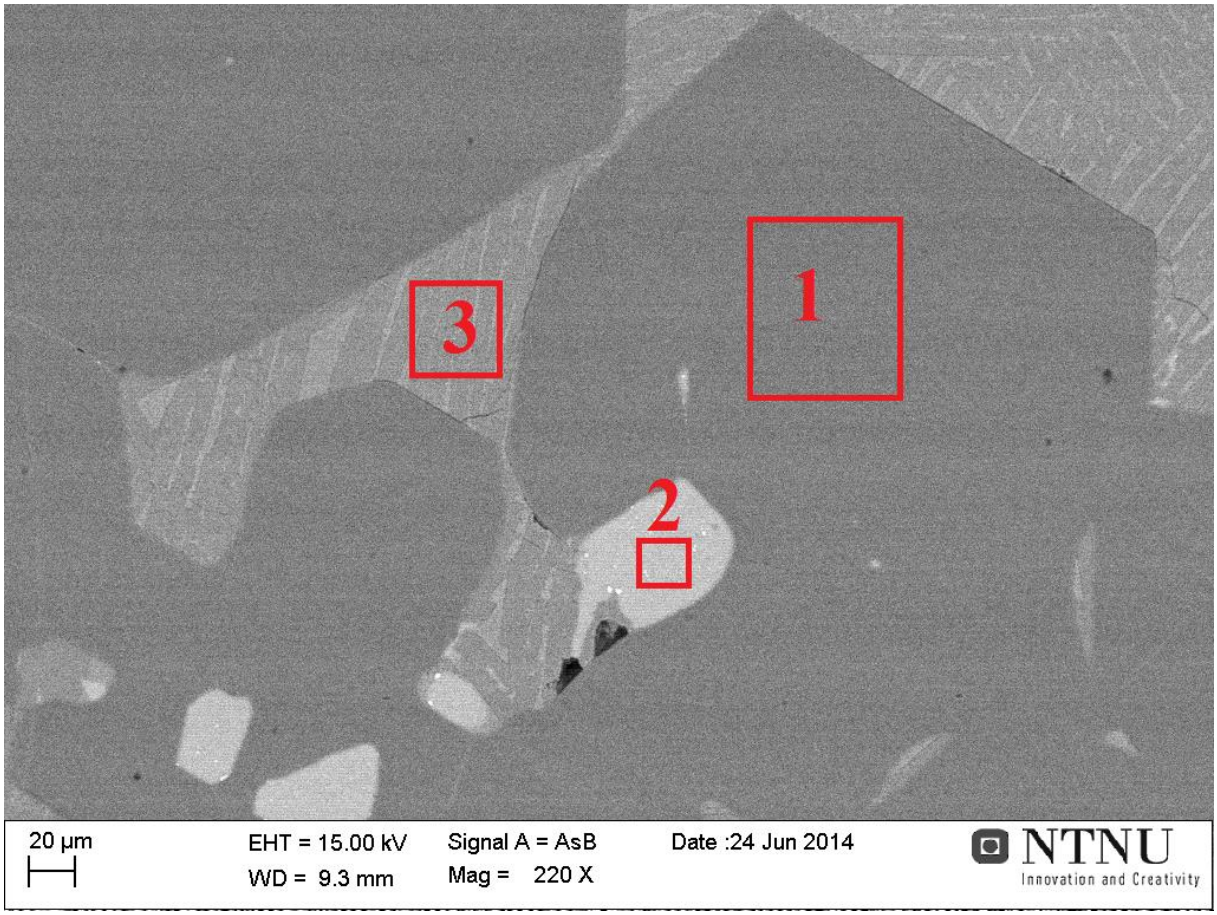

Figure 4.18: Z-contrast image of sample E#41

The same peaks appear in sample E#41 as in E#20, as seen in Figure 4.19, proving the assumption of the four major phases to be correct.

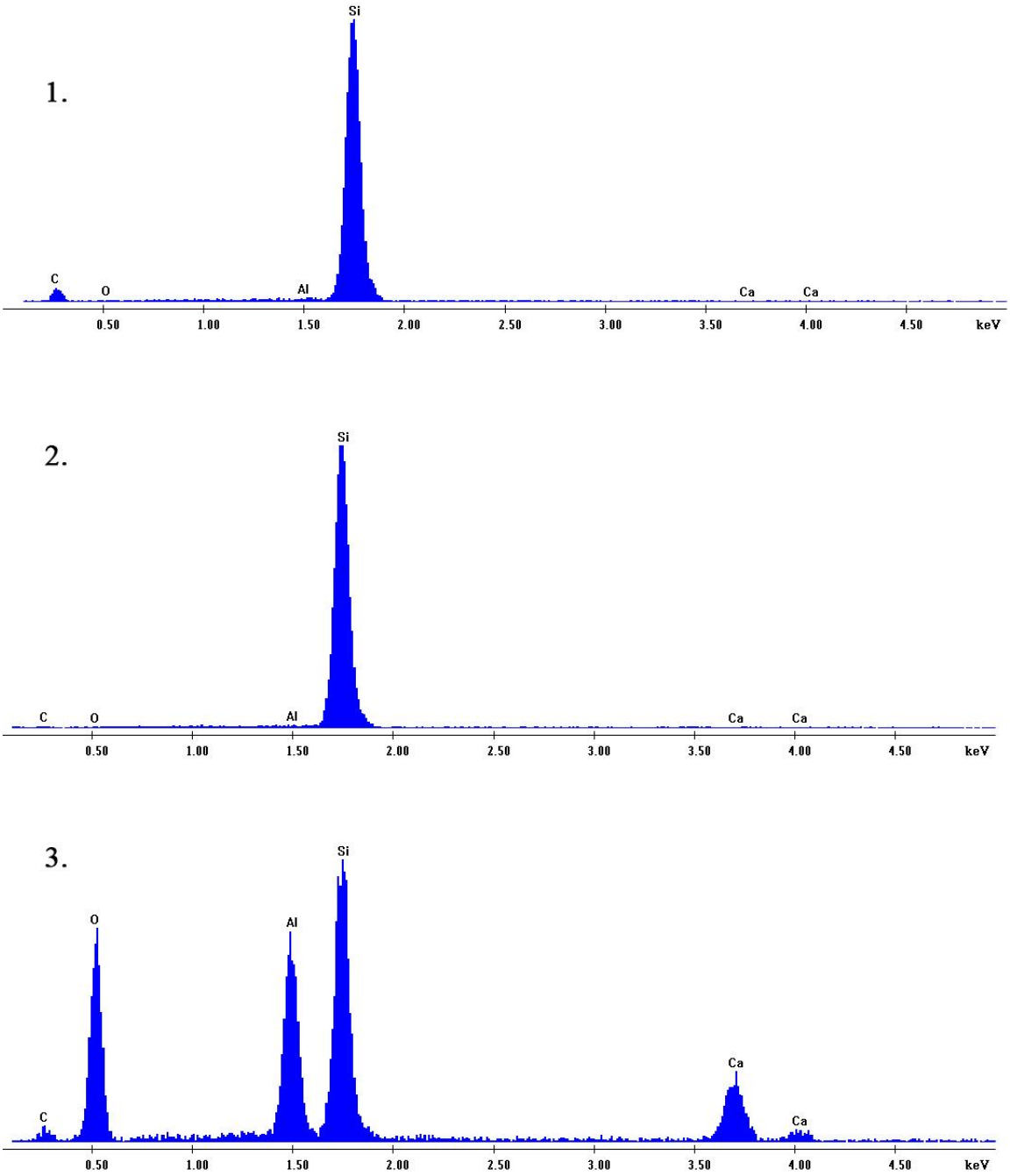

Figure 4.19: EDS spectra from the three areas in Figure 4.16.

The major difference between the Finnfjord and the Elkem samples regarding composition was the FeSi, which was abundant in the Finnfjord-samples but only sporadic in the Elkem-samples. Figure 4.20 and Figure 4.21 show the Z-contrast images of sample F#33, while Figure 4.22 and Figure 4.23 show the respective EDS-spectra for the areas in Figure 4.21.

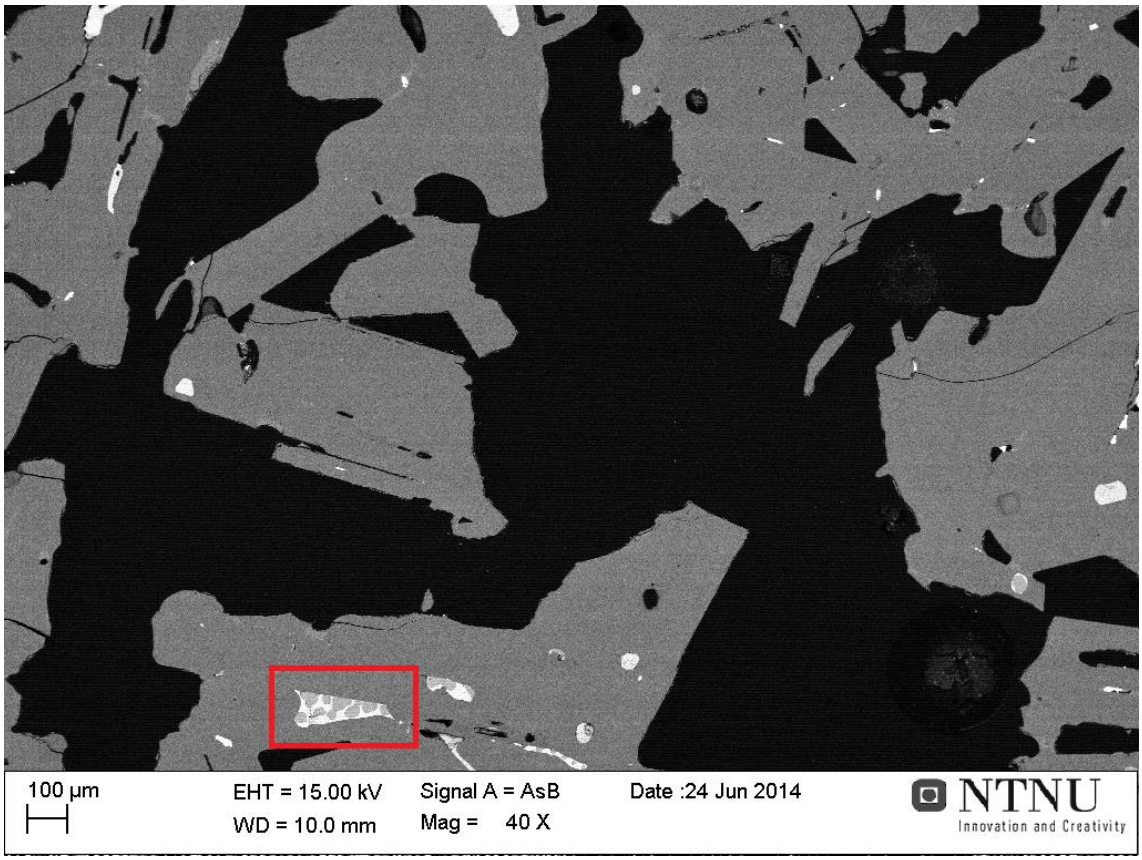

Figure 4.20: Z-contrast image of sample F#33

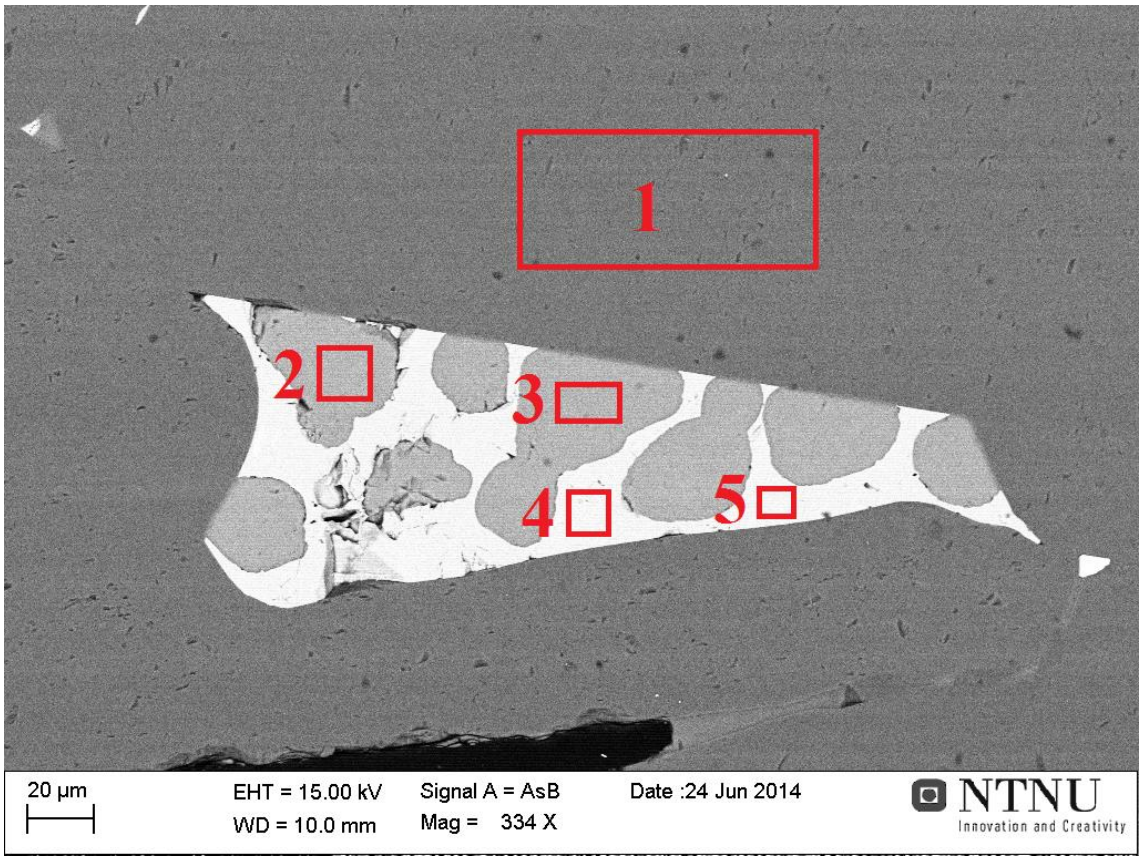

Figure 4.21: Red area of Figure 4.20

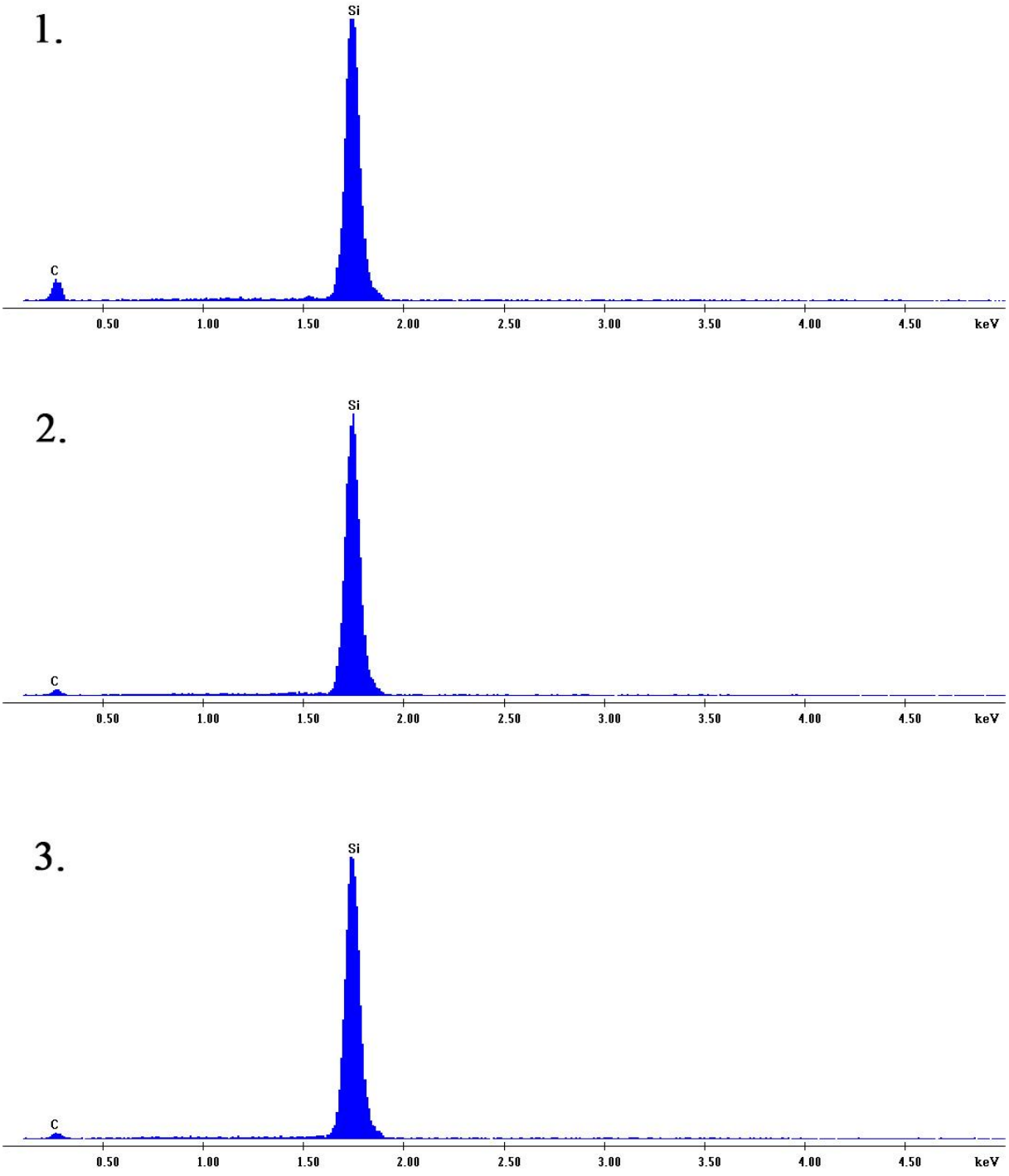

Figure 4.22: EDS spectra from the three areas in Figure 4.21

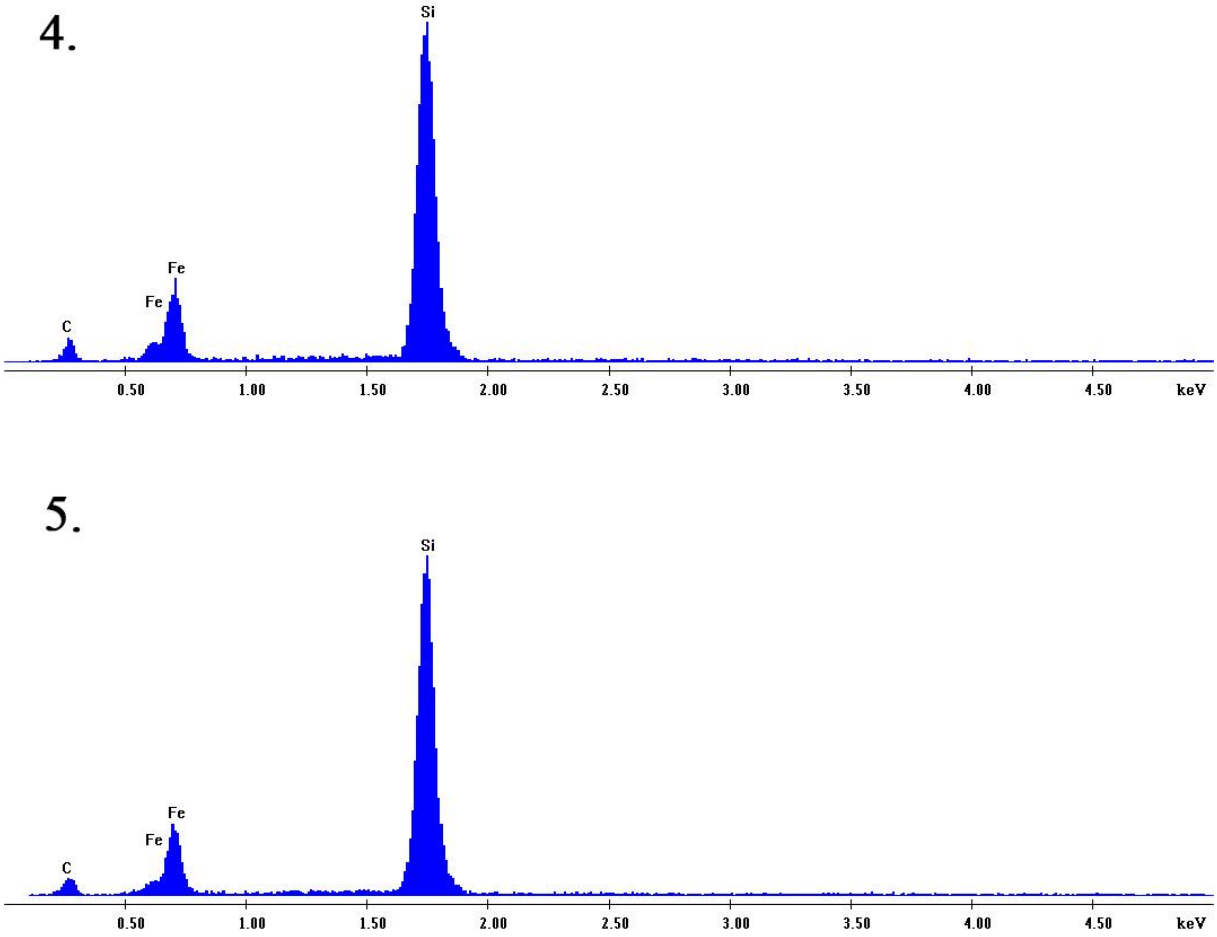

Figure 4.23: EDS spectra from the three areas in Figure 4.21

The same results were found in the Finnfjord sample as in the two Elkem samples. The formation of the FeSi/Si-particle seen in Figure 4.21 indicates precipitation of Si from a Fe_xSi_y-melt.

4.2.3. XRD of Si-droplets

In most experiments, droplets of Si formed underneath the sample during experiments. Sample E#41 showed especially large droplets, and as this sample was measured under both Ar and N_2-atmopsheres both droplets were investigated to see if any Si_xN_y was formed. Photos of the sample with droplet from Ar-experiment and the droplet from the N_2-

experiment can be found in Figure 4.24 and Figure 4.25. Both were examined in the XRD to determine the composition.

Figure 4.24: Sample E#41 after the first experiment (Ar atmosphere)

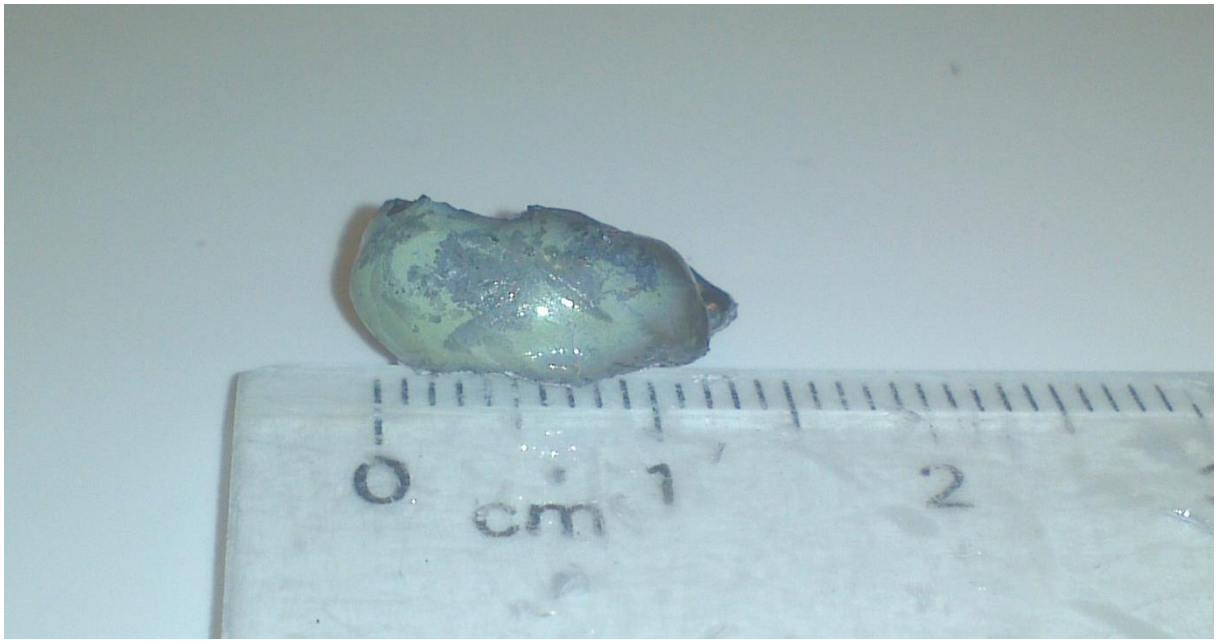

Figure 4.25: Droplet formed beneath sample during the second experiment (N_2 atmosphere)

XRD-spectra for the two droplets are seen in Figure 4.26 and Figure 4.27.

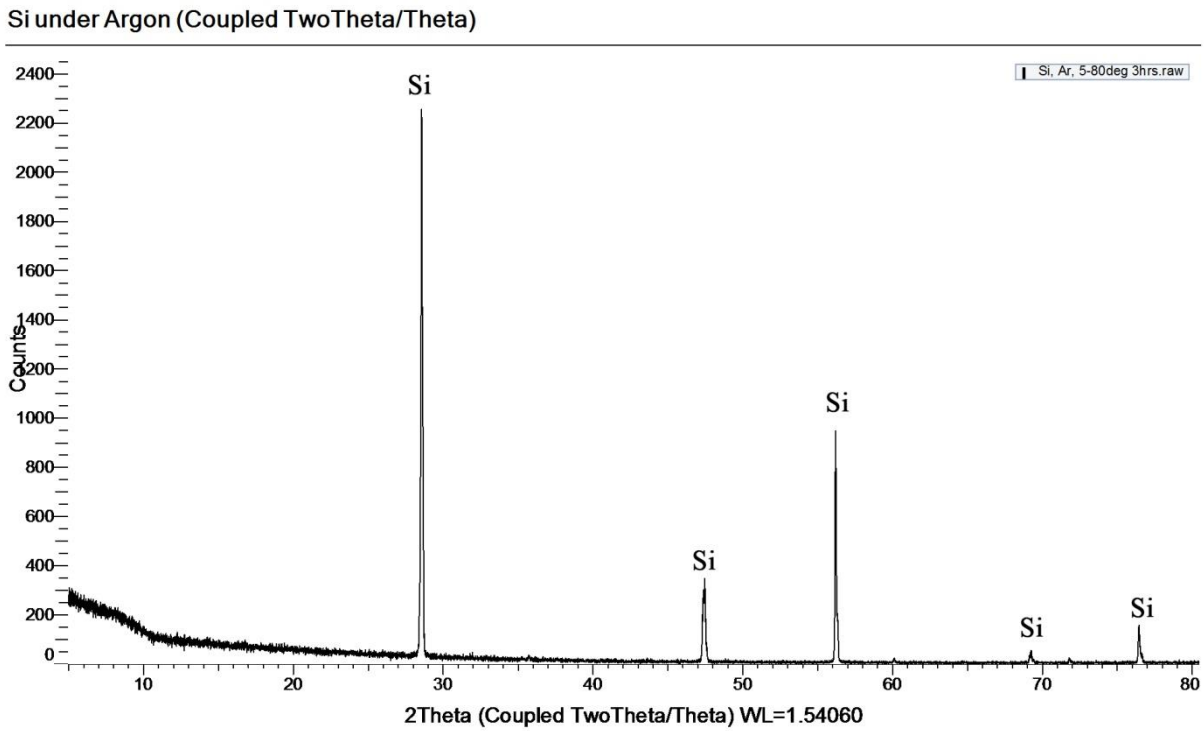

Figure 4.26: XRD-spectrum for the droplet formed during experiments with Ar-atmosphere

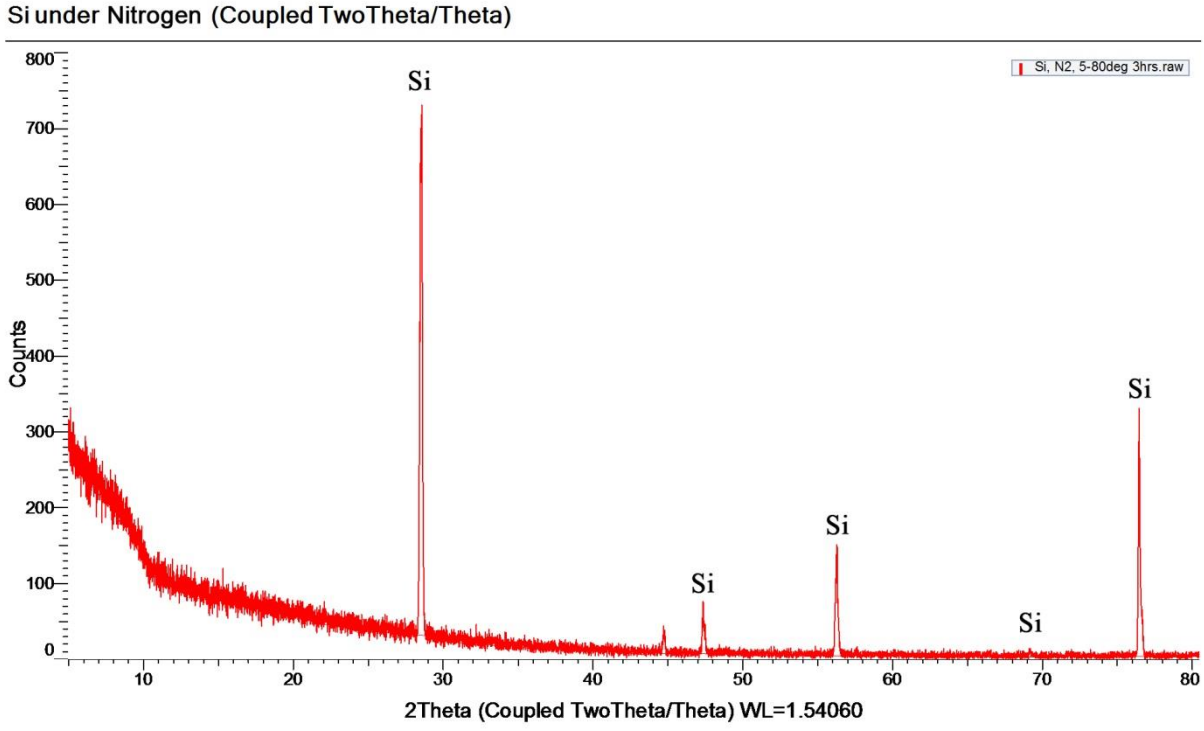

Figure 4.27: XRD-spectrum spectrum for the droplet formed during experiments with N_2 -atmosphere

Both droplets show the same peaks, with the exception of a minor peak in the N_2-atmosphere sample. No decisive phase was found for this peak.

CHAPTER 5. DISCUSSION

5.1. Resistivity of industrial SiC-crusts

The resistivity of industrial SiC-crust samples compared to the other materials of the furnace is found in Figure 5.1 while Figure 5.2 shows the SiC-crust samples in a logarithmic scale.

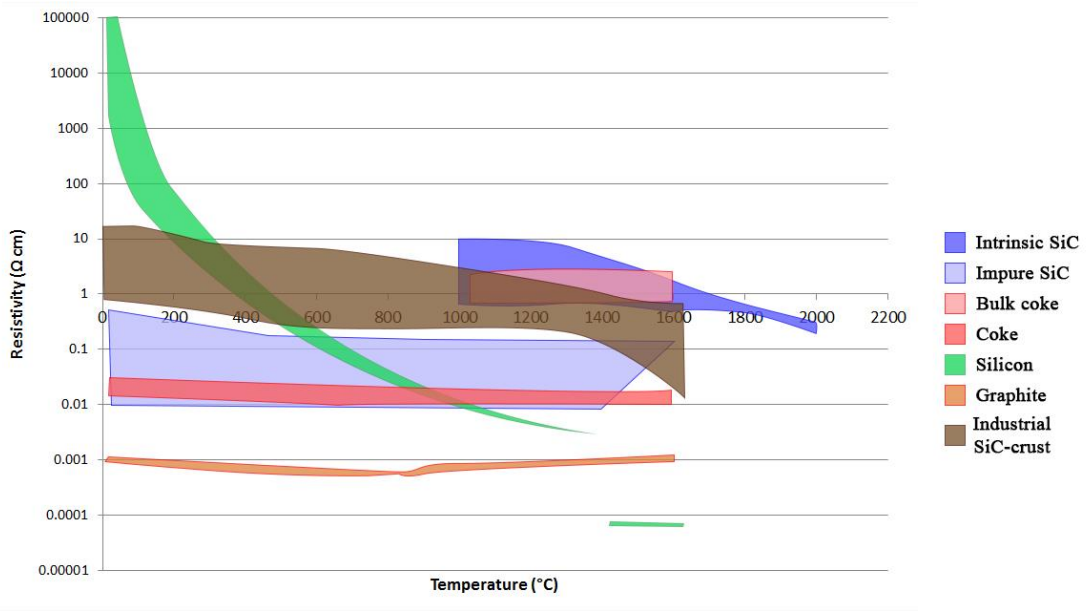

Figure 5.1: Resistivity of materials found in a silicon-alloy furnace

The first thing to notice is the width of the resistivity range at all temperatures, even at high temperatures. This width is not larger than the literature values found for impure SiC, but the decrease is not comparable with the literature where a much smaller decrease with temperature is seen. The explanation for this could be porosity of the crust samples which is not investigated in the literature, where all samples are insignificantly porous. A support for this is the much larger decrease in resistivity with temperature in the Finnfjord-samples, which also have a significantly larger porosity than the Elkem-samples seen Figure 5.3 which shows the difference in resistivity ($\Delta\rho$) at high and low temperature as a function of porosity. The effect of larger decrease is also seen in between the two Finnfjord-samples, with F#33 having a smaller porosity and decrease than F#97. An increase in porosity seems to indicate higher room-temperature resistivity as well. This effect seems to diminish with temperature, suggesting that the continuous SiC conducts the electricity around the pores efficiently. As

experiments are performed with DC current, no surface current effects are expected along the pores.

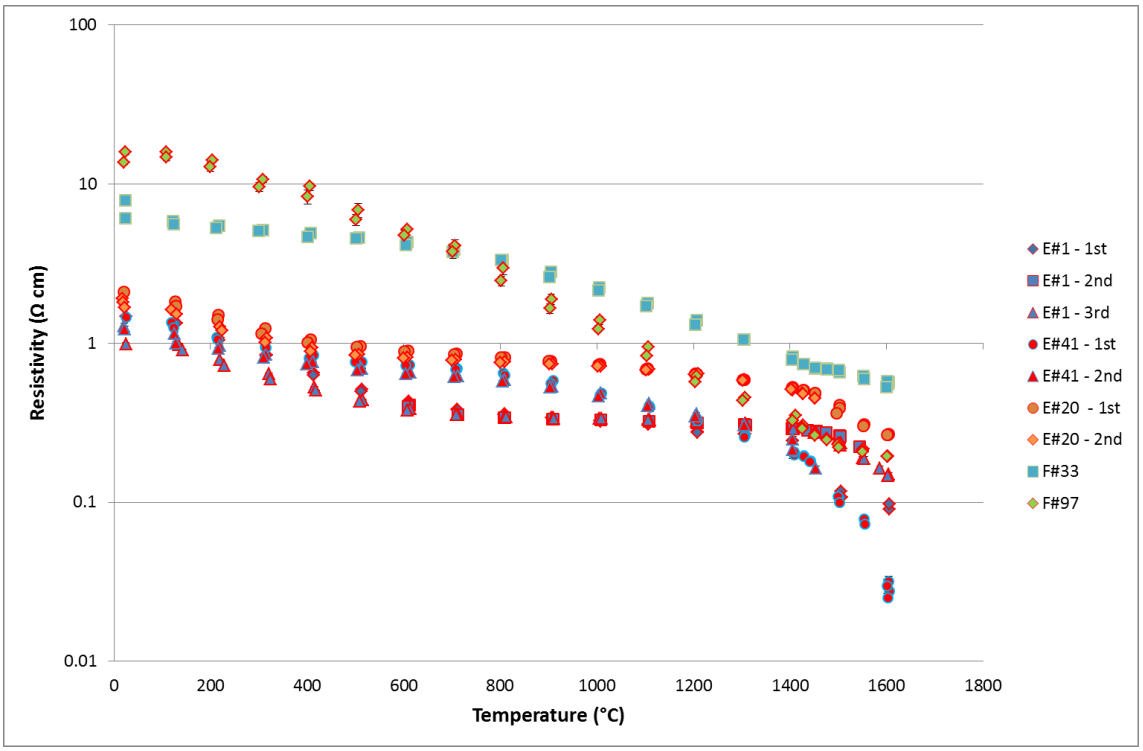

Figure 5.2: The resistivity of all industrial-SiC-samples as a function of temperature

The resistivity of the industrial SiC-crust is also lower than the intrinsic values found in the literature; this corresponds with the conclusion that the SiC is an extrinsic semiconductor made by Krokstad (2013). The other samples are however not following the same extrinsic resistivity-temperature relationship as was found in E#1 by Krokstad, and has a flatter more linear decrease which can be seen especially in F#33 in Figure 4.1.

All samples except E#1 follow a relatively linear relationship between amount of FeSi + Si and high temperature resistivity where an increased amount of FeSi + Si corresponds to a decreased resistivity as seen in Figure 5.4. It is reasonable to assume the FeSi and Si is liquid above ~1400°C from the Fe-Si phase diagram (Figure 5.5), which would lead to pools of molten metal inside the sample. If these pools wet the SiC to an acceptable degree they could

create highly conductive paths for the electric current, as seen in Figure 5.6, reducing the resistivity of the sample.

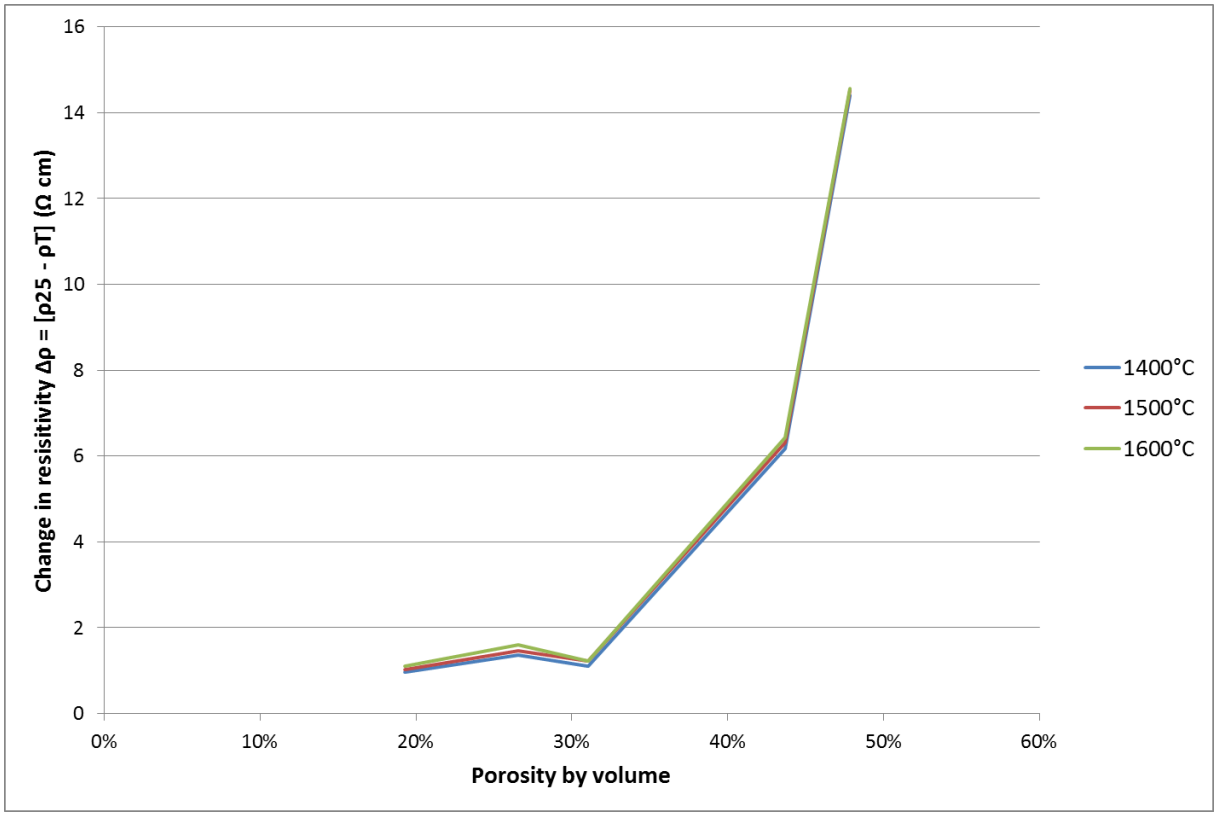

Figure 5.3: Change in resistivity as a function of volume-percent FeSi + Si based on all samples.

Even though droplets formed beneath most samples, no significant decrease in Si or FeSi-content was seen with the samples before and after heating. It is therefore expected that hypothesis 3 of the project work (Krokstad, 2013), where silicon or FeSi is pooling up towards the bottom or beneath the sample forming continuous, highly conductive layers, is invalid. Hypothesis 1, with conductive pools evenly spread throughout the sample is likely. See Figure 5.6. This pooling of metal, and its sudden drop in resistivity as it melts, is the main reason no attempt at finding the material constants for intrinsic resistivity.

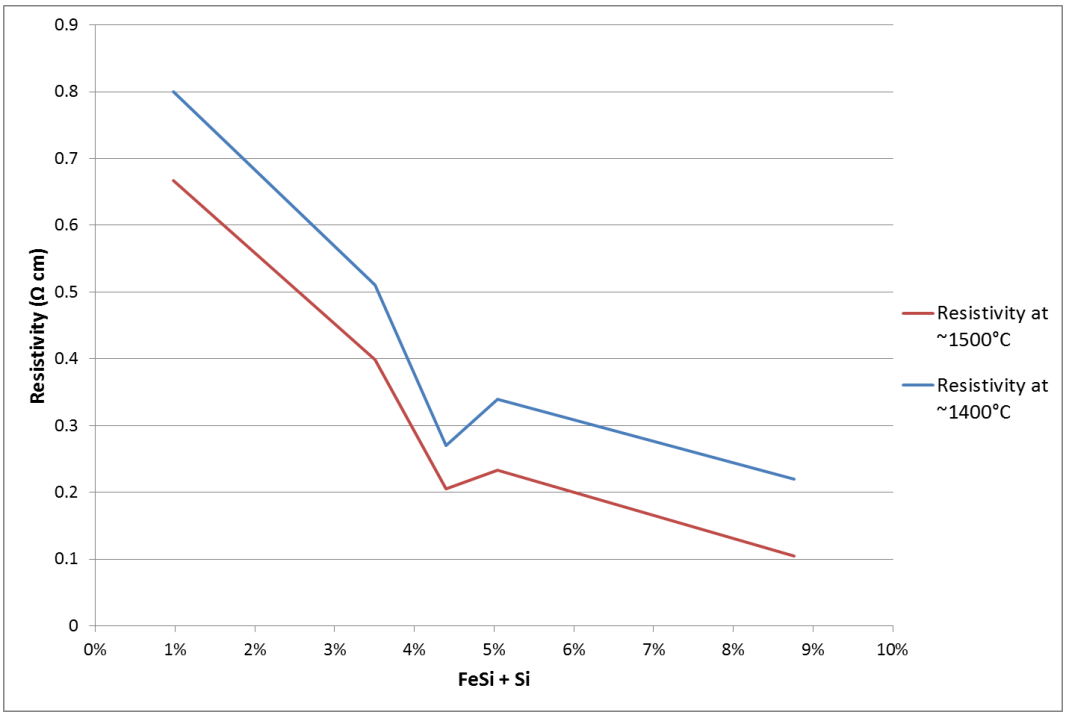

Figure 5.4: Resistivity at high temperature as a function of volume-percent of FeSi+Si

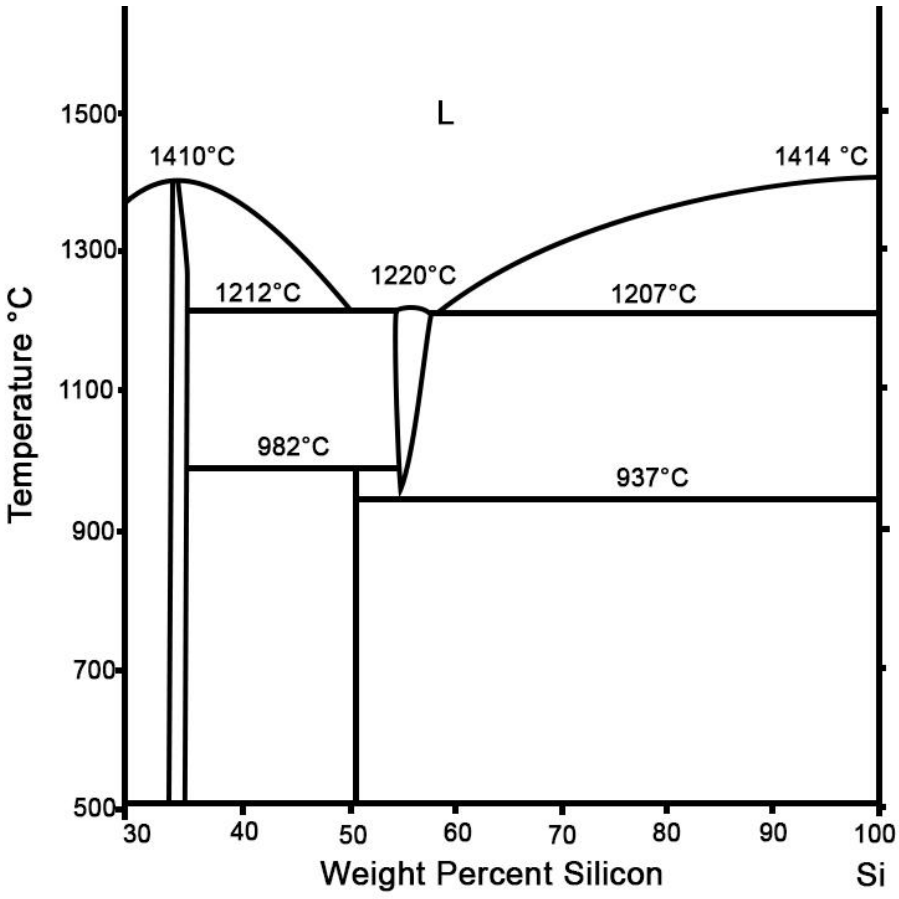

Figure 5.5: The Fe-Si phase diagram (from Schei et al. (1998, pp. 301))

Another effect seen in this work is the reduction of low-temperature resistivity with subsequent heating. Above 500ºC there was no significant difference between the resistivity for the same sample, but subsequent heating. As all wires and paste was reapplied between the experiments, the most likely reason for the low temperature differences is that as the setup was tested to ensure full contact. This testing lead to an ohmic heating of the sample, and its temperature is higher than that of the crucible suggested by the thermocouple. This could also be the reason for the different shape of the curves at lower temperatures, as the heating from the measurement could have given the sample a higher temperature than indicated.

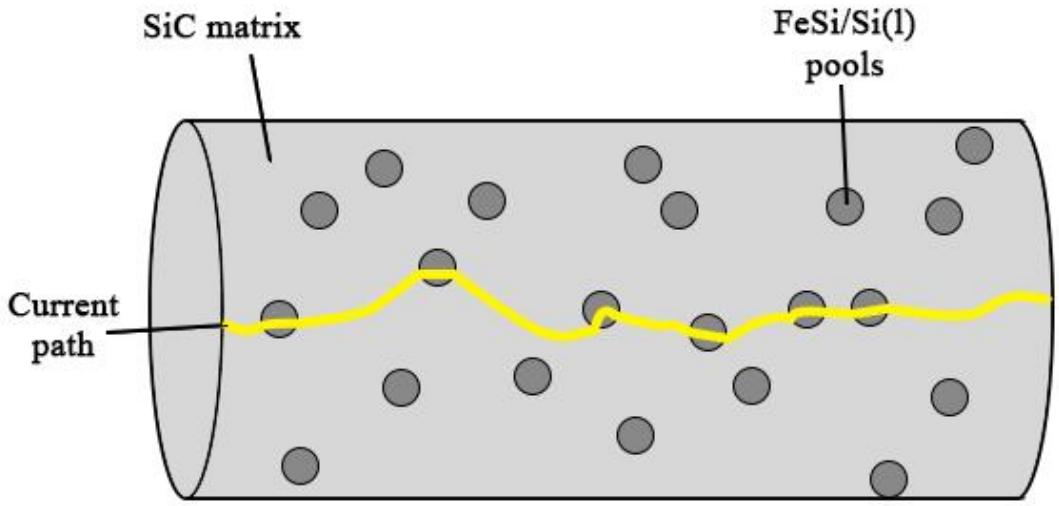

Figure 5.6: Possible current path via pools of FeSi/Si (Krokstad, 2013)

While the temperature of the crust in the furnace is thought to be higher than 1600°C, equipment did not allow for measurements above this temperature. As best seen in Figure 4.3, the resistivity does not seem to have reached a steady state and would probably decrease further with temperature giving even lower values at industrial temperatures.

It is also important to notice that the measurement of the resistivity of the solid material itself was not the goal for this work, but rather the bulk-resistivity of the material as a whole.

5.2. Compositional differences in the SiC-crust

As seen, a large difference in composition of the industrial SiC-crust can be found both on a short and a long range. The short-range order is, in this work, used on the samples internally and would refer to lengths of 2-3 cm. Long range order is the spacing between the samples, which is unfortunately unknown for the Elkem samples. F#33 is from the centre column while F#97 was located towards the lining in a zone of brown condensate according to Tranell et al. A first glance through the Z-contrast images (Figure 4.5 through Figure 4.9) gives a few conclusions discussed in the following:

The different samples show quite different structures, some with SiC grains of various size (70 µm to 900 µm) and others with a continuous SiC phase. Long range difference is of no surprise, as the furnace is not perfectly symmetrically charged, stoked and tapped.

Two major characteristics appear when considering the composition of the samples, first is the content of FeSi/Si. The Finnfjord-furnace was using iron ore pellets as a source of iron, but by assuming all iron is found as a metal it should be of no surprise to find most of the metal in the form of FeSi. Tranell et al. (2010) found this FeSi to be in the ratio $Fe_{45}Si_{55}$ on a weight basis. They argue this comes from precipitation from the liquid phase, which is only possible if the liquid has a composition very close to the solid composition as almost no pure Si was found in samples F#33 and F#97.

The condensation of SiO (g) through reaction 2-8 (2 SiO (g) = SiO_2 (s,l) + Si (l)) is less likely, as Tranell et al. also states, due to the lack of oxide in the vicinity of the FeSi or Si. It is likely this happens further up in the furnace where the temperatures are lower and a condensate consisting of SiO_2 and Si is found (Vangskåsen, 2012). This does, however, create an interesting question about the temperature in the crust as reaction 2-8 is thermodynamically favourable at temperatures below 1811°C. Tranell et al. mentions that the furnace was operated above its designed power, and the inside temperature could be higher relative to standard operation. If the crust is at such high temperatures, it is possible for the lower parts of it to be a major source of Si-production through reaction 2-4 [SiC (s) + SiO (g) = 2 Si (l) + CO (g)].

Table 5.1: Major characteristics found in the Z-contrast images of the samples
More images can be found in APPENDIX B

Sample	Characteristics
E#1	• Very continous SiC – Traces of crystals/grains surrounded by or in the Si • Size range of 140 µm to 900 µm • Some slag present close to Si • All FeSi present close to or on Si
E#20	• Continous SiC – Traces of original carbon particles in the Si and pores • Size range of 160 µm to 800 µm • Some slag present close to Si • All FeSi present close to or on Si
E#41	• Obvious traces of crystals/grains close to pores and in the Si – Size range of 70 µm to 600 µm • Large areas of Si (big pools) • Some slag present close to the Si • All FeSi present close to or on Si
F#33	• Obvious crystals/grains – Not as continuous – Size range of 70 µm to 900 µm • Very small amounts of slag – Not present close to FeSi • Small and evenly distributed FeSi • All Si present close to FeSi
F#97	• Mainly continuous SiC – Traces of shapes similar to crystals/grains, which seems sintered • Size range of 140 µm to 440 µm • Slag present close to pores, not the FeSi – Low amounts of slag considering the sample supposedly comes from the brown condensate layer

Samples from the Elkem-SiC only had trace amounts of iron, and most of the metal was found as pure Si. Tangstad et al. (2014) does not explain the origin, but slag/oxide was found several places close to the Si and reaction 2-8 seems likely. The amount of each is however not equal as suggested by the reaction as a lot more Si is seen compared to SiO_2. It is also possible that the SiO_2 reacts with SiC through reaction 2-2 [2 SiO_2 (s,l) + SiC (s) = 3 SiO (g) + CO (g)] if the temperature is high enough, but this reaction should have left pores in close vicinity of the Si which is not seen regularly enough for it to be definite. The lack of pores could be explained by the expansion of Si as it solidifies.

The second major characteristic of the samples is the seemingly continuous SiC in E#1, E#20 and, to a smaller degree, F#97 compared to the crystal/grain-based SiC matrix of E#41 and F#33. The structure of the samples can be seen in the Z-contrast images of Figure 4.5 through Figure 4.9 and in APPENDIX B.

Tranell et al. does not discuss how the SiC formed, but Tangstad et al. suggest a mechanism of deposition from gaseous SiC. It is thought that the carbide is formed from silicon species reacting with solid carbon particles, but as neither Tranell et al. nor Tangstad et al. found any free, solid carbon in their investigation of the condensate layers it is unlikely solid carbon particles can form SiC. The particles seen in the Z-contrast images are also too small to be formed from coal particles, up to ten times smaller than the recommended size of 1.5 mm (Schei et al., 1998).

Both Vangskåsen (2012) and Myrhaug (2003) investigated transformed carbon particles from pilot scale furnace experiments. While the SiC found by Myrhaug at the bottom of the furnace, in close vicinity of coke and charcoal seems visually similar to the structure of more continuous SiC found in this work (see Figure 5.7 (right) and Figure 5.8 (left)). The same applies to anthracite in contact with molten silicon (Figure 5.8, right). Samples from further up in their furnaces where, obvious reactions between carbon and SiO is seen, show a different structure to the SiC found in this work, see Figure 5.7 (left). While no SiC-crust was found in the pilot experiment of Vangskåsen, samples from the top to the bottom of the furnace were taken and can be seen in Figure 5.9 through Figure 5.11. The SiC-structure seems visibly similar at towards the bottom of the furnace, but a lot more Si is observable due to reactions between SiO (g) and SiC. The lack of a crust in Vangskåsen's experiments could indicate that the gas-specie-mechanism of Tangstad et al. is correct, as it requires an electric arc to create to temperatures required for the gas-species to develop.

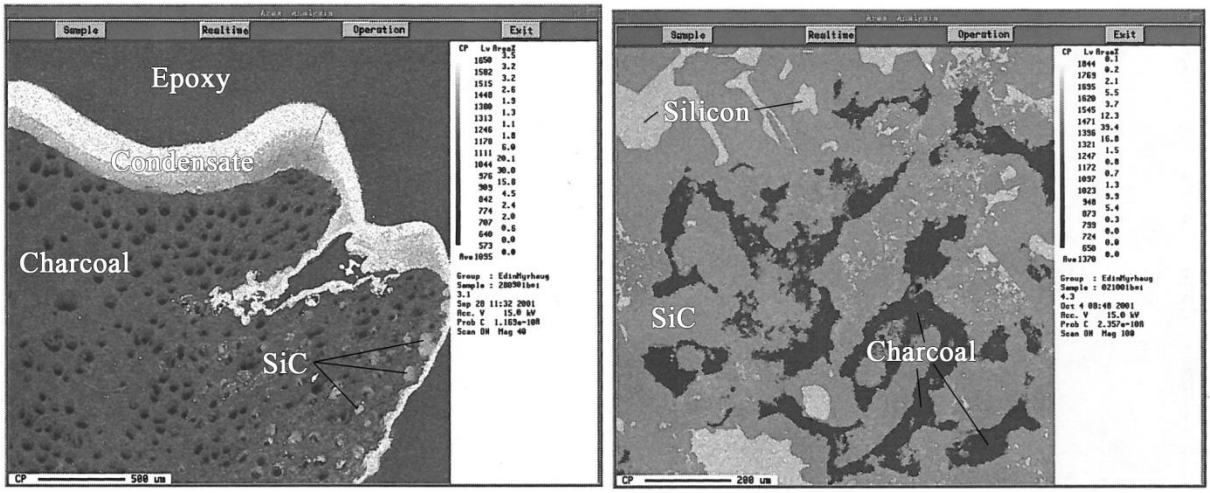

Figure 5.7: Charcoal from top of charge (left) and partially converted charcoal on top of SiC-crust (right) (Myrhaug, 2003)

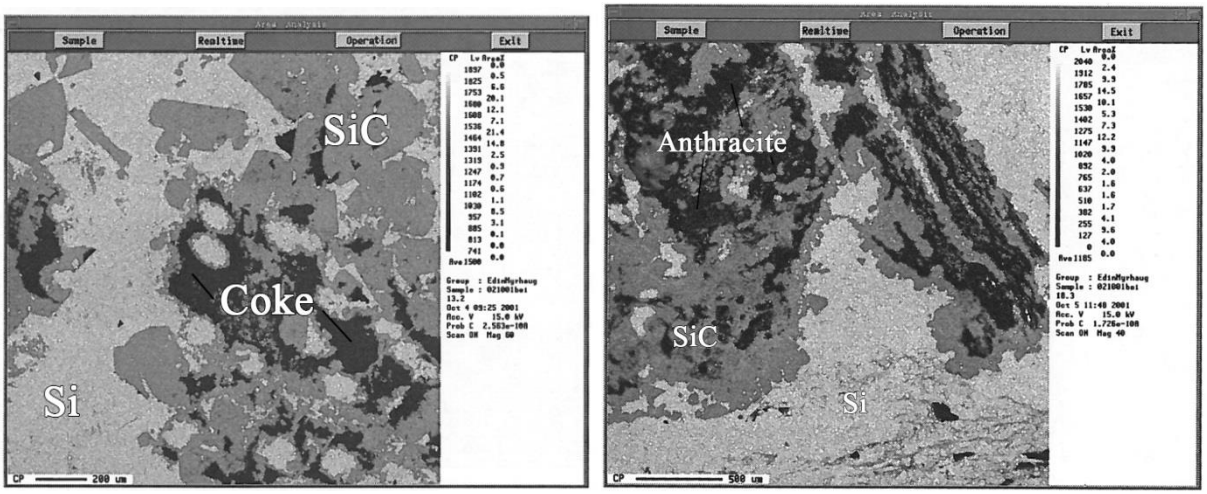

Figure 5.8: Unreacted coke from the bottom of the furnace (left) and anthracite in contact with molten silicon reacting to SiC (right) (Myrhaug, 2003)

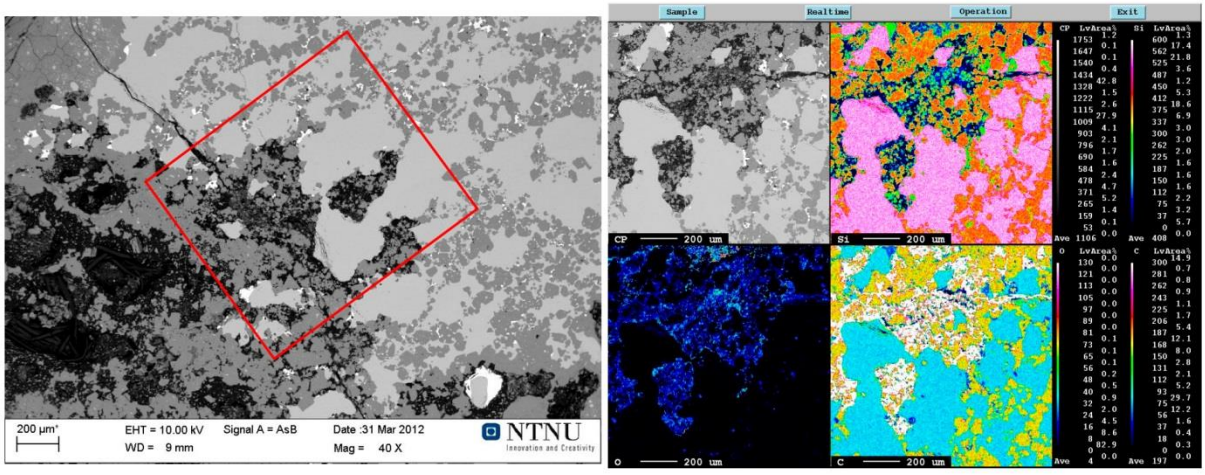

Figure 5.9: Partially converted SiC from Vangskåsen (2012) (left). EPMA of red region (left)

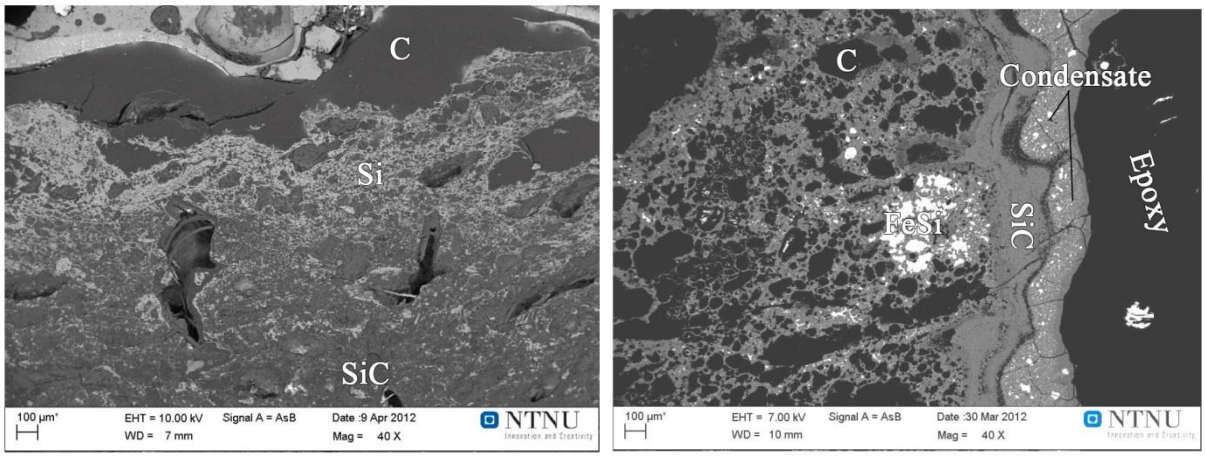

Figure 5.10: Carbon reacting to SiC, and further on to Si, with SiO-gas (left: top of furnace, right: top of condensate layer) (Vangskåsen, 2012)

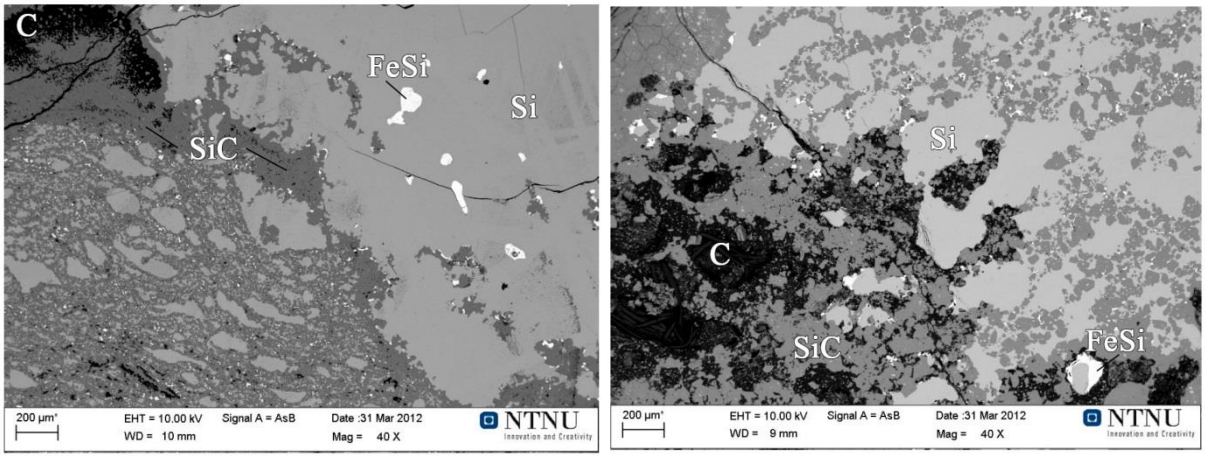

Figure 5.11: Carbon reacting to SiC, and further on to Si, with SiO-gas (left: middle of condensate layer, right: bottom of condensate layer towards the metal bath) (Vangskåsen, 2012)

The needle-shaped grains of SiC found especially in sample F#33 look more like the precipitated SiC from silicon melts found by both Myrhaug and Vangskåsen (Figure 5.12). But it seems unlikely that the formation of crust is from precipitation from molten Si. It could, however, come from the reaction between CO (g) and Si (l) (reverse reaction 2-4). This would explain the shape of the porosity of the SiC, and perhaps also the dendrite-like shape as the reaction would happen easier once a SiC-nucleus has already formed.

By calculating the equilibrium composition with decreasing temperature of a mixture of Si(l):SiO(g):CO(g) of 0.1:1:1 by atoms, Figure 5.15, SiC seems to emerge already at 1975°C showing this as a possible crust-forming mechanism.

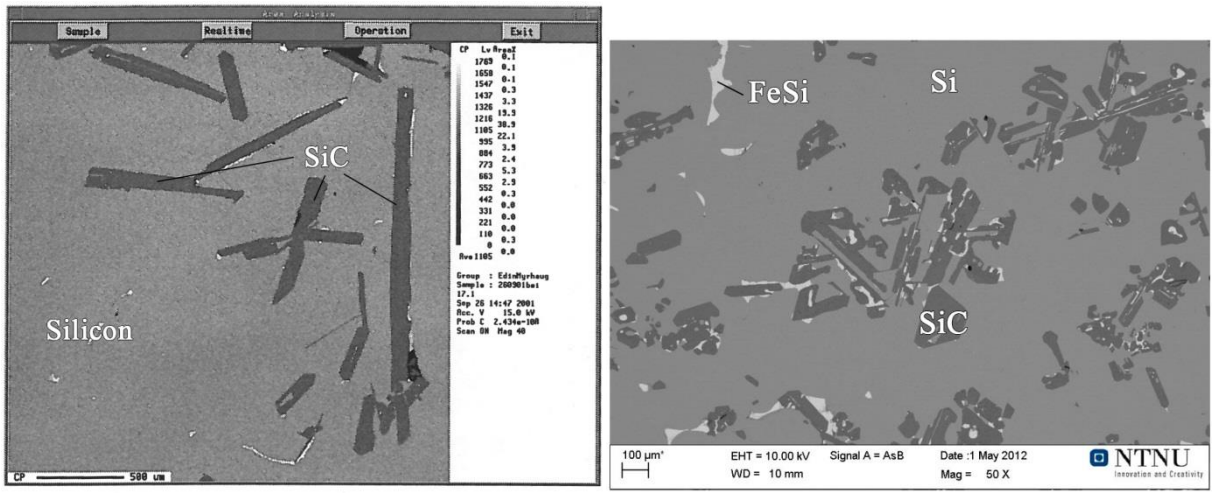

Figure 5.12: SiC precipitated from the metal baths of Myrhaug (2003, left) and Vangskåsen (2012, right)

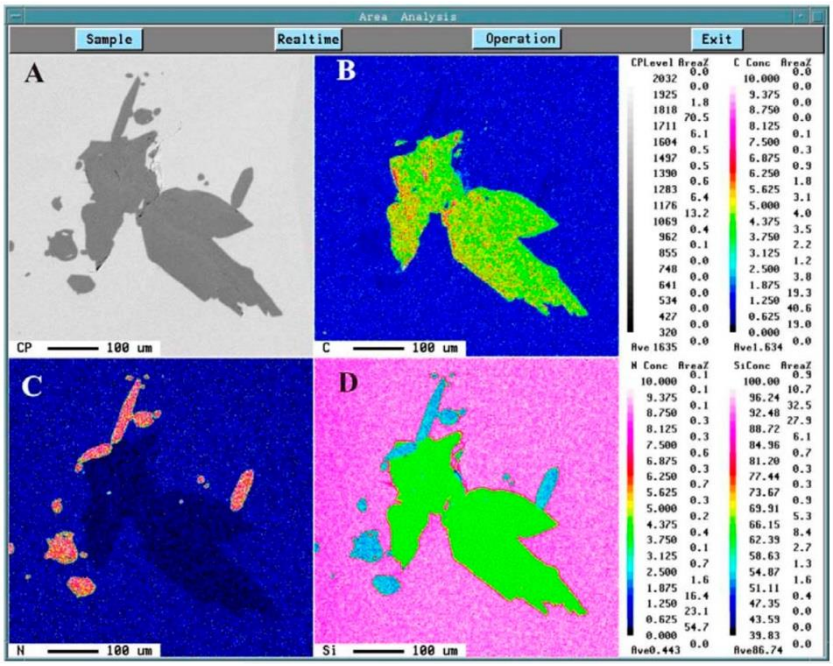

Figure 5.13: SiC-particles precipitated from liquid silicon (Ciftja, 2009)

The gaseous SiC thought by Tangstad et al. to have deposited into the carbide layer comes from the plasma arc, which holds several thousand degrees. An equilibrium calculation in HSC, ignoring the plasma species for practicality, gives Figure 5.14. An assumption of SiO (g) : CO (g) = 1:1 is made as cavity gas composition based on Saevarsdottir et al. (2001).

One can see that several gas species will develop in/close to the arc where the temperature is high enough, even Si_xC_y (g)-species. While this could mean Tangstad et al. could be correct in their speculations that the carbide phase is formed through deposition, it is difficult to conclude as the amount of Si_xC_y-gases in equilibrium should be very low. However, if the arc continuously is striking against the carbide layer, it could still be possible for the formation of enough gases close to the surface to create a growing crust.

Another argument against the formation of SiC through deposition is the reaction between the Si_xC_y (g) and SiO (g) through reactions 5-1 through 5-3, for which the standard Gibbs energy can be seen in Figure 5.16. At the relevant temperatures, all reactions are favourable with reaction 5-1 being favourable to temperatures well below the suspected crust-temperature.

$$SiC(g) + SiO(g) = 2Si(g) + CO(g) \qquad 5\text{-}1$$

$$Si_2C(g) + SiO(g) = 3Si(g) + CO(g) \qquad 5\text{-}2$$

$$SiC_2(g) + 2SiO(g) = 3Si(g) + 2CO(g) \qquad 5\text{-}3$$

An argument left undiscussed is the possibility that the SiC-crust is formed as a part of the green condensate, but as the SiO_2 and Si reacts and/or is drained away one is left with the SiC. In the Finnfjord-furnaces, sample F#33 was taken closer to the arc chamber than sample F#97 and would have felt a higher temperature and thus a lower viscosity of the metal. This could explain the lower content of FeSi, as it would have trickled out of the SiC and into the cavity. This argument is hard to make with the Elkem-samples, as their position is unknown. This crust growth mechanism is only possible if the crust is grown at the condensate layer and pushes the existing crust outwards. If the crust, however, grows on the surface of the cavity it is not feasible.

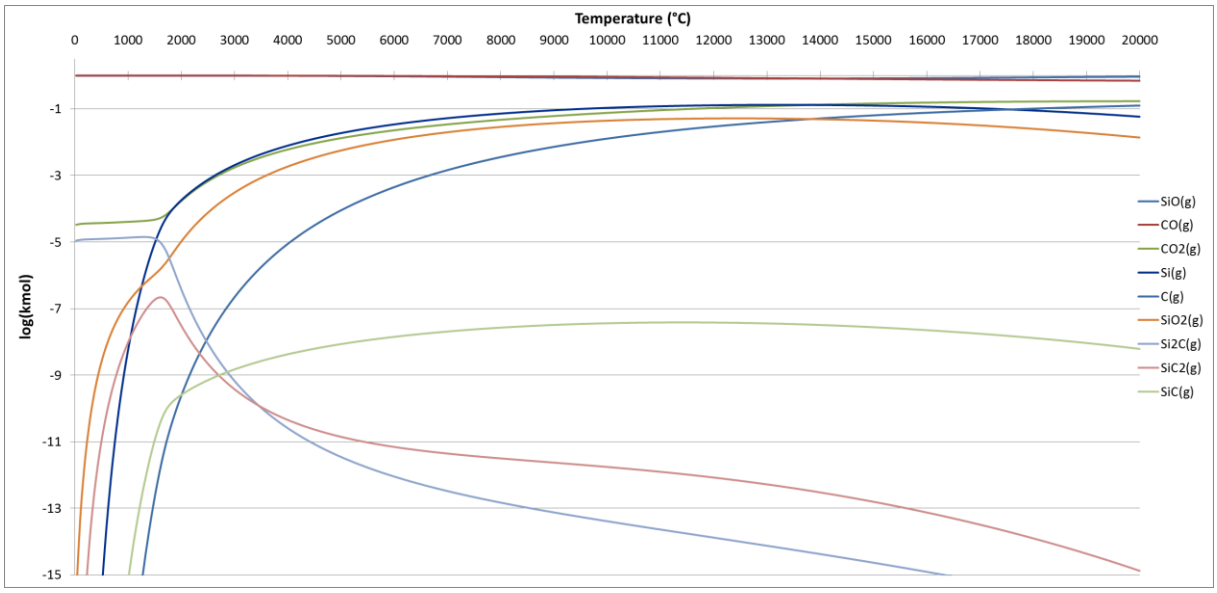

Figure 5.14: HSC equilibrium composition of gases from the plasma with a composition of SiO:CO = 1:1

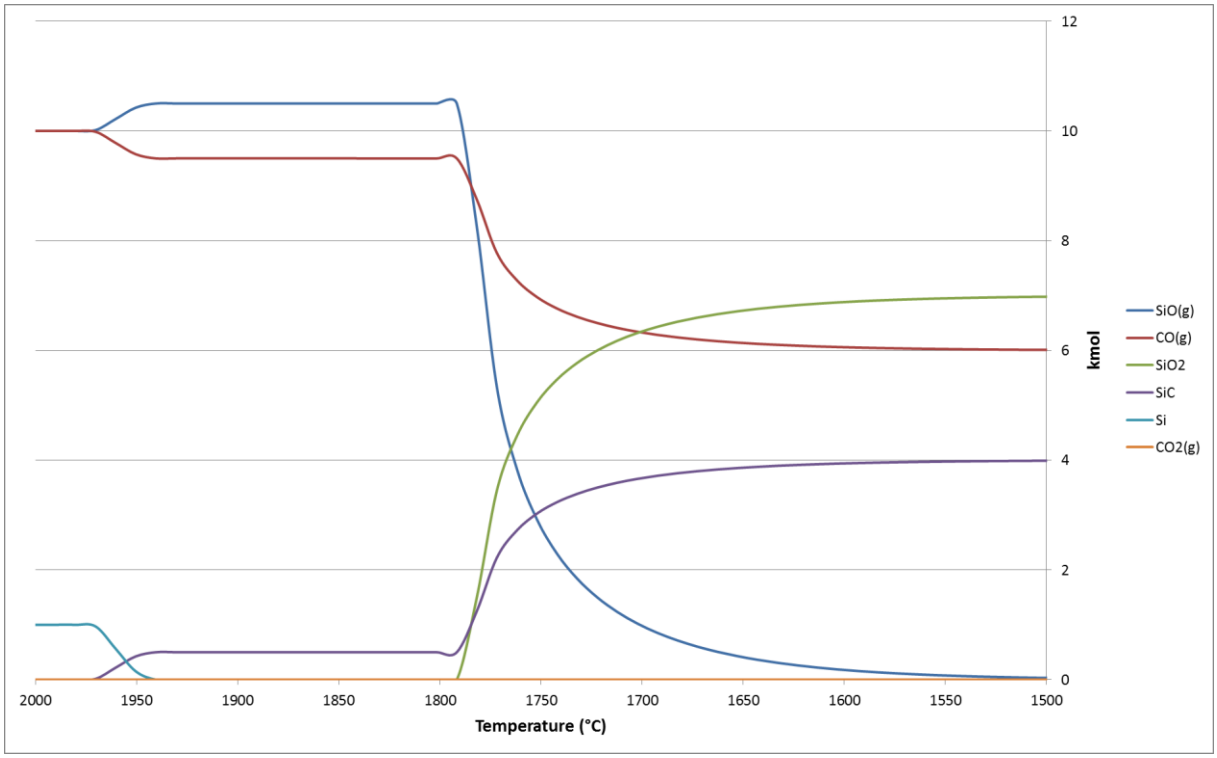

Figure 5.15: Equilibrium composition of a mixture of SiO(g), CO(g) and Si(l) in the ration 1:1:0.1

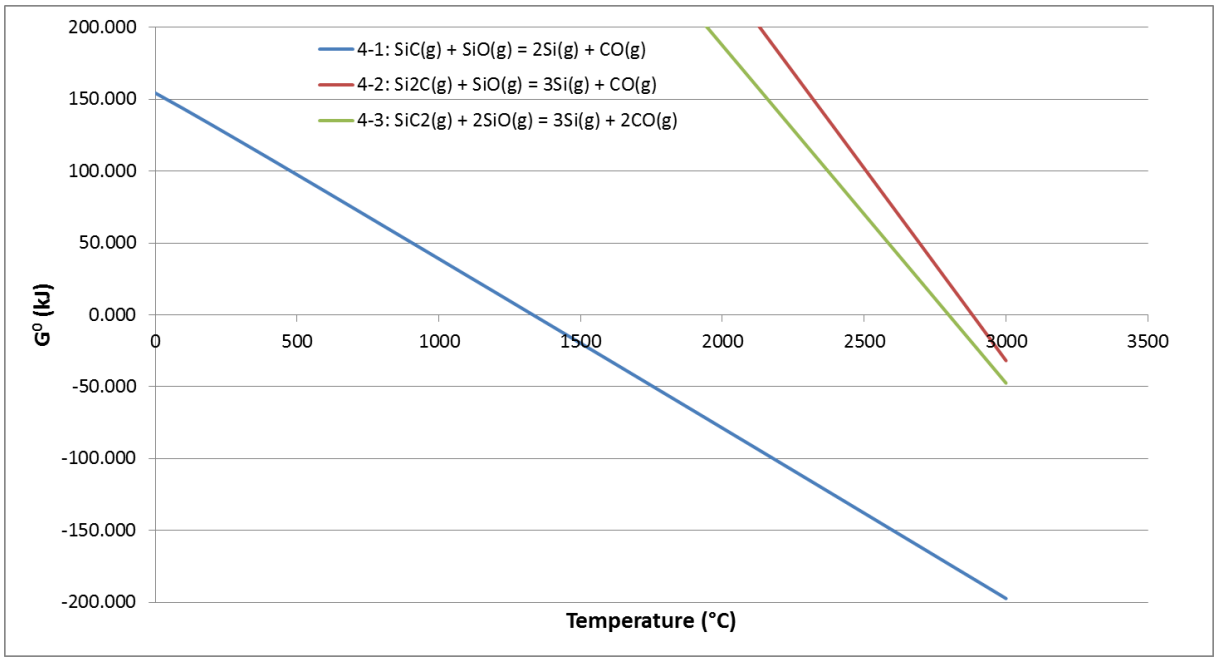

Figure 5.16: Standard Gibbs energy for reaction 5-1 through 5-3

5.3. Current path distribution

Valderhaug (1992) assumes an insignificant amount of current, 1% based on the findings of Schäfer (1984)and Stewart (1980), flows through the charge between the electrodes. This is based on the melting of any metallic Si conducting electricity through the charge from ohmic heating, leading to a break of contact. If the centre-SiC-column is the main conductor of electrode-to-electrode current it could possibly be much higher than 1% of the total current. No comment on how much of the arcing happens towards the crater walls instead of the metal pool is made by Valderhaug.

The modelling by Saevarsdottir and Bakken (2010) showed that up to 2/3 of the current can bypass the arc if only one arc is present, they also stated that several arcs is probable and will reduce this amount.

Saeversdottir et al. (2001) concludes that the arcs can be no longer than 10 cm, which, with the movement of the electrode seen in chapter 2.4, suggests a significant amount of the arcs will connect with the SiC-crust instead of the metal pool. This could lead to higher temperatures of the crust from ohmic heating than previously assumed, explaining the lack of oxides close to the Si-formations as temperatures could locally become high enough for reaction 2-2 to occur.

The furnace operates with an AC-system, and as such surface currents and impedance would affect the electrical properties of the crust significantly. These are not accounted for in this work.

CHAPTER 6. CONCLUSION

SiC crust excavated from industrial FeSi and Si furnaces has been studied regarding electrical resistivities and structure. The resistivities have been measured up to temperatures of 1600 °C by a 4 point measuring method.

The industrial SiC-crust has, at temperatures around 1600°C, a resistivity in the range of 0.1-1 Ω cm. It is therefore likely that a significant amount of the arcs from the electrode will strike against the crust. The SiC crust has a higher resistivity than liquid Si (10^{-4} Ω cm), in the range of commercial SiC materials (10^{-2} – 10^{0} Ω cm) at high temperature, but lower than a cokebed (1-5 Ω cm) used in other metal producing furnaces.

Samples showed a large difference in composition, but this does not seem to affect the resistivity at high temperatures to a large degree. Increased content of metal, liquid at the respective temperature, seems to indicate a lower high-temperature resistivity. More samples should be measured to find a more reliable correlation.

In the Elkem-samples, a fairly similar structure appears in all samples. The continuity of the SiC seems to be the major difference, and while the composition varied between samples the variance in each sample in and of itself could account for these variations. The position, in the crust, of these samples is unfortunately unknown, so a discussion regarding their relative position and composition is impossible. Sample E#1 and E#20 show little traces of grains while E#41 shows a clear indication of grain/dendrite-formation structure.

The Finnfjord samples can be separated from the Elkem-samples with two main differences. First is the content of FeSi instead of Si, which comes from the fact that Finnfjord produced FeSi and Elkem MG-Si. Second is the porosity, where the Finnfjord-samples showed a higher amount of pores. The structure of the two samples is different to each other, with sample F#33 showing a much more granular structure similar to that of SiC precipitated from molten silicon solidifying as well as a much lower content of FeSi. Sample F#97 had a structure more resembling that of E#41, with clear grains but more continuous SiC than F#33. Composition of the samples is in the ranges of about 50-75 vol% SiC, 20-50 vol% pores and 0-10 vol% Si or FeSi..

It is difficult to decide a SiC-forming mechanism from the results of this work, but several ideas have been suggested with more work needed to conclude:

1. Formation of SiC from carbon seems unlikely as no free carbon is found in the condensate layer above the SiC-crust. The structures found from reactions with carbon particles and SiO (g) also seem to form a different structure.
2. SiC could be formed from Si (l) trickling down from the brown condensate reacting with CO (g)
3. The arcs could facilitate the formation of Si_xC_y –gases depositing as the SiC-crust
4. The crust could grow by losing the SiO_2 and Si from the condensates and being pushed down by the weight of new raw materials.
5. Precipitation of SiC from the liquid Si phase during temperature cycles.

The electrode-to-electrode current is thought to be around 1%, but could be much higher by going through the column in the centre of the furnace consisting mainly of conductive SiC instead of the thought path via silicon engulfing charge particles. This is however purely speculation based on material properties.

REFERENCES

ASKELAND, D. R. & PHULÉ, P. P. 2003. The science and engineering of materials.

BLUDAU, W., ONTON, A. & HEINKE, W. 1974. Temperature dependence of the band gap of silicon. *Journal of Applied Physics,* 45**,** 1846-1848.

CIFTJA, A. 2009. Solar silicon refining; Inclusions, settling, filtration, wetting.

EIDEM, P. A. 2008. Electrical resistivity of coke beds. *Doctoral Theses at NTNU,* 279.

EISENHÜTTENLEUTE, V. D. 1995. *Slag Atlas,* Verlag Stahleisen GmbH.

FETTERLEY, G. 1957. Electrical Conduction in Silicon Carbide. *Journal of The Electrochemical Society,* 104**,** 322-327.

GASIK, M. 2013. *Handbook of Ferroalloys: Theory and Technology*, Butterworth-Heinemann.

GNESIN, G., SHIPILOVA, L. & KAS' YANENKO, A. 1983. Electrical conductivity of self-bonded silicon carbide doped with boron. *Powder Metallurgy and Metal Ceramics,* 22**,** 1022-1025.

GNESIN, G., ZAKHARENKOV, V. & SHIPILOVA, L. 1978. Volume electrical resistivity of silicon carbide heating elements. *Powder Metallurgy and Metal Ceramics,* 17**,** 72-76.

HOFFMANN, A., REUSCHEL, K. & RUPPRECHT, H. 1959. Measurement of the hall effect and conductivity of super-pure silicon. *Journal of Physics and Chemistry of Solids,* 11**,** 284-287.

KOSOLAPOVA, T. Y. 1968. Carbides. *Metallurgiya, Moscow***,** 299.

KOUKOUZAS, N., HÄMÄLÄINEN, J., PAPANIKOLAOU, D., TOURUNEN, A. & JÄNTTI, T. 2007. Mineralogical and elemental composition of fly ash from pilot scale fluidised bed combustion of lignite, bituminous coal, wood chips and their blends. *Fuel,* 86**,** 2186-2193.

KROKSTAD, M. A. 2013. *Measuring electrical resistivity of SiC found in a MG-Si furnace.* NTNU.

LAW, J. & FRANCOIS, E. 1956. Adsorption of Gases on a Silicon Surface. *The Journal of Physical Chemistry,* 60**,** 353-358.

LI, Y. & CHING, W. 1985. Band structures of all polycrystalline forms of silicon dioxide. *Physical Review B,* 31**,** 2172.

LINDSTAD, T., GAAL, S., HANSEN, S. & PRYTZ, S. 2007. Improved SINTEF SiO-reactivity Test. *INFACON XI, New Dehli*.

MYRHAUG, E. H. 2003. Non-fossil reduction materials in the silicon process–properties and behaviour. *PhD avhandling NTNU,* 67.

OLANDERS, B. & STEENARI, B.-M. 1995. Characterization of ashes from wood and straw. *Biomass and Bioenergy,* 8**,** 105-115.

PELISSIER, K., CHARTIER, T. & LAURENT, J. 1998. Silicon carbide heating elements. *Ceramics international,* 24**,** 371-377.

RACETTE, J. 1957. Intrinsic Electrical Conductivity in Silicon Carbide. *Physical Review,* 107**,** 1542-1544.

RYU, C., YANG, Y. B., KHOR, A., YATES, N. E., SHARIFI, V. N. & SWITHENBANK, J. 2006. Effect of fuel properties on biomass combustion: Part I. Experiments—fuel type, equivalence ratio and particle size. *Fuel,* 85**,** 1039-1046.

SAEVARSDOTTIR, G. & BAKKEN, J. 2010. CURRENT DISTRIBUTION IN SUBMERGED ARC FURNACES FOR SILICON METAL/FERROSILICON PRODUCTION.

SAEVARSDOTTIR, G., BAKKEN, J. A., SEVASTYANENKO, V. & GU, L. 2001. High-power AC arcs in metallurgical furnaces. *High Temperature Material Processes (An International Quarterly of High-Technology Plasma Processes),* 5.

SASAKI, H., IKARI, A., TERASHIMA, K. & KIMURA, S. 1995. Temperature dependence of the electrical resistivity of molten silicon. *Japanese journal of applied physics,* 34**,** 3426-3431.

SCHEI, A., TUSET, J. K. & TVEIT, H. 1998. *Production of high silicon alloys*, Tapir Trondheim, Norway.

SHUR, M., RUMYANTSEV, S. L. & LEVINSHTEĬN, M. E. 2007. *SiC materials and devices,* World Scientific.

TANGSTAD, M., KSIAZEK, M. & ANDERSEN, J. 2014. An industrial Si furnace excavation – results and observations. *Silicon for the Chemical and Solar Industry XII.* Trondheim, Norway.

TOMOZEIU, N., ANTOHE, S. & MODREANU, M. 2000. Electrical Properties of LPCVD Polysilicon Deposited in the Vicinity of Amorphous-Polycrystalline Phase. *Journal of Optoelectronics and Advanced Materials,* 2**,** 657-663.

TRANELL, G., ANDERSSON, M., RINGDALEN, E., OSTROVSKI, O. & STEINMO, J. REACTION ZONES IN A FeSi75 FURNACE–RESULTS FROM AN INDUSTRIAL EXCAVATION. Proceedings of the 12th International Ferroalloys Congress, INFACON XII, 2010. 709-715.

VALDERHAUG, A. M. 1992. Modelling and control of submerged-arc ferrosilicon furnaces. *Dr. Theses, The Norwegian Institute of Technology, Trondheim*.

VANGSKÅSEN, J. 2012. *Metal-producing Mechanisms in the Carbothermic Silicon Process.* MSc, NTNU.

WEST, A. R. 1988. *Basic solid state chemistry*, Wiley New York.

APPENDIX A

The macro used to filter data from the resistivity measurements.

```
Sub filtermacro()

Application.ScreenUpdating = False

Dim WS_Count As Integer
Dim I As Integer
Dim siste As Integer
Dim rad As Integer
Dim dataspm As Integer

'Data organisert?
dataspm = 0  '1 = nei, 0 = ja

'Lengde og areal på prøven?
lengde = "1.842"
areal = "Pi() * (3.41/2)^2"

'Er første ark i arbeidsboken tomt?
' Hvis ikke, legg til ett ark fremst i boken!
```

```
'_____

'Hindrer skjermoppdatering
Application.ScreenUpdating = False

    WS_Count = ActiveWorkbook.Worksheets.Count

        For I = 2 To WS_Count

            Worksheets(I).Select
            ThisSheet = Worksheets(I).Name

            If dataspm = 1 Then
            'Sletter unyttig data
                Columns("G:I").Select
                Selection.Delete Shift:=xlToLeft
                Columns("E:E").Select
                Selection.Delete Shift:=xlToLeft
                Columns("B:B").Select
                Selection.Delete Shift:=xlToLeft
                Columns("A:A").Select
                Selection.Delete Shift:=xlToLeft
```

```
'Bytter ut komma med punktum
' (Må fjernes hvis windows bruker , som decimaltegn)
    Cells.Replace What:=",", Replacement:=".", LookAt:=xlPart, SearchOrder _
    :=xlByRows, MatchCase:=False, SearchFormat:=False, ReplaceFormat:=False

'Navngir øverste celler
    Range("D1") = "Current"
    Range("E1") = "Resistance"
    Range("F1") = "Resistivity"
    Range("G1") = "Teste strøm"
    Range("H1") = "Tester uteligger"
End If

'Siste rad i arket
siste = Worksheets(I).Range("A1").End(xlDown).Row


For rad = 2 To siste

    'Går gjennom linjene
If rad < siste + 1 Then

'Setter inn current, resistance, resistivity
```

```
Worksheets(I).Range("D" & rad) = "=C" & rad & "*1000"

Worksheets(I).Range("E" & rad) = "=B" & rad & "*10/D" & rad

Worksheets(I).Range("F" & rad) = "=E" & rad & "*" & areal & "/" & lengde


'Legger til formelen i alle arkene - > KAN SKIFTES MED HENSYN TIL LEDNINGSEVNEN

Worksheets(I).Range("G" & rad) = "=if(D" & rad & ">3,1,0)"



'Sletter rad der strømmen er av

   If Worksheets(I).Range("G" & rad) = 0 Then

      Worksheets(I).Range("G" & rad).EntireRow.Delete

      rad = rad - 1

      siste = siste - 1

   End If


End If


If rad = siste Then

Exit For

End If


Next
```

```
'Legger in average og stdev


        'Legger til formelen i alle arkene
        Worksheets(I).Range("J1") = "Average"
        Worksheets(I).Range("J2") = "=average(F2:F" & siste & ")"
        Worksheets(I).Range("K1") = "StDev"
        Worksheets(I).Range("K2") = "=stdev.P(F2:F" & siste & ")"




    For rad = 2 To siste


        'Går gjennom linjene
    If rad < siste + 1 Then


        Worksheets(I).Range("H" & rad) = "=IF(OR(F" & rad & ">$J$2+$K$2*3,F" & rad
& "<$J$2-$K$2*3),0,1)"
    End If


    Next
```

```
    'Lagrer data som tall og ikke formler
Worksheets(I).Range("H2:H" & siste).Copy
Worksheets(I).Range("H2:H" & siste).PasteSpecial (xlPasteValues)



c = 1
For c = 1 To 3
For rad = 2 To siste
'Sletter rad med utligger
    If Worksheets(I).Range("H" & rad) = 0 Then
        Worksheets(I).Range("H" & rad).EntireRow.Delete
        rad = rad - 1
        siste = siste - 1

        If Worksheets(I).Range("J2") = 0 Then
            Worksheets(I).Range("J2") = "=average(F2:F" & siste & ")"
            Worksheets(I).Range("K2") = "=stdev.P(F2:F" & siste & ")"
        End If
    End If

If rad = siste Then
Exit For
```

```
        End If


        Next

        Next


'Teller antall datapunkt

Worksheets(I).Range("L2") = "=count(F2:F" & siste & ")"


'Legger inn i dataark (første ark)


            'Kopierer formelens verdier til første ark

            Worksheets(I).Range("J2").Copy

            Worksheets(1).Range("B" & (I + 1)).PasteSpecial Paste:=xlPasteValues

            Worksheets(I).Range("K2").Copy

            Worksheets(1).Range("C" & (I + 1)).PasteSpecial Paste:=xlPasteValues

            Worksheets(I).Range("L2").Copy

            Worksheets(1).Range("D" & (I + 1)).PasteSpecial Paste:=xlPasteValues


            Worksheets(1).Range("A" & (I + 1)) = ThisSheet


'Setter inn plot av res og current i arket
```

```
    Range("K22").Select


    ActiveSheet.Shapes.AddChart.Select
    ActiveChart.ChartType = xlXYScatter
    ActiveChart.SeriesCollection.NewSeries
    ActiveChart.SeriesCollection(1).Name = "Resistivity"
    ActiveChart.SeriesCollection(1).XValues = "='" & ThisSheet & "'!$A2:$A" & siste
    ActiveChart.SeriesCollection(1).Values = "='" & ThisSheet & "'!$F2:$F" & siste
        ActiveChart.Axes(xlValue).MinimumScale = 0
        ActiveChart.Axes(xlValue).MaximumScale = 2
    ActiveChart.SeriesCollection.NewSeries
    ActiveChart.SeriesCollection(2).Name = "Current"
    ActiveChart.SeriesCollection(2).XValues = "='" & ThisSheet & "'!$A2:$A" & siste
    ActiveChart.SeriesCollection(2).Values = "='" & ThisSheet & "'!$D2:$D" & siste
    ActiveChart.SeriesCollection(2).AxisGroup = 2


        Next I
        Application.ScreenUpdating = True


End Sub
```

APPENDIX B

A selection of the atomic number contrast images taken of the SiC-crust samples.

Sample E#1:

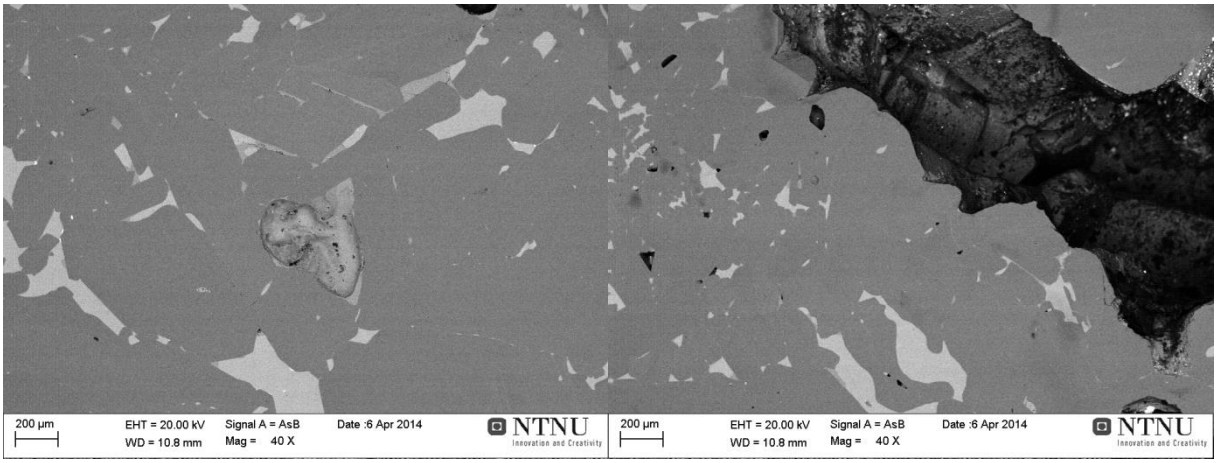

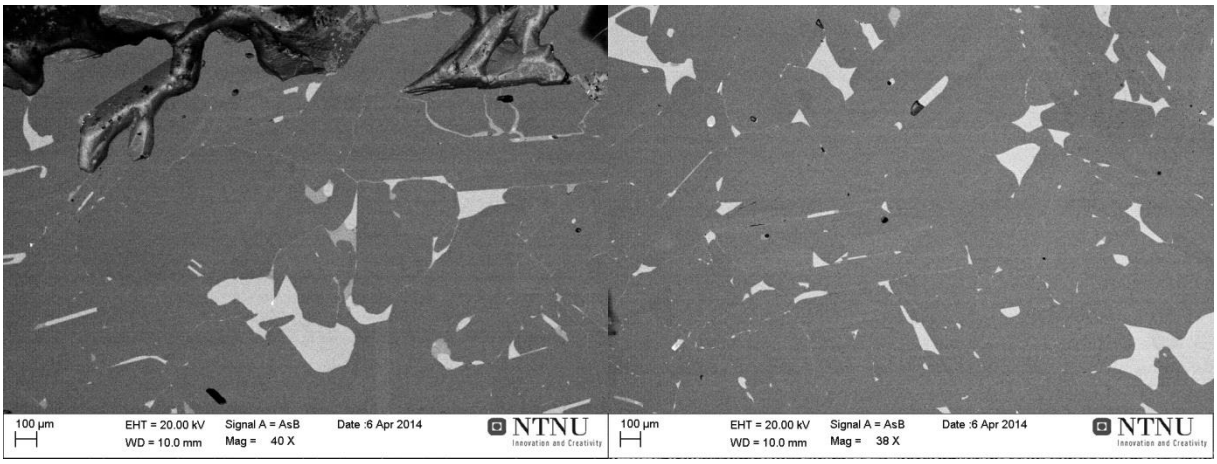

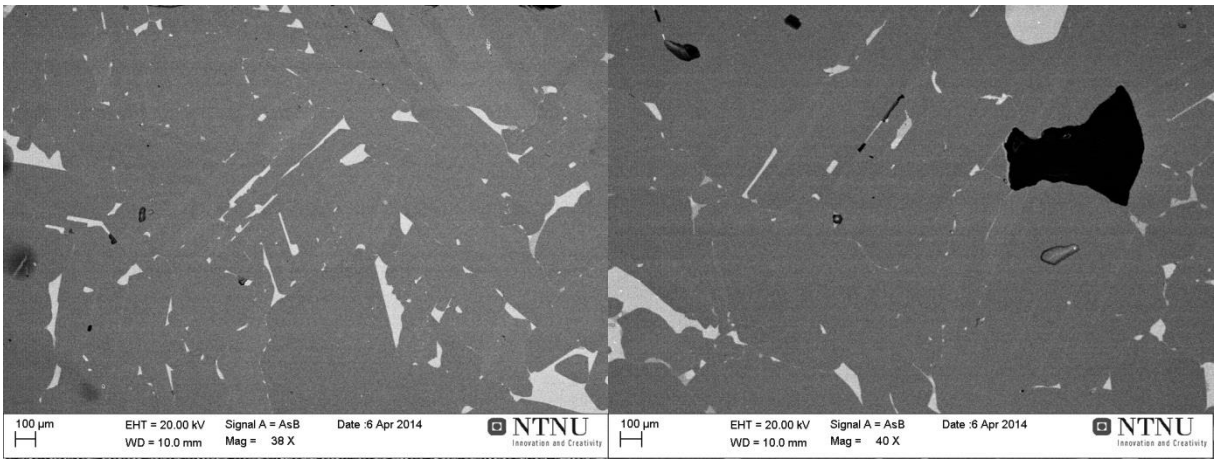

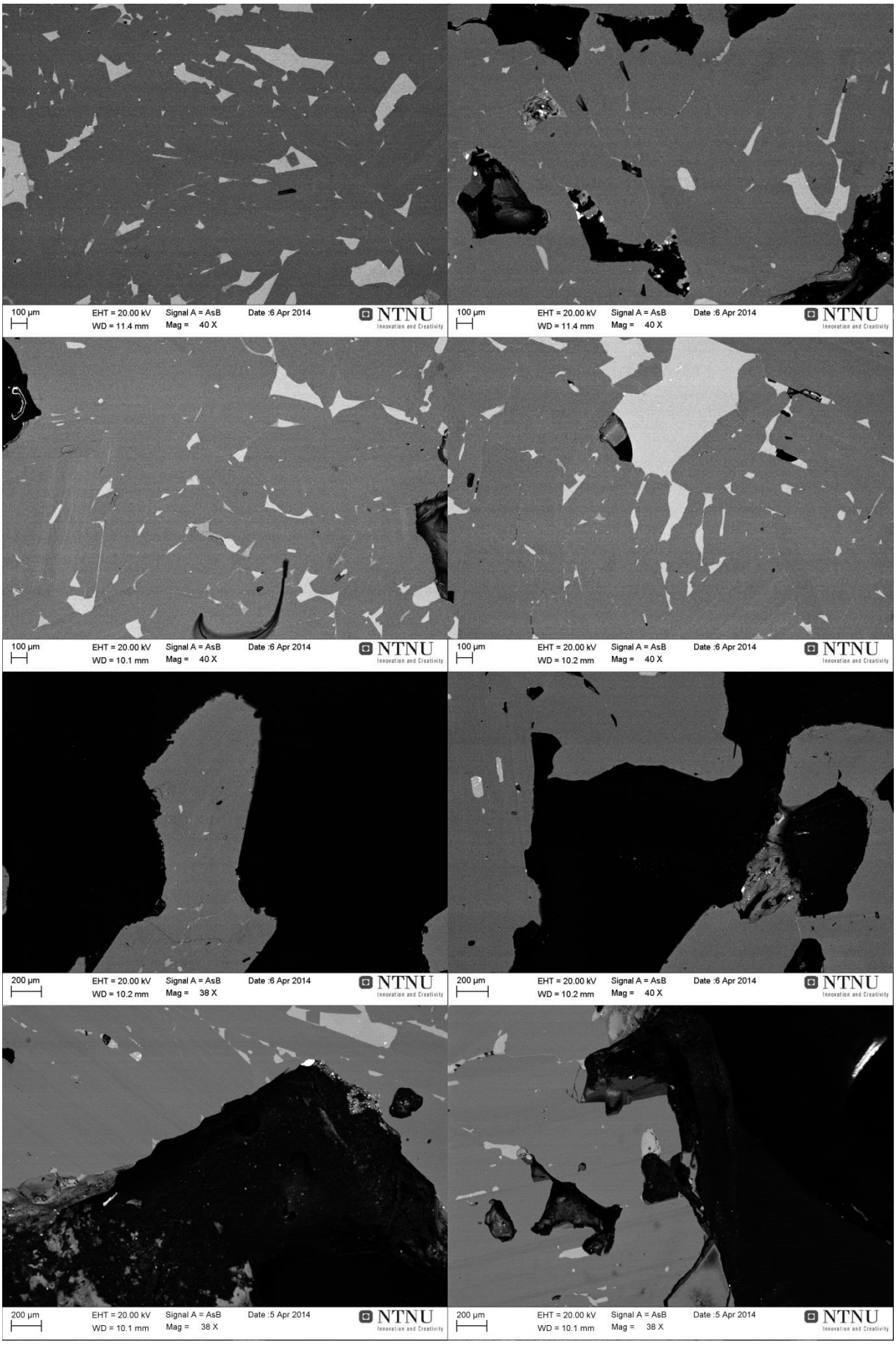
100 µm
EHT = 20.00 kV
WD = 11.4 mm
Signal A = AsB
Mag = 40 X
Date :6 Apr 2014
NTNU
Innovation and Creativity
100 µm
EHT = 20.00 kV
WD = 11.4 mm
Signal A = AsB
Mag = 40 X
Date :6 Apr 2014
NTNU
Innovation and Creativity
100 µm
EHT = 20.00 kV
WD = 10.1 mm
Signal A = AsB
Mag = 40 X
Date :6 Apr 2014
NTNU
Innovation and Creativity
100 µm
EHT = 20.00 kV
WD = 10.2 mm
Signal A = AsB
Mag = 40 X
Date :6 Apr 2014
NTNU
Innovation and Creativity
200 µm
EHT = 20.00 kV
WD = 10.2 mm
Signal A = AsB
Mag = 38 X
Date :6 Apr 2014
NTNU
Innovation and Creativity
200 µm
EHT = 20.00 kV
WD = 10.2 mm
Signal A = AsB
Mag = 40 X
Date :6 Apr 2014
NTNU
Innovation and Creativity
200 µm
EHT = 20.00 kV
WD = 10.1 mm
Signal A = AsB
Mag = 38 X
Date :5 Apr 2014
NTNU
Innovation and Creativity
200 µm
EHT = 20.00 kV
WD = 10.1 mm
Signal A = AsB
Mag = 38 X
Date :5 Apr 2014
NTNU
Innovation and Creativity

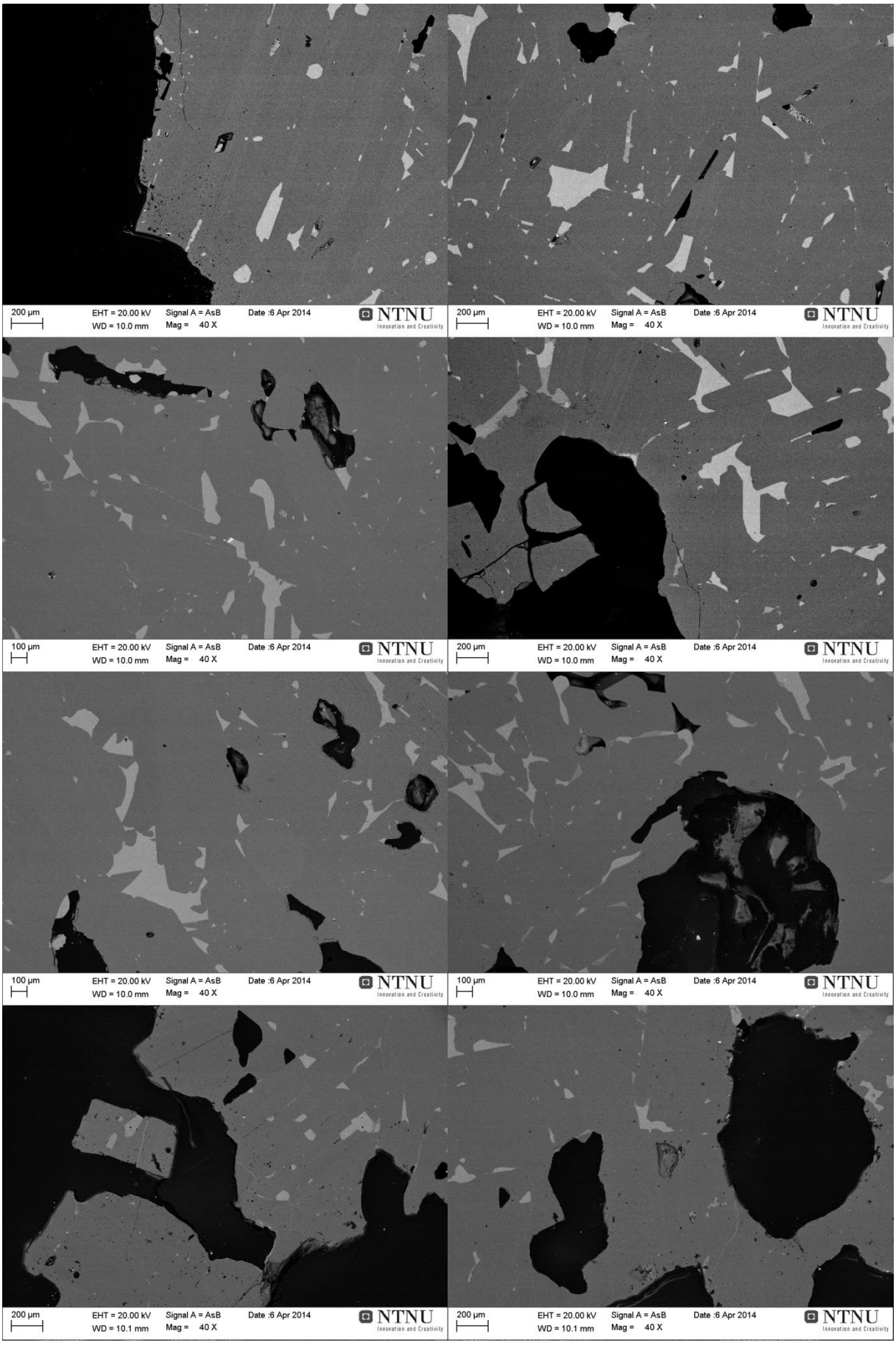
200 µm
EHT = 20.00 kV
WD = 10.0 mm
Signal A = AsB
Mag = 40 X
Date :6 Apr 2014
NTNU
Innovation and Creativity
200 µm
EHT = 20.00 kV
WD = 10.0 mm
Signal A = AsB
Mag = 40 X
Date :6 Apr 2014
NTNU
Innovation and Creativity
100 µm
EHT = 20.00 kV
WD = 10.0 mm
Signal A = AsB
Mag = 40 X
Date :6 Apr 2014
NTNU
Innovation and Creativity
200 µm
EHT = 20.00 kV
WD = 10.0 mm
Signal A = AsB
Mag = 40 X
Date :6 Apr 2014
NTNU
Innovation and Creativity
100 µm
EHT = 20.00 kV
WD = 10.0 mm
Signal A = AsB
Mag = 40 X
Date :6 Apr 2014
NTNU
Innovation and Creativity
100 µm
EHT = 20.00 kV
WD = 10.0 mm
Signal A = AsB
Mag = 40 X
Date :6 Apr 2014
NTNU
Innovation and Creativity
200 µm
EHT = 20.00 kV
WD = 10.1 mm
Signal A = AsB
Mag = 40 X
Date :6 Apr 2014
NTNU
Innovation and Creativity
200 µm
EHT = 20.00 kV
WD = 10.1 mm
Signal A = AsB
Mag = 40 X
Date :6 Apr 2014
NTNU
Innovation and Creativity

Sample E#20:

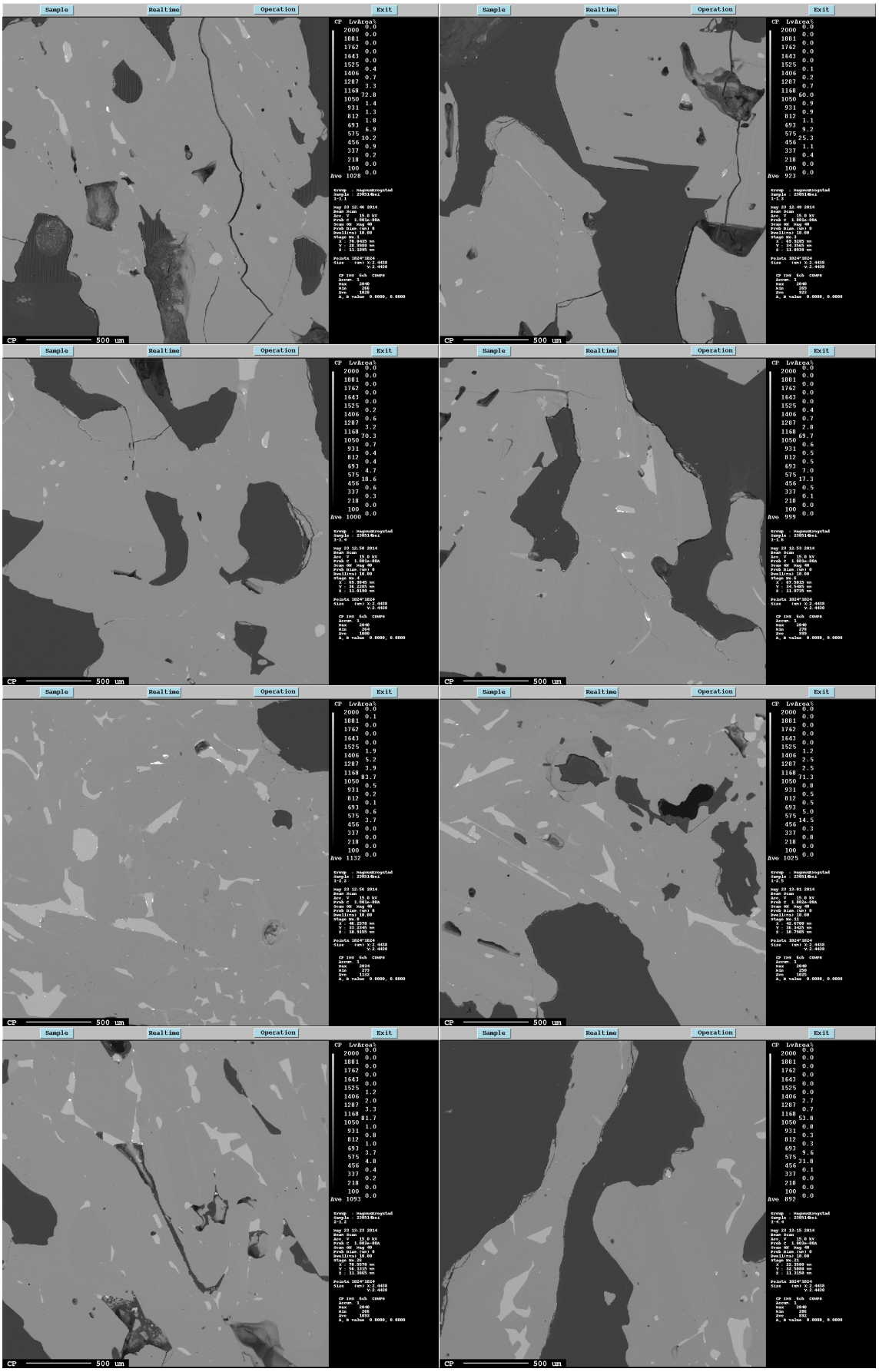

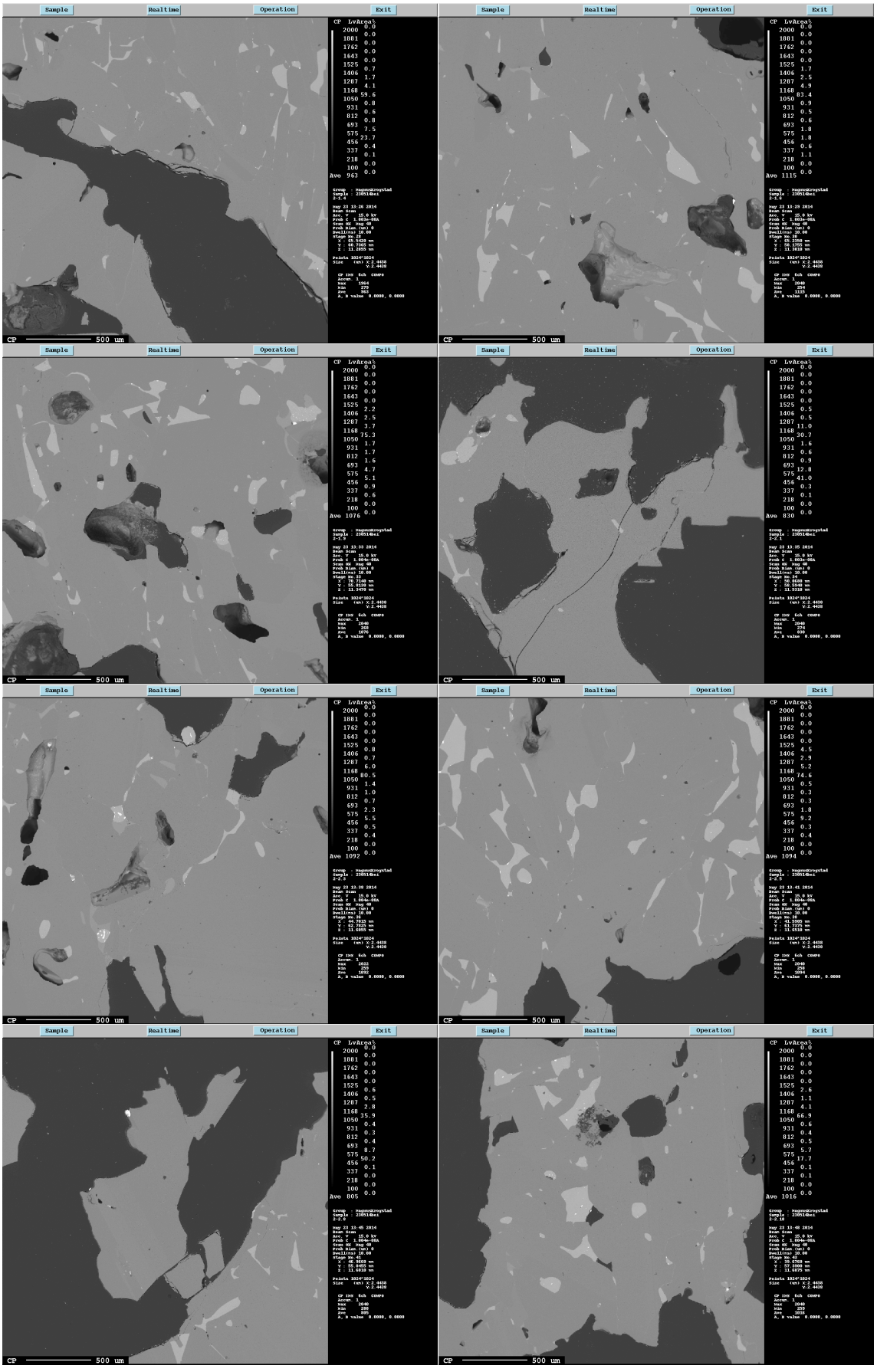
Sample
Realtime
Operation
Exit
CP
500 um

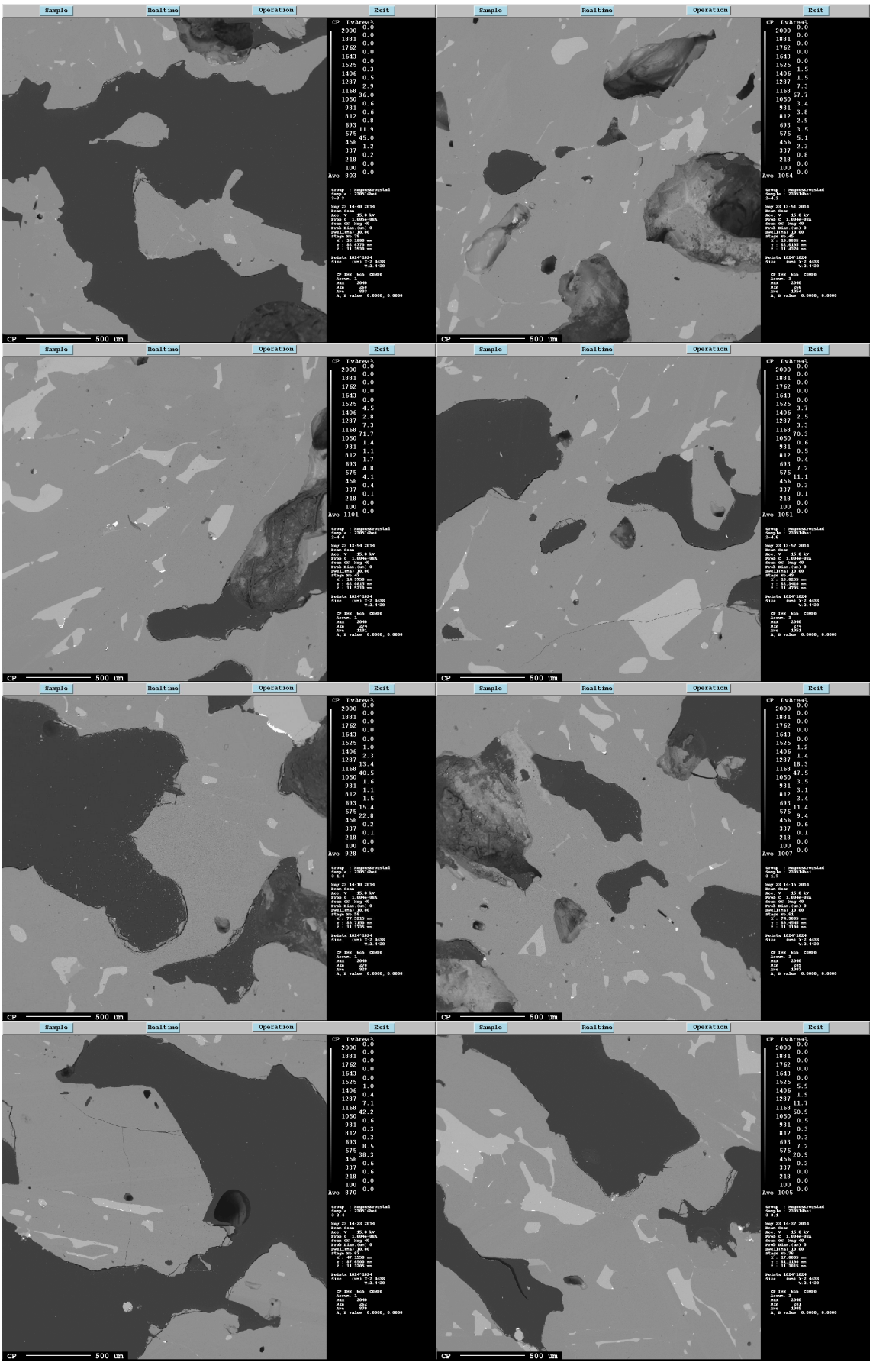
Sample
Realtime
Operation
Exit
CP
500 um

Sample E#41:

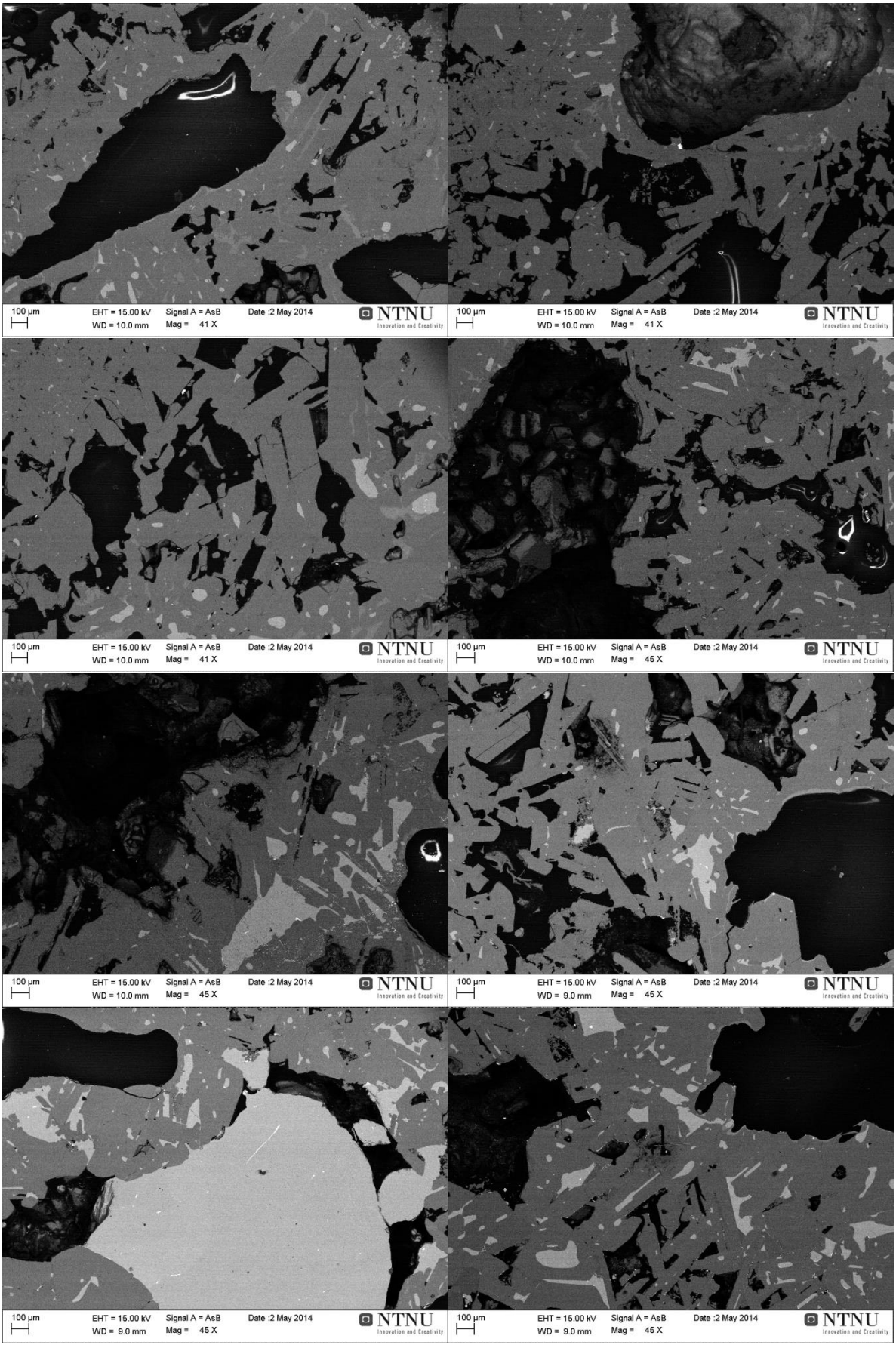
100 µm
EHT = 15.00 kV
WD = 10.0 mm
Signal A = AsB
Mag = 41 X
Date :2 May 2014
NTNU
Innovation and Creativity
100 µm
EHT = 15.00 kV
WD = 10.0 mm
Signal A = AsB
Mag = 41 X
Date :2 May 2014
NTNU
Innovation and Creativity
100 µm
EHT = 15.00 kV
WD = 10.0 mm
Signal A = AsB
Mag = 41 X
Date :2 May 2014
NTNU
Innovation and Creativity
100 µm
EHT = 15.00 kV
WD = 10.0 mm
Signal A = AsB
Mag = 45 X
Date :2 May 2014
NTNU
Innovation and Creativity
100 µm
EHT = 15.00 kV
WD = 10.0 mm
Signal A = AsB
Mag = 45 X
Date :2 May 2014
NTNU
Innovation and Creativity
100 µm
EHT = 15.00 kV
WD = 9.0 mm
Signal A = AsB
Mag = 45 X
Date :2 May 2014
NTNU
Innovation and Creativity
100 µm
EHT = 15.00 kV
WD = 9.0 mm
Signal A = AsB
Mag = 45 X
Date :2 May 2014
NTNU
Innovation and Creativity
100 µm
EHT = 15.00 kV
WD = 9.0 mm
Signal A = AsB
Mag = 45 X
Date :2 May 2014
NTNU
Innovation and Creativity

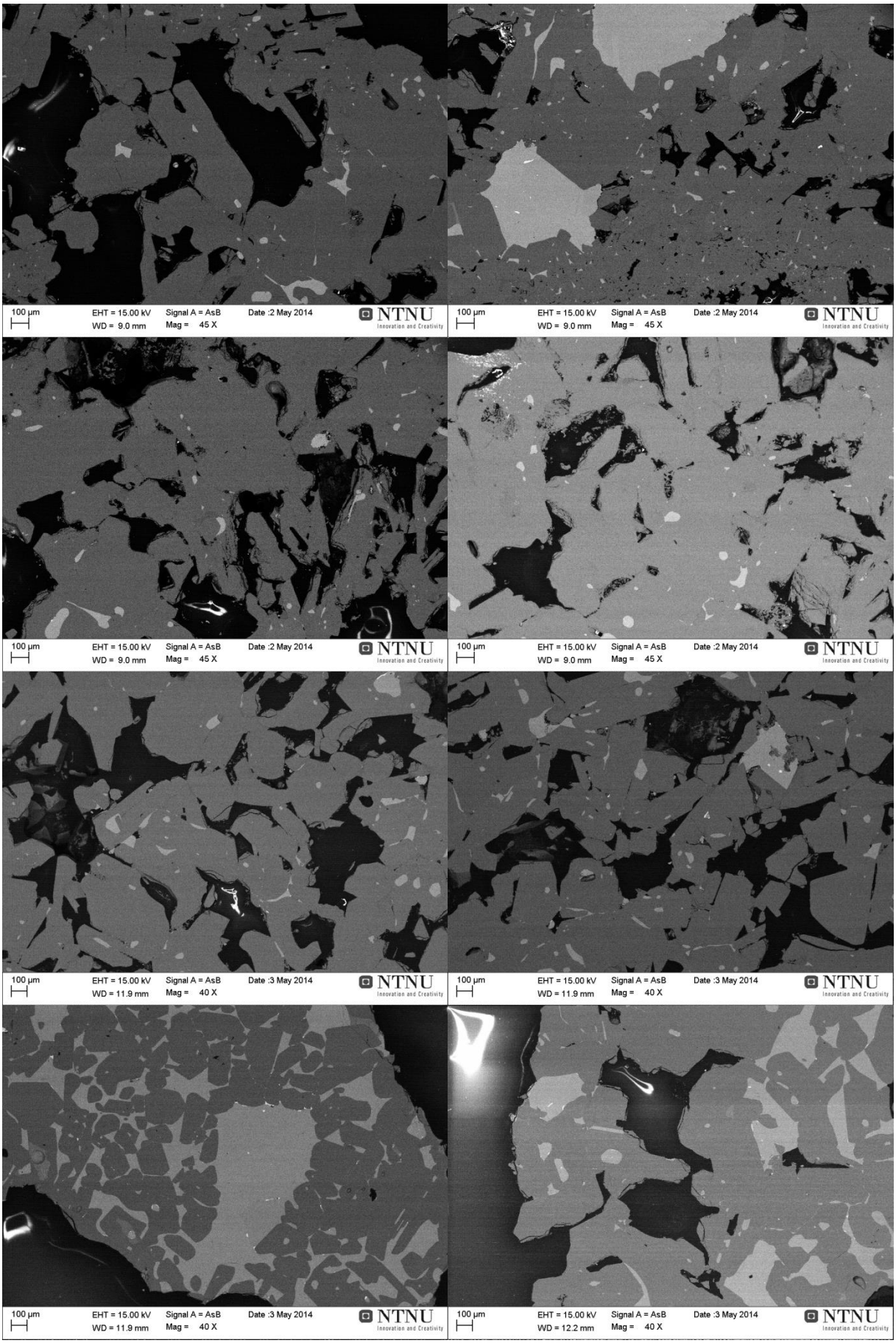
100 µm
EHT = 15.00 kV
WD = 9.0 mm
Signal A = AsB
Mag = 45 X
Date :2 May 2014
NTNU
Innovation and Creativity
100 µm
EHT = 15.00 kV
WD = 9.0 mm
Signal A = AsB
Mag = 45 X
Date :2 May 2014
NTNU
Innovation and Creativity
100 µm
EHT = 15.00 kV
WD = 9.0 mm
Signal A = AsB
Mag = 45 X
Date :2 May 2014
NTNU
Innovation and Creativity
100 µm
EHT = 15.00 kV
WD = 9.0 mm
Signal A = AsB
Mag = 45 X
Date :2 May 2014
NTNU
Innovation and Creativity
100 µm
EHT = 15.00 kV
WD = 11.9 mm
Signal A = AsB
Mag = 40 X
Date :3 May 2014
NTNU
Innovation and Creativity
100 µm
EHT = 15.00 kV
WD = 11.9 mm
Signal A = AsB
Mag = 40 X
Date :3 May 2014
NTNU
Innovation and Creativity
100 µm
EHT = 15.00 kV
WD = 11.9 mm
Signal A = AsB
Mag = 40 X
Date :3 May 2014
NTNU
Innovation and Creativity
100 µm
EHT = 15.00 kV
WD = 12.2 mm
Signal A = AsB
Mag = 40 X
Date :3 May 2014
NTNU
Innovation and Creativity

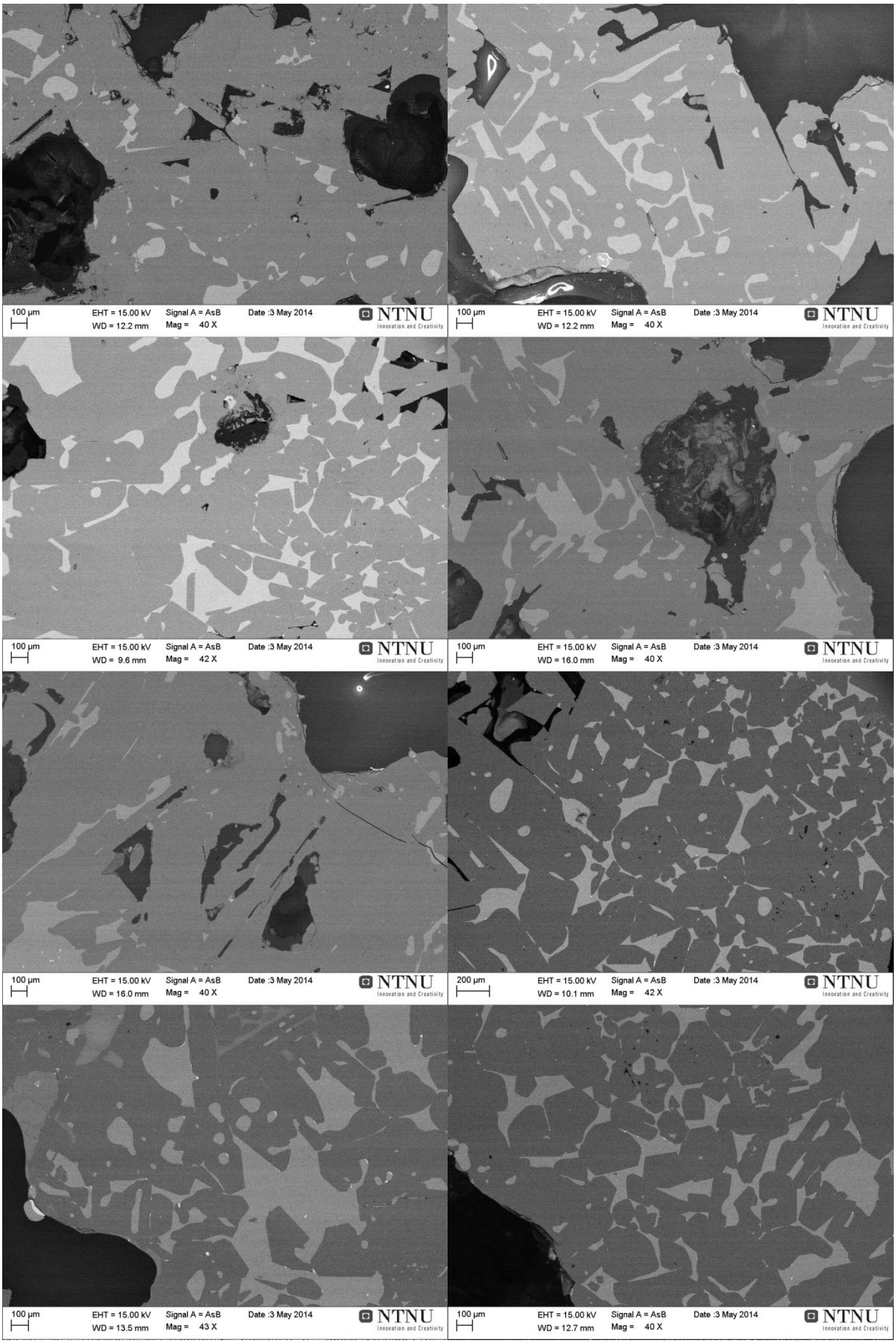
100 µm
EHT = 15.00 kV
WD = 12.2 mm
Signal A = AsB
Mag = 40 X
Date :3 May 2014
NTNU
Innovation and Creativity
100 µm
EHT = 15.00 kV
WD = 12.2 mm
Signal A = AsB
Mag = 40 X
Date :3 May 2014
NTNU
Innovation and Creativity
100 µm
EHT = 15.00 kV
WD = 9.6 mm
Signal A = AsB
Mag = 42 X
Date :3 May 2014
NTNU
Innovation and Creativity
100 µm
EHT = 15.00 kV
WD = 16.0 mm
Signal A = AsB
Mag = 40 X
Date :3 May 2014
NTNU
Innovation and Creativity
100 µm
EHT = 15.00 kV
WD = 16.0 mm
Signal A = AsB
Mag = 40 X
Date :3 May 2014
NTNU
Innovation and Creativity
200 µm
EHT = 15.00 kV
WD = 10.1 mm
Signal A = AsB
Mag = 42 X
Date :3 May 2014
NTNU
Innovation and Creativity
100 µm
EHT = 15.00 kV
WD = 13.5 mm
Signal A = AsB
Mag = 43 X
Date :3 May 2014
NTNU
Innovation and Creativity
100 µm
EHT = 15.00 kV
WD = 12.7 mm
Signal A = AsB
Mag = 40 X
Date :3 May 2014
NTNU
Innovation and Creativity

Sample F#33:

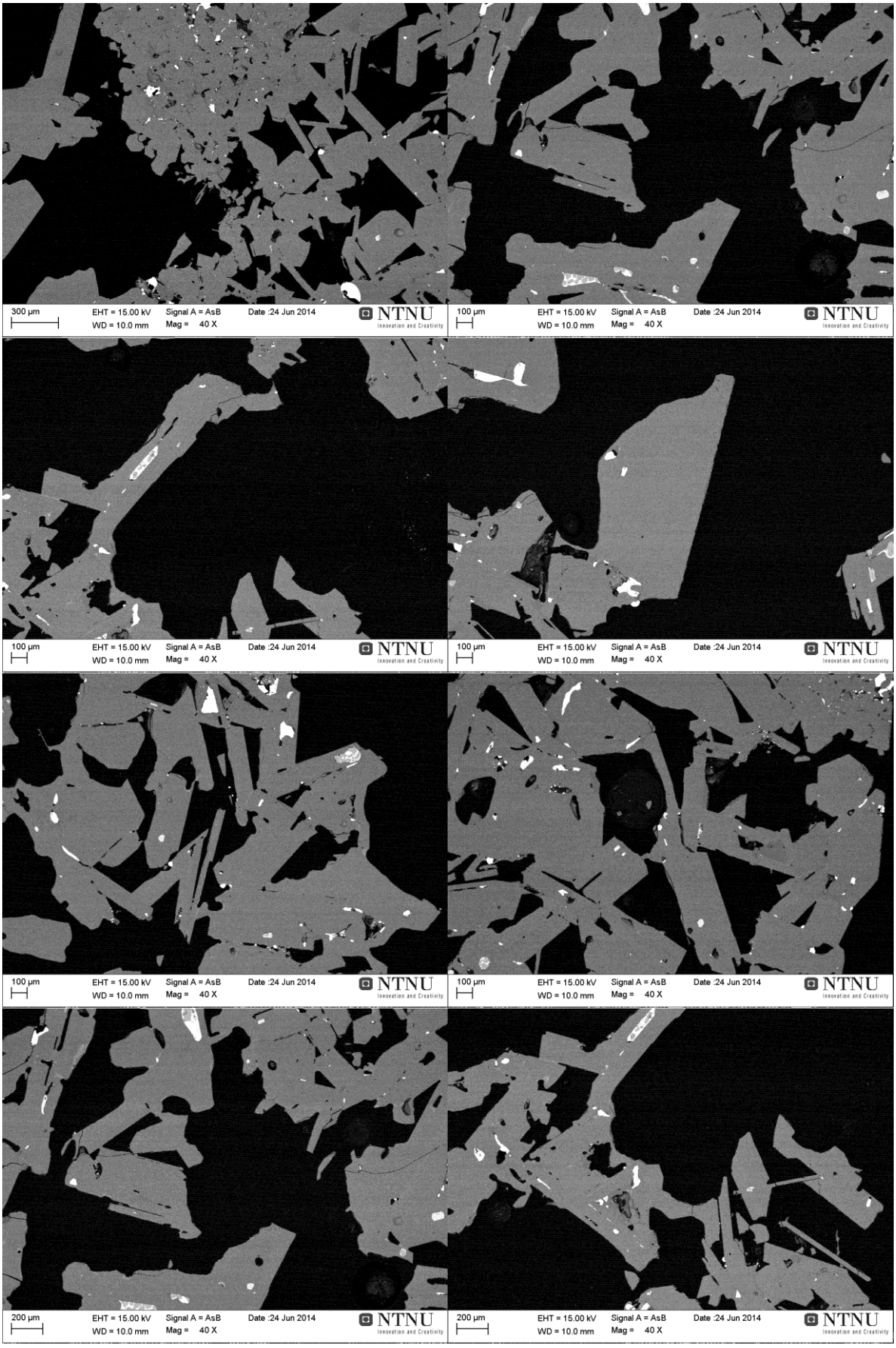
300 µm
EHT = 15.00 kV
WD = 10.0 mm
Signal A = AsB
Mag = 40 X
Date :24 Jun 2014
NTNU
100 µm
EHT = 15.00 kV
WD = 10.0 mm
Signal A = AsB
Mag = 40 X
Date :24 Jun 2014
NTNU
100 µm
EHT = 15.00 kV
WD = 10.0 mm
Signal A = AsB
Mag = 40 X
Date :24 Jun 2014
NTNU
100 µm
EHT = 15.00 kV
WD = 10.0 mm
Signal A = AsB
Mag = 40 X
Date :24 Jun 2014
NTNU
100 µm
EHT = 15.00 kV
WD = 10.0 mm
Signal A = AsB
Mag = 40 X
Date :24 Jun 2014
NTNU
100 µm
EHT = 15.00 kV
WD = 10.0 mm
Signal A = AsB
Mag = 40 X
Date :24 Jun 2014
NTNU
200 µm
EHT = 15.00 kV
WD = 10.0 mm
Signal A = AsB
Mag = 40 X
Date :24 Jun 2014
NTNU
200 µm
EHT = 15.00 kV
WD = 10.0 mm
Signal A = AsB
Mag = 40 X
Date :24 Jun 2014
NTNU

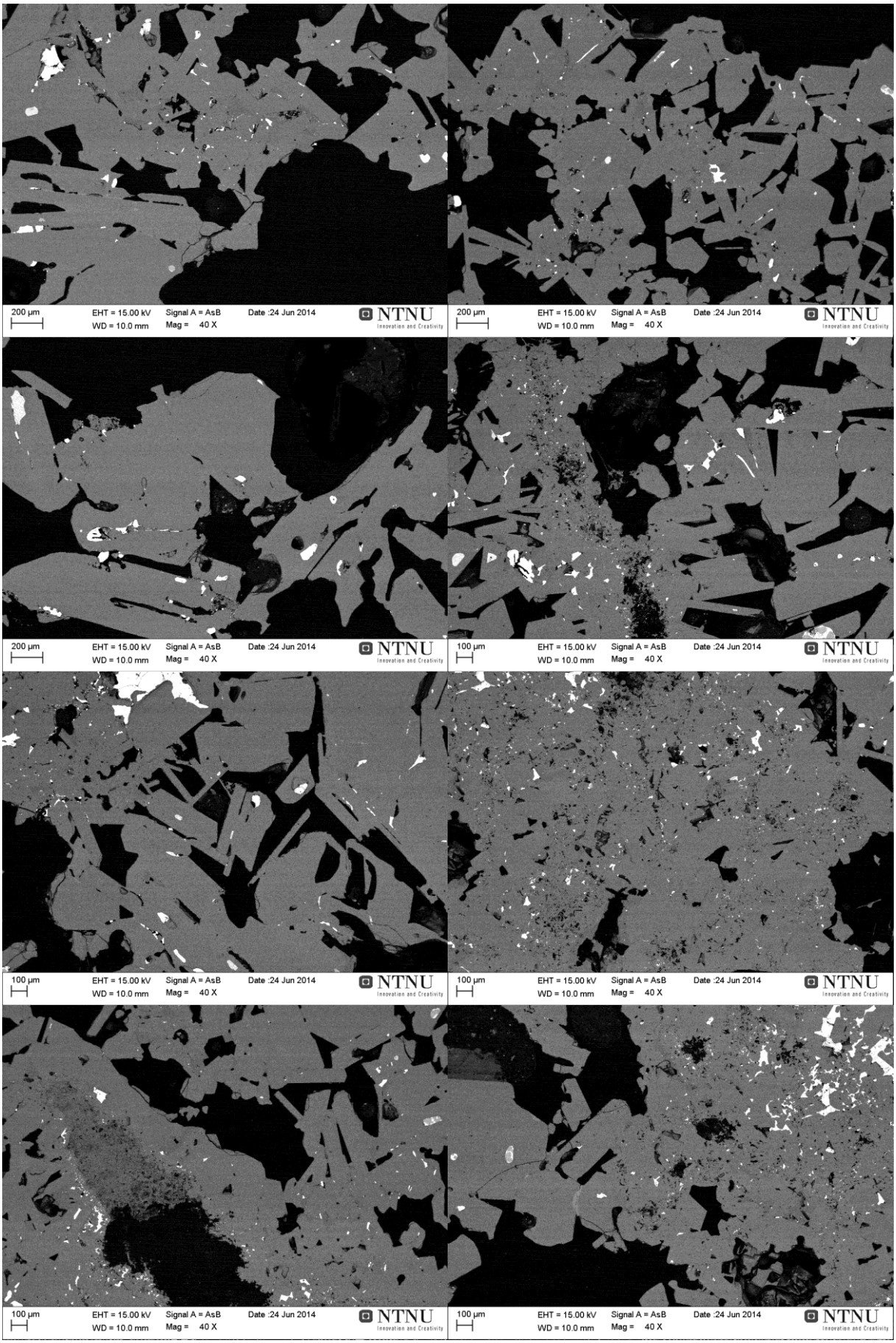
200 µm
EHT = 15.00 kV
WD = 10.0 mm
Signal A = AsB
Mag = 40 X
Date :24 Jun 2014
NTNU
Innovation and Creativity
200 µm
EHT = 15.00 kV
WD = 10.0 mm
Signal A = AsB
Mag = 40 X
Date :24 Jun 2014
NTNU
Innovation and Creativity
200 µm
EHT = 15.00 kV
WD = 10.0 mm
Signal A = AsB
Mag = 40 X
Date :24 Jun 2014
NTNU
Innovation and Creativity
100 µm
EHT = 15.00 kV
WD = 10.0 mm
Signal A = AsB
Mag = 40 X
Date :24 Jun 2014
NTNU
Innovation and Creativity
100 µm
EHT = 15.00 kV
WD = 10.0 mm
Signal A = AsB
Mag = 40 X
Date :24 Jun 2014
NTNU
Innovation and Creativity
100 µm
EHT = 15.00 kV
WD = 10.0 mm
Signal A = AsB
Mag = 40 X
Date :24 Jun 2014
NTNU
Innovation and Creativity
100 µm
EHT = 15.00 kV
WD = 10.0 mm
Signal A = AsB
Mag = 40 X
Date :24 Jun 2014
NTNU
Innovation and Creativity
100 µm
EHT = 15.00 kV
WD = 10.0 mm
Signal A = AsB
Mag = 40 X
Date :24 Jun 2014
NTNU
Innovation and Creativity

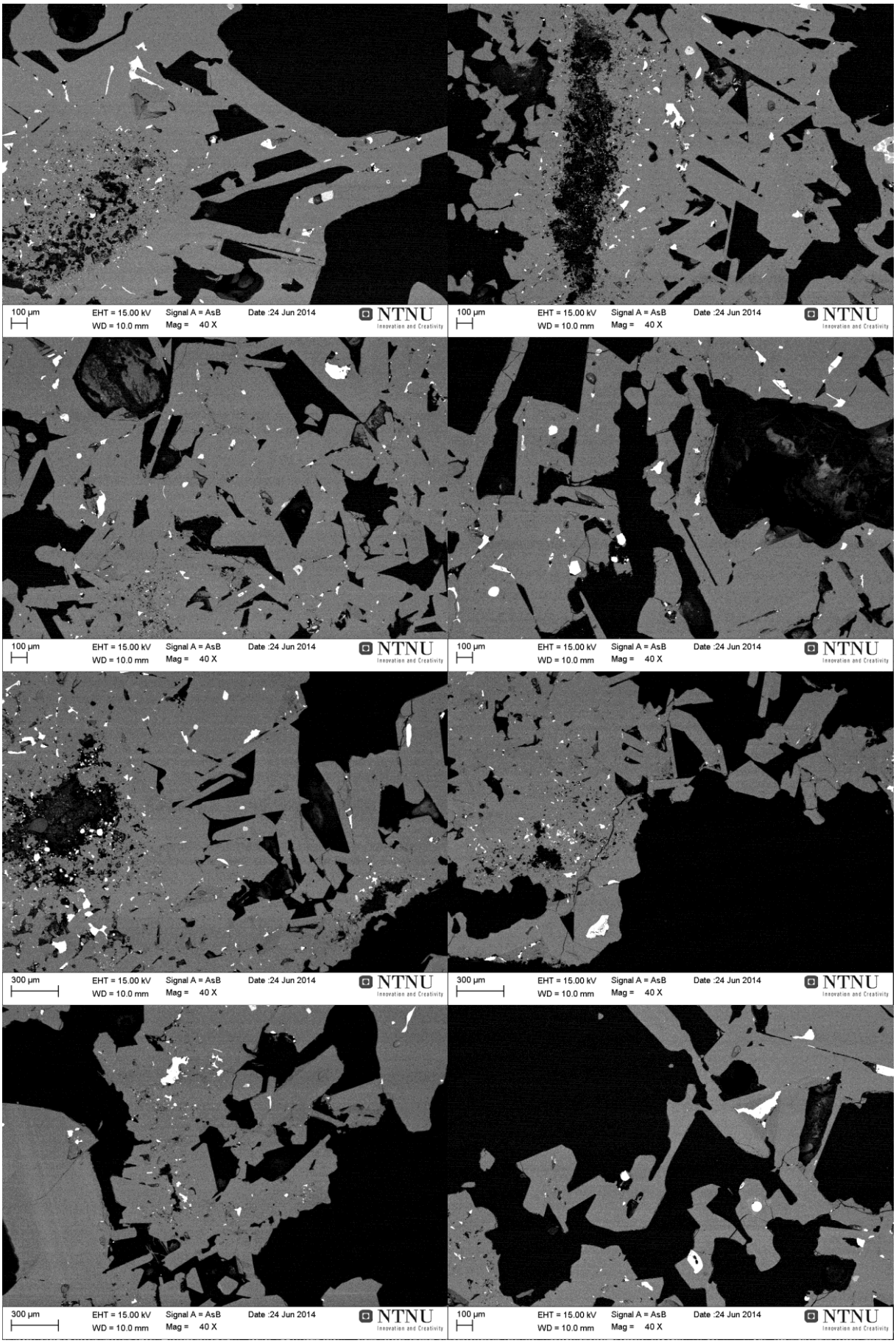
100 µm
EHT = 15.00 kV
WD = 10.0 mm
Signal A = AsB
Mag = 40 X
Date :24 Jun 2014
NTNU
Innovation and Creativity
100 µm
EHT = 15.00 kV
WD = 10.0 mm
Signal A = AsB
Mag = 40 X
Date :24 Jun 2014
NTNU
Innovation and Creativity
100 µm
EHT = 15.00 kV
WD = 10.0 mm
Signal A = AsB
Mag = 40 X
Date :24 Jun 2014
NTNU
Innovation and Creativity
100 µm
EHT = 15.00 kV
WD = 10.0 mm
Signal A = AsB
Mag = 40 X
Date :24 Jun 2014
NTNU
Innovation and Creativity
300 µm
EHT = 15.00 kV
WD = 10.0 mm
Signal A = AsB
Mag = 40 X
Date :24 Jun 2014
NTNU
Innovation and Creativity
300 µm
EHT = 15.00 kV
WD = 10.0 mm
Signal A = AsB
Mag = 40 X
Date :24 Jun 2014
NTNU
Innovation and Creativity
300 µm
EHT = 15.00 kV
WD = 10.0 mm
Signal A = AsB
Mag = 40 X
Date :24 Jun 2014
NTNU
Innovation and Creativity
100 µm
EHT = 15.00 kV
WD = 10.0 mm
Signal A = AsB
Mag = 40 X
Date :24 Jun 2014
NTNU
Innovation and Creativity

Sample F#97:

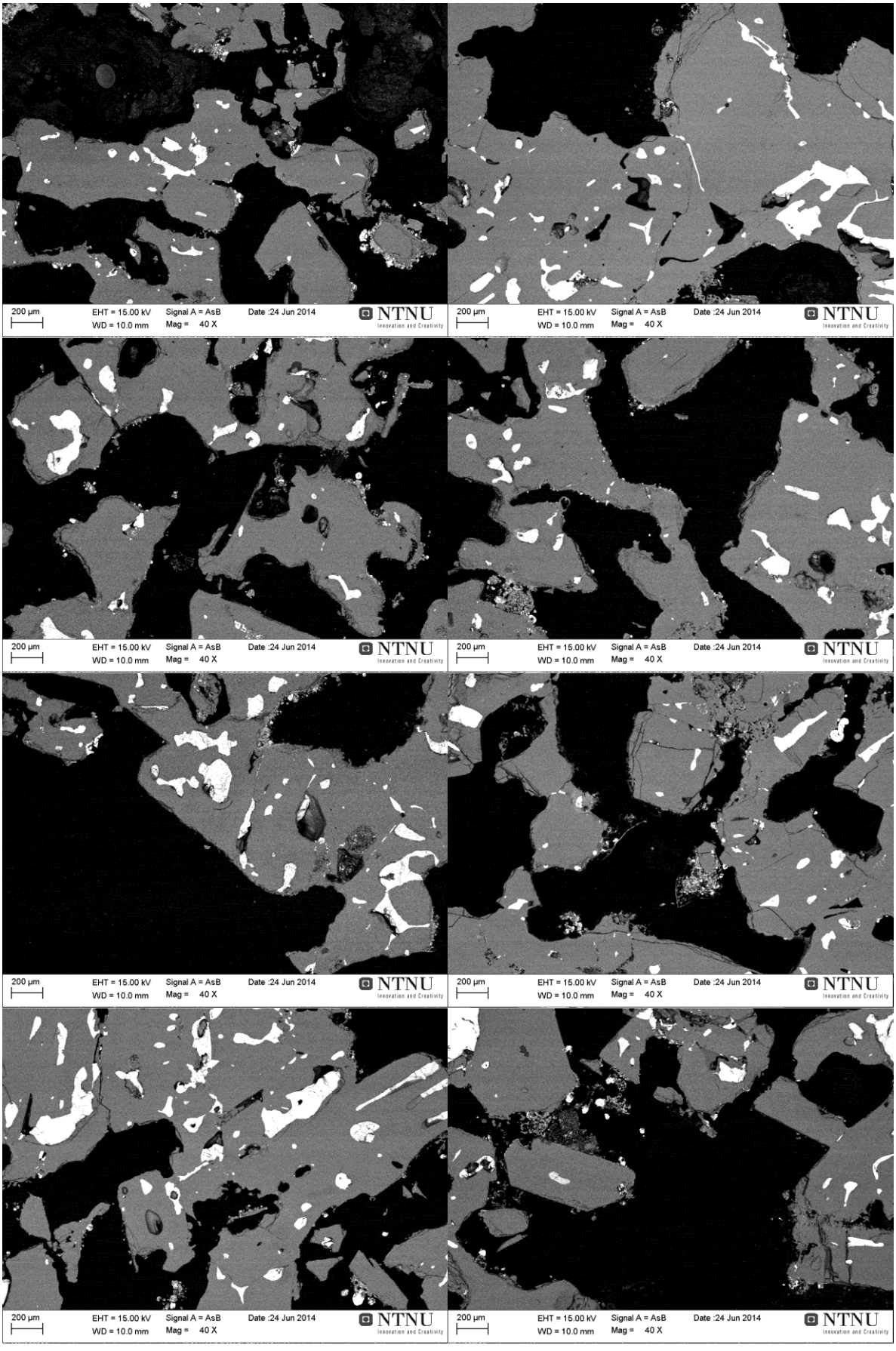
200 µm
EHT = 15.00 kV
WD = 10.0 mm
Signal A = AsB
Mag = 40 X
Date :24 Jun 2014
NTNU
Innovation and Creativity

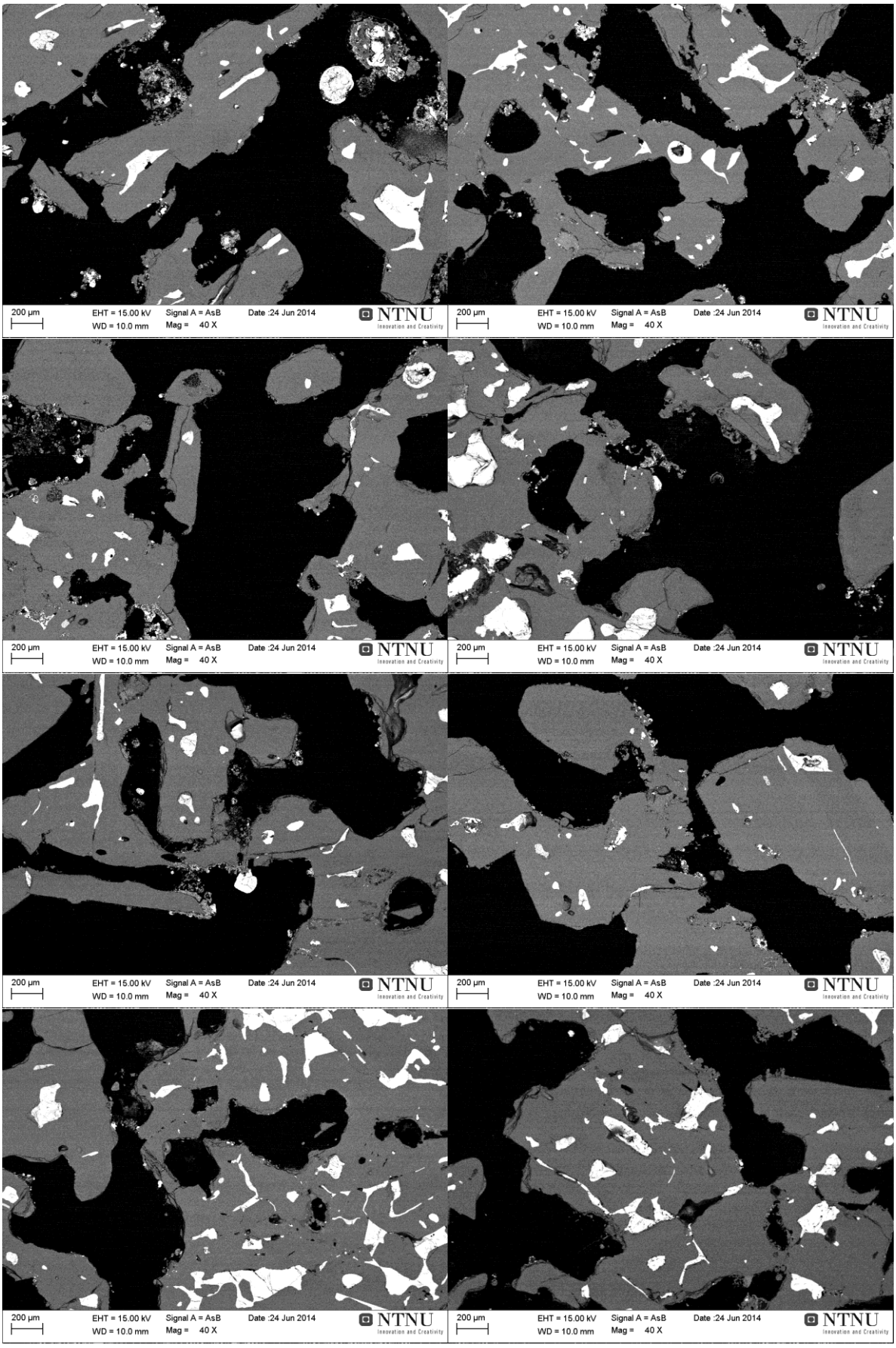
200 µm
EHT = 15.00 kV
WD = 10.0 mm
Signal A = AsB
Mag = 40 X
Date :24 Jun 2014
NTNU
Innovation and Creativity

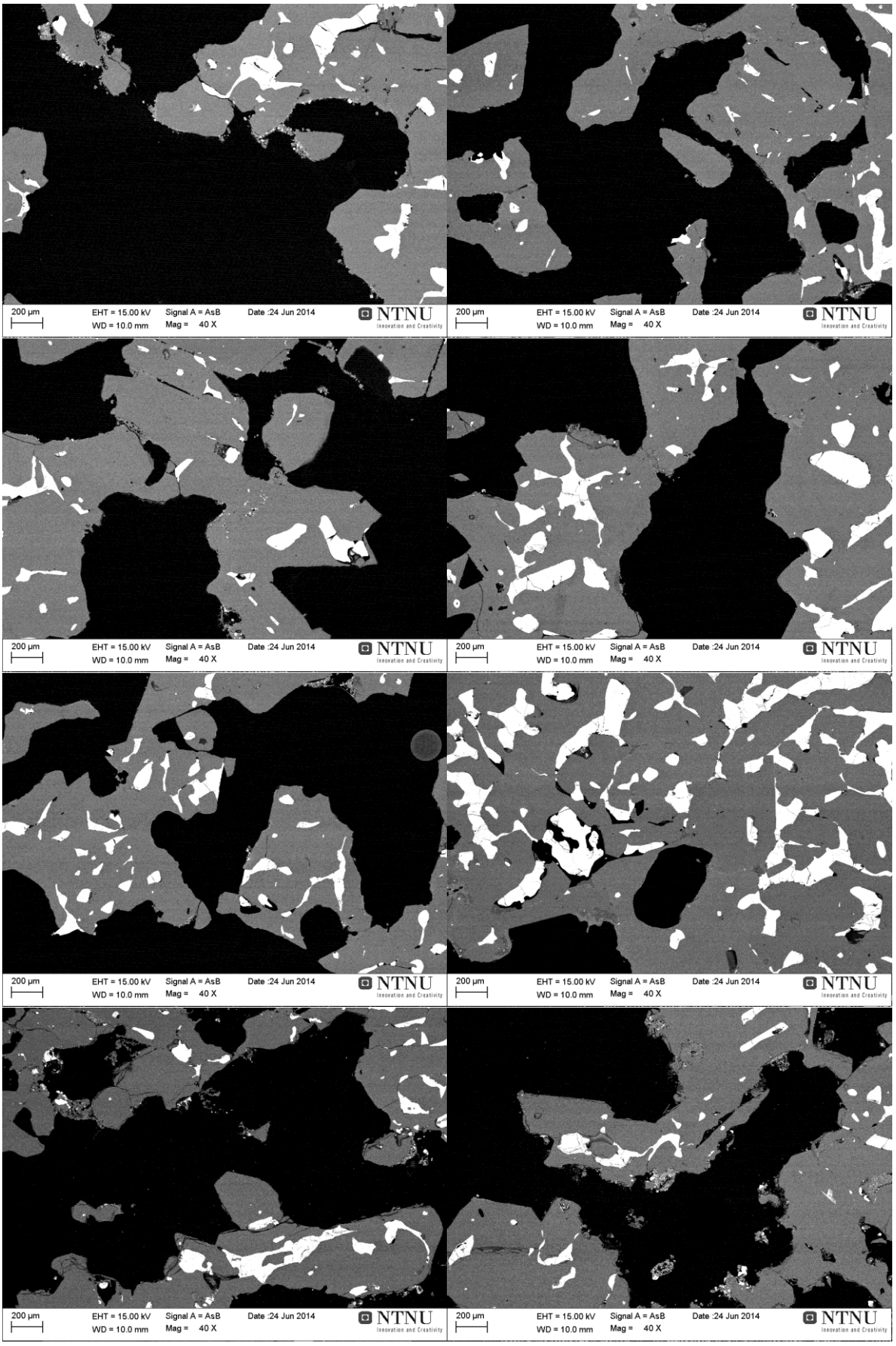
200 µm
EHT = 15.00 kV
WD = 10.0 mm
Signal A = AsB
Mag = 40 X
Date :24 Jun 2014
NTNU
Innovation and Creativity